MASTER

A multi-particle DNS model for TCM heat battery applications

D' Rose, R.D.

Award date:
2019

Department of Mechanical Engineering
Energy Technology group

A Multi-Particle DNS Model for TCM Heat Battery Applications

Master Thesis

Ruben D. D'Rose

Supervisors
ir. M.A.J.M. Beving
Dr.ir. A.J.H. Frijns

Graduation committee
Dr.ir. C.C.M. Rindt
Dr.ir. A.J.H. Frijns
Dr. Y. Tang

Eindhoven, November 2019

Abstract

In the transition of the energy sector from fossil fuels to sustainable resources, a main issue arises from the energy supply/demand mismatch. Seasonal thermal energy storage can mitigate this problem by storing excess of energy during summer, which can then be used during wintertime when demand exceeds supply. A promising type of thermal energy storage is the thermal battery. Using a thermo-chemical material (TCM), heat can be stored at relatively high energy density and with minimal thermal losses. The modelling of a TCM heat battery can provide useful insight on the performance without the need for expensive equipment. However, doing this may not be so straightforward.

For this thesis, a Computational Fluid Dynamics model of a Representative Elementary Volume (REV) was developed with the goal to simulate the hydration process of a heat battery. To this end, use was made of Direct Numerical Simulation to model the flow through the particle bed, including heat and mass transfer. The REV consisted of a number of K_2CO_3 particles in a face-centered cubic lattice. Discretizing the domain with a body-fitted unstructured mesh, the particles were shrunk by 3% to create space for intermediate cells at the particle contact points and avoid mesh degradation. The hydration kinetics were determined using the Arrhenius equation, including a shape term and water vapour pressure dependency. From the results, it was concluded that the length of the REV was insufficient as inlet effects were still at play. This was derived from the observation that in the downstream direction, the progression of hydration was still significantly changing per particle. It was advised to increase the length of the REV to at least three times the size. For low Péclet numbers, when outlet effects are also to be taken into account, a further increase in length is likely to be necessary. However, since the current model already took 5 days to run, the practicality of such a large geometry is low. Therefore, advanced discretization methods such as the Immersed Boundary Method (IBM) may be able to provide a solution.

In a second study, emphasis was put on pressure drop and convective heat transfer in the REV, which were calculated by the model for a range of Reynolds numbers. Results from the model were compared with correlations from literature. Additionally, four particle contact modelling methods were compared: gaps (used in the hydration study), increase, bridges and caps. Regarding pressure drop, it was concluded that in general, pressure drop was underestimated by the model. Among the four methods, the caps method yielded results closest to the relations from literature. For $Re \leq 1$, an average relative error of 0.038 was found to the Kozeny-Carman (K-C) equation, while for $Re \geq 1$ an error of 0.132 was found to the Ergun equation. Regarding heat transfer, the same Reynolds number range was used to calculate the Nusselt number from the rate of convective heat transfer in the REV. Results were compared to the Wakao&Kaguei and Whitaker equations (valid for $Re \geq 20$) and Gnielinski equation (valid over the entire range). For low Reynolds numbers, a constant underestimation by the model was observed. For $Re \geq 10$, the results were in good concordance with the Gnielinski equation. Between the four geometries, the increase method had the closest match, followed by the caps method. It was recommended that when employing continuum methods to model porous media with spherical particles, the K-C and Ergun equations can be used for the pressure drop. For heat transfer, the Gnielinski equation can be used to determine heat transfer in the higher Reynolds number range, but for low Reynolds numbers no proper correlation is known yet. When choosing between the four particle contact modelling methods, either the caps (good pressure drop, acceptable heat transfer) or increase method (mediocre pressure drop, good heat transfer for high Reynolds numbers) was advised.

Contents

List of Figures

List of Tables

List of Symbols

A	Area [m^2]
A_f	Pre-exponential factor [1/min]
Bi	Biot number ($= hd_p/k_s$)
D_c	Diffusion coefficient [m^2/s]
E_a	Activation energy [J/mol]
K	Permeability [m^2]
L	Characterisic length [m]
M	Molar weight [kg/mol]
Nu	Nusselt number ($= hd_p/k_f$)
Pe	Péclet number ($= u_i d_p/D$)
Pr	Prandtl number ($= \nu/D_T$)
R	Ideal gas constant = 8.314 [J/molK]
Re	Reynolds number ($= u_s d_p/\nu$)
T	Temperature [K]
V	Volume [m^3]
ΔH	Reaction enthalpy [J/mol]
c	Concentration [mol/m^3]
c_p	Heat capacity [J/kgK]
d_p	Particle diameter [m]
h	Convective heat transfer coefficient [W/m^2K]
k	Thermal conductivity [W/mK]
m	Mass [kg]
p	Pressure [Pa]
q	Heat flux [W/m^2]
r	Radius [m]

t	Time [s]
u	Velocity [m/s]

Acronyms

CFD	Computational Fluid Dynamics
DNS	Direct Numerical Simulation
FCC	Face-centered cubic
IBM	Immersed Boundary Method
REV	Representative Elementary Volume
TCM	Thermo-chemical material
TES	Thermal Energy Storage

Greek symbols

α	Fractional conversion [-]
ϵ	Porosity [-]
μ	Dynamic viscosity [Pa·s]
ν	Kinematic viscosity $[\mathrm{m}^2/\mathrm{s}] = \mu/\rho$
ϕ	Sphericity [-]
ρ	Density $[\mathrm{kg/m}^3]$

Subscripts

c	concentration
eq	equilibrium
f	fluid
i	intersitial
m	modified
p	particle
s	superficial, solid
T	temperature
wv	water vapour

Chapter 1

Introduction

By signing the Paris Agreement in 2015, a large number of countries agreed to dedicate themselves to reducing the emission of greenhouse gases. In order to reach the goal of keeping the global temperature rise below two degree Celsius, a considerable improvement of energy efficiency is required. From the total energy consumption in the Netherlands, 38% is used for heating and almost half of that is used for the built environment [8]. Additionally, 46% of the total energy consumption of a Dutch household comes from space and water heating [1] (see figure 1.1). It is clear that reducing the energy consumption for heating plays an important role in reaching the Paris goals.

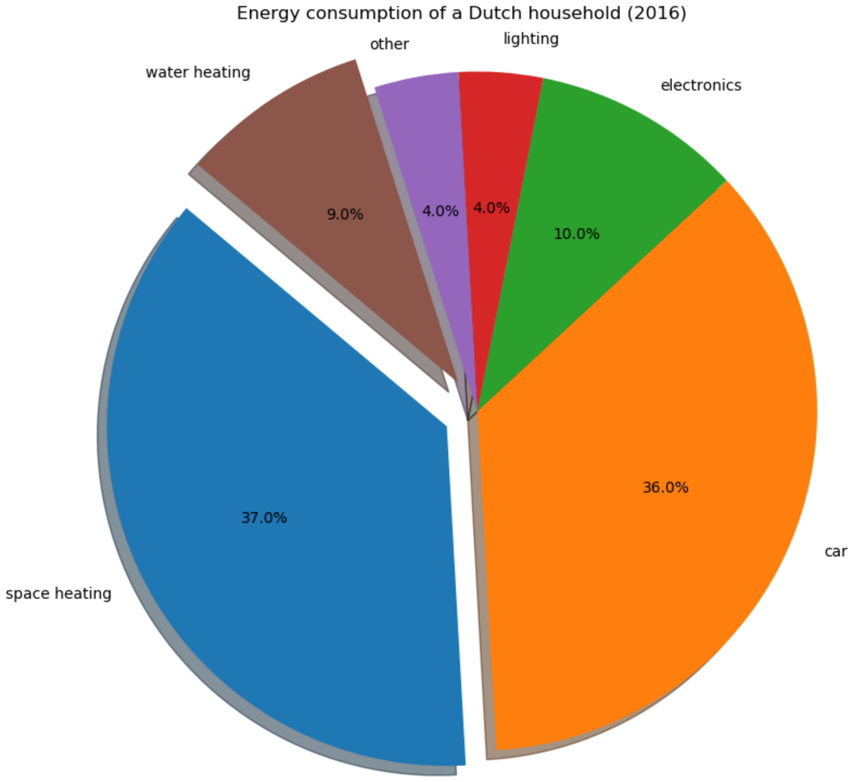

Figure 1.1: Energy consumption of a Dutch household. Space and water heating add up to 46% (2016 data, from the ECN [1]).

A promising way to do this would be to mitigate the energy demand/supply mismatch. In general, supply exceeds demand in summer and vice versa in winter. Using Thermal Energy Storage (TES), heat can be stored and used again at a later point in time. Supposing the energy is produced from renewable resources, there would be less dependence on conventional energy sources. Within the built environment, use can be made of seasonal heat storage: during summer, excess heat can be stored in seasonal storage tanks and used during winter time when the demand is exceeding the supply. For different applications, there are different types of TES.

1.1 Types of TES

In **sensible heat storage**, thermal energy is stored by using the heat capacity of the storage material. Therefore, heat is stored by increasing the temperature. The thermal energy that is stored is given by the following equation [3]:

$$Q = mc_p(T_{high} - T_{low}), \tag{1.1}$$

with m [kg] the storage material mass, c_p [J/kgK] the specific heat of the storage material and T_{high} and T_{low} the upper and lower temperatures [K]. Examples of this form of heat storage are aquifers, domestic water heaters and solar ponds. The major advantage of storing heat by using the heat capacity of liquids is that it can be easily transported. However, the overall heat storing capacity is low while thermal losses are high because of the temperature difference between the storage material and the ambient. In sensible heat storage, the amount of energy stored is directly proportional to the temperature difference. This is not the case in **latent heat storage**, which makes use of so-called phase change materials (PCMs). When heated or cooled, PCMs behave similar to sensible heat storage materials, but the phase changes solid$\Longleftrightarrow$liquid$\Longleftrightarrow$gas yield or take up additional energy. The bulk of the energy is therefore stored in the state of the material. The phase change itself occurs at constant temperature. This makes PCMs useful in applications where the temperature differences are small. However, the heat capacities of most PCMs are lower than those of the materials used in sensible heat storage. The thermal energy stored is given by the following equation [3]:

$$Q = m(c_p(T_{high} - T_{low}) + \Delta h_{PCM}), \tag{1.2}$$

where Δh_{PCM} [J/kg] is the specific enthalpy difference over the phase change. A suiting example is an ice bank storage installation, where energy is stored in the phase change water$\Longleftrightarrow$ice. The last category of TES is **sorbtion heat storage**. In this form, the majority of the heat is stored by using physical or chemical bonding energy and use is made of thermochemical materials (TCMs). This can be done both in solids (solid sorbtion) and in liquids (liquid sorbtion). Solid sorbtion is further differentiated into chemisorbtion and physisorbtion. In chemisorbtion, the sorbtion is on molecular level into the crystal structure, affecting the composition and morphology of the sorbent, while physisorbtion takes place at the surface of the material and does not affect the sorbent structure. The thermal energy stored is given by the following equation [3]:

$$Q = m(c_p(T_{high} - T_{low}) + \Delta h_{TCM}), \tag{1.3}$$

where Δh_{TCM} [J/kg] is the specific enthalpy difference over the sorbtion reaction. One of the advantages of TCMs is that their overall heat storage capacity is higher than the other forms of TES. Two examples of TCM systems are Desiccant Cooling systems and ammonia absorption chillers. The resulting energy densities for the forms of heat storage that are described above are visualized in figure 1.2.

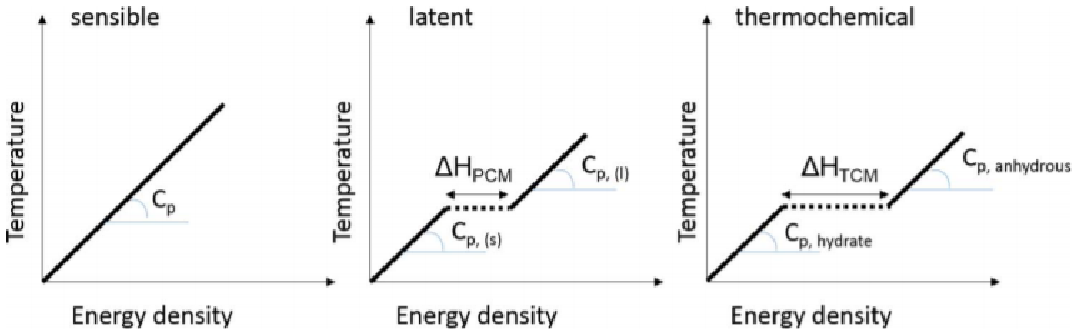

Figure 1.2: Energy densities for different forms of heat storage. In PCM and TCM applications, the phase change or chemical reaction causes the jump in density at constant temperature which can be advantageous in systems with small temperature differences. From [2].

When charging TCM systems hot and dry air is flown through the *sorbent* bed, which is hydrated with the *sorbate*. Heat is transferred to the bed and water is taken up by the flow. In discharging mode, the reverse takes place: cold and moist air is now flown through the bed where it transfers the sorbate to the bed and takes up the heat generated by the hydration reaction. This also brings forward the main advantage of TCM systems: heat is only generated when water is absorbed, so energy losses during storage are minimal. The majority of the materials used as sorbent are salts. The hydration/dehydration is described by a reversible chemical reaction of the following form:

$$\mathrm{A(s)} + \mathrm{B(g)} \rightleftharpoons \mathrm{C(s)} + \mathrm{heat}, \tag{1.4}$$

in which A is the dehydrated salt, B the water vapor and C the hydrated salt. It can easily be seen that the rightwards direction is exothermic as it generates heat, this is the hydration reaction. Two different system configurations are used for TCM heat storage, which are shown in figure 1.3. In an open system, air is drawn from the ambient and flow is usually provided by a fan. In charging mode, air is heated by a heat exchanger after which it charges the TCM bed by transferring its thermal energy to it. In discharging mode a fan forces moist air through the TCM bed which then discharges its thermal energy. This energy can then be used for heating purposes. The open system operates at ambient pressure. The working fluid -often air- is discharged directly into the surrounding ambient air. Due to this, only non-toxic sorbates like water can be used. Closed systems on the other hand are not in direct connection with the environment. Advantageous to the closed layout is that no fan is required, due to the vapour pressure that acts as driving force. Additionally, closed systems can provide higher temperature outputs although also higher charging temperatures are required. One of the primary disadvantages of closed systems is that the energy density of the system is lower than in open systems due to the inclusion of a water storage tank [9]. Michel et al. [10] compared the reaction rates of open and closed TCM systems and concluded that closed systems are limited by heat transfer: when the thermal power output is low it can be substantially improved by increasing the thermal conductivity. Conversely, open systems are limited by mass transfer: increasing the bed permeability is beneficial to the reaction time and thus to the power output. Other components in TCM systems include heat exchangers and water pumps.

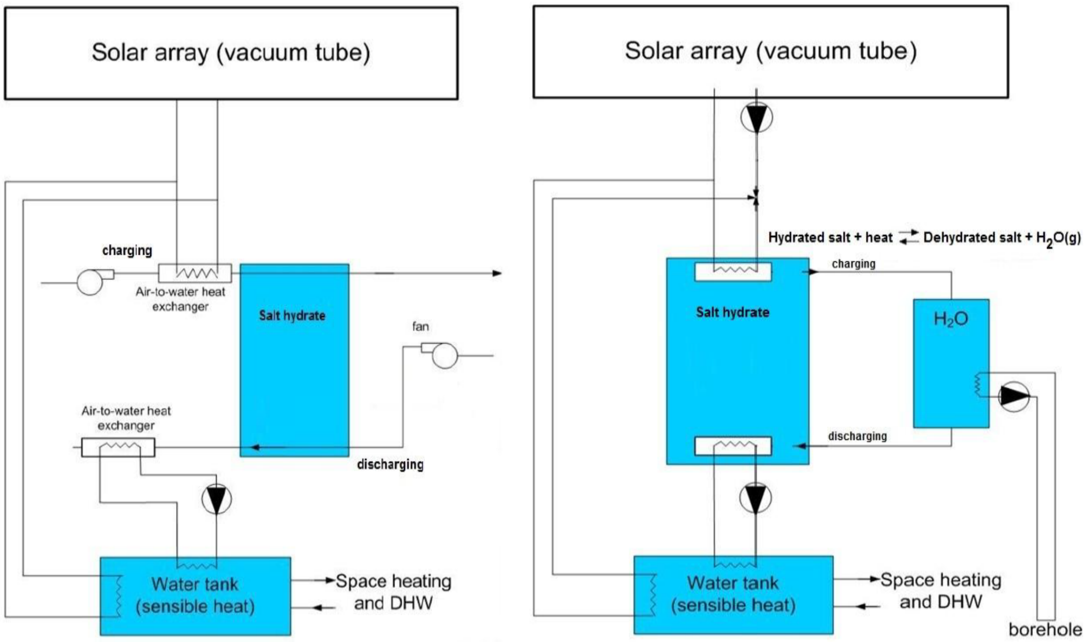

Figure 1.3: Thermochemical heat storage systems (left) open sorbtions system, (right) closed sorbtion system. In closed systems the working fluid does not leave the system and heat is only exchanged through heat exchangers. From [3].

1.2 K_2CO_3 as TCM

Salt hydrates are extensively used materials for solid sorbtion. Water vapor is mostly used as sorbate. Due to the polarity of the salts and water, a significant binding energy exists in salt hydrates [3]. There are numerous salt hydrates which all have unique characteristics and as a result it has been a popular topic among researchers. In salt hydrate performance evaluation, the emphasis is often put on power output and thermal efficiency. In the work of Donkers et al. [2], 563 reactions were evaluated on their thermal efficiency, power output, temperature range and stability, among other aspects. K_2CO_3, which is a relatively new salt in the context of energy storage, showed a promising overall performance. Although energy density was lower compared to other evaluated materials, it was chosen as preferred TCM due to its stability, lack of energy loss during storage, weak corrosivity and low dehydration temperature. In the modelling framework, K_2CO_3 brings another advantage as it hydrates in only one step: from anhydrous to sesquihydrate. The hydration/dehydration reaction is

$$\mathrm{K_2CO_3(s) + 1.5H_2O(g) \rightleftharpoons K_2CO_3 \cdot 1.5H_2O(s) + \Delta H} \tag{1.5}$$

The reaction from left to right is exothermic and produces heat ΔH. According to Washburn [11], ΔH is 62.5 kJ per mol water. This results in a bulk energy density of 1.56 GJ/m^3. In figure 1.4 the phase diagram of K_2CO_3 is shown. When hydrating, the phase changes from the area under the blue line in the light grey area to the area between the blue and red lines in the grey area. A second phase change can occur if the water vapour pressure is increased even further, when deliquescense will occur: the salt will dissolve in the water and all porosity is lost, even when re-solidifying (dark grey area). As diffusion of water through the material is reduced, reaction rates drop significantly and less thermal power can be generated.

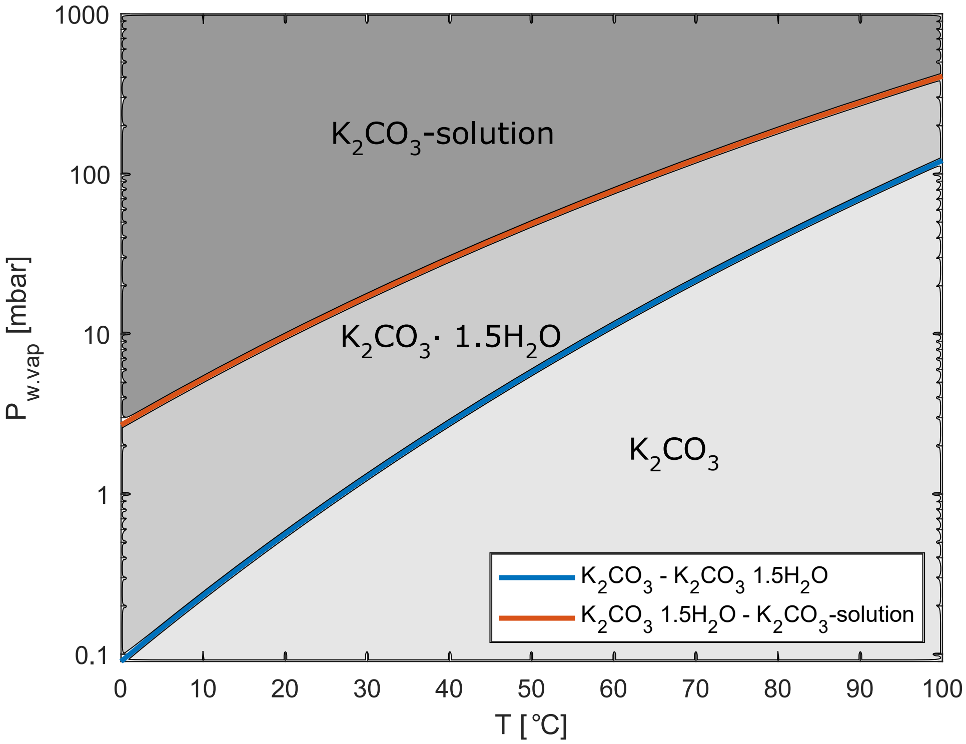

Figure 1.4: Phase diagram of K_2CO_3 with data from [2]. Dehydration occurs under the conditions in the light grey area under the blue line, while hydration occurs under conditions in the light grey area between the blue and red lines. Under conditions in the dark grey area, the material is in deliquescent state.

1.3 Modelling of heat batteries

Modelling heat batteries (or porous media in general) can be done using several approaches. With the continuum method, the reactor volume is regarded as one uniform volume. Internal geometric details are not included. Empirical laws are used to quantify pressure drop, porosity and heat and mass transfer. Advantageous to this is that little computational effort is required, as the equations that are to be solved are not overly complicated. Obtained results have shown to be in good agreement with experiments, as was illustrated in the work of Gaeini [12], where the hydration of a zeolite heat battery was modelled using the continuum approach. Pressure drop over the reactor, water concentration and temperature profiles corresponded to what was experimentally obtained. Similarly, research by Favergeon et al. [13] and Fopah-Lele et al. [14] provided satisfactory results for the dehydration of kaolinite and the hydration of magnesium chloride.

The second method uses Direct Numerical Simulation (DNS). In contrast to the continuum method, the internal geometry is fully modelled using finite elements. Flow is characterized through the discrete Navier-Stokes equations. This was done for example in the thesis of Lan [15]. The main advantage over the continuum method is that greater accuracy is achieved and that virtually all spatial detail from macro to micro scale is available. Wall effects can be visualized and if present, even turbulence. The advantage of discrete over continuum modelling for heat transfer in packed beds was also shown in the work of Burström et al. [16]. It was advised to use DNS if the local heat transfer effects were of interest. However, since computational times were significantly larger, continuum models would suffice if only mean predictions over the bed were desired.

1.3.1 Representative Elementary Volume modelling

When modelling packed beds, often use is made of Representative Elementary Volumes (REVs). These periodic, repetitive volumes can be utilized to minimize the computational effort required to model packed beds. Because the properties of an REV are the average of the complete reactor, this method is regarded as a middle-of-the-road compromise between DNS and continuum. A properly defined REV is representative of the bulk of the bed and must be applicable to any arbitrary location (with the exception of the in- and outlet areas). It must therefore contain locally correct portions of fluid and solid [17]. Therefore, in- and outlet effects must be avoided. In this thesis, use is made of an REV. In this way, the domain can be kept small, while still being able to visualize effects on micro scale and representing the packed bed reactor.

1.4 Aim of the thesis

Although a large amount of experimental research has been conducted on TCM heat storage, their numerical counterparts have had relatively little exposure. Additionally, the numerical modelling that has been done on this topic has for the most part been on the dehydration process and not on hydration [6,18–22]. The modelling of salt hydration for TCM applications is important due to the fact that it can provide useful insight on the performance of materials and configurations without the need of expensive experimental setups. Furthermore, the utilization of DNS in this task can provide accuracy and additional spatial detail that would not be available with the limitations of the continuum method. Therefore, the main objective of this thesis is to develop a DNS model that can simulate the hydration process of a (part of a) K_2CO_3 heat battery reactor. Emphasis will be put on the rate of hydration, heat transfer and pressure drop. To this end, use is be made of the open-source Computational Fluid Dynamics (CFD) software OpenFOAM, in which an REV of the reactor will be modelled. First, a geometry is modelled and meshed. This geometry does not cover a complete reactor, but is a representation. Using this geometry, the hydration process is simulated. Additionally, the pressure drop over the geometry and the heat transfer coefficient is compared with results from literature. Also the effect of the chosen particle contact modelling method is investigated. To frame it in research questions:

1. How does the hydration of the REV progress over time? What are the effects of inlet water vapour concentration? Can the REV be used to represent the packed bed?
2. When investigating pressure drop and heat transfer, do the results agree with values from literature? If not, what can be done to improve accuracy? Additionally, what is the effect of the particle contact modelling method?

1.5 Outline of the thesis

Chapter 2: Relevant background and theory on salt hydration and CFD modelling is provided. Correlations for pressure drop and heat transfer are listed. Different reaction models are explained and a description is given on how geometry modelling and meshing can be approached.

Chapter 3: A detailed description of the model is given. The geometry of the REV is described, as well as the meshing parameters. The solution strategy is provided. The results of the hydration process are also presented.

Chapter 4: A comparison is made between the pressure drop and heat transfer results obtained from the model and values from literature. The influence of the particle contact modelling methods is discussed.

Chapter 5: The conclusions of the thesis are presented, along with the recommendations.

Chapter 2

Theory

In this chapter the relevant theoretical background of heat batteries and packed beds is provided. Important equations are stated which are used in the packed bed hydration model, additional to correlations from literature that can be employed when using continuum methods. This chapter starts with what packed beds are and how their complex geometries can be modelled. Subsequently, the physical processes at play in the packed bed reactor are discussed, along with equations from literature that can be used to characterize them. Finally, an overview is provided of the different reaction models that can be used when modelling salt hydration.

2.1 Packed beds

Heat batteries often make use of packed bed columns. In these containers particles are randomly stacked and air can be flown through the resulting voids. In characterizing a porous medium, use is made of the porosity ϵ, which is synonymous to the void fraction of a solid material:

$$\epsilon = \frac{V_V}{V_T}, \tag{2.1}$$

with the total volume of the voids V_V and the total solid volume V_T. In a porous medium, fluids are able to flow through the volume's pores. The velocity of the fluid is often expressed as the Darcy velocity. This Darcy velocity or Darcy flux is not the actual velocity with which the fluid is flowing through the medium, but the flow per unit of cross sectional area, and this is illustrated in figure 2.1. The actual or interstitial velocity can be obtained by dividing the Darcy velocity by the porosity:

$$u_i = \frac{u_s}{\epsilon} \tag{2.2}$$

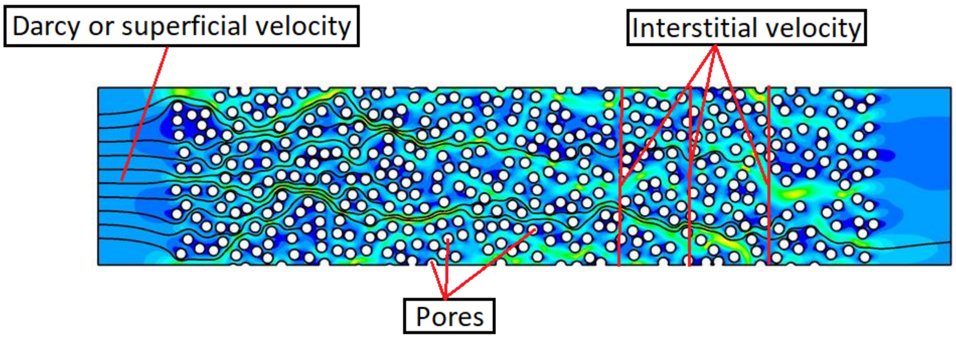

Figure 2.1: Velocity plot of a CFD study of flow through a porous medium. A fluid is flown through a medium with several pores. At the inlet, where no solid material is present, the interstitial velocity equals the Darcy or superficial velocity (as $\epsilon = 1$). Further downstream the pores will cause the interstitial velocity to increase ($\epsilon < 1$). This interstitial velocity is taken as the average over a plane normal to the flow direction (illustrated with the red lines). Taken and adapted from [4].

2.1.1 Packing of particles

The particles in packed beds can be arranged is different ways: fixed or random. In fixed configurations, all particles are positioned in consistent fashion throughout the reactor. There are several

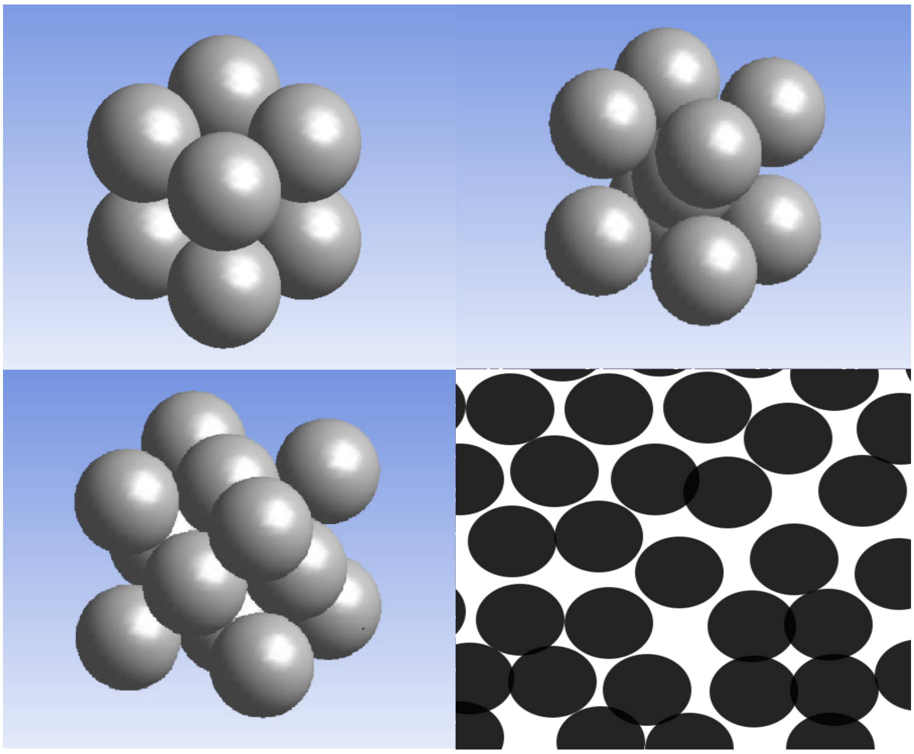

Figure 2.2: Four different types of packing. Top left: simple cubic; top right: body-centered cubic; bottom left: face-centered cubic; bottom right: 2D random packing.

different fixed packings, but the three most often encountered are simple cubic (SC), body-centered cubic (BCC) and face-centered cubic (FCC). In a random packing the particle positions are irregular. In figure 2.2 the four mentioned types of packing are shown. The porosity is the lowest for FCC structures (≈ 0.26), followed by BCC (≈ 0.32) and SC (≈ 0.48) and they can be calculated mathematically. In determining the porosity of random packings, balls are poured in a volume and shaken by a vibrator. The total occupied volume is determined by measuring the height of the top ball to calculate the total occupied volume. The solid volume is determined by counting the number of balls used. Because this process is random and not fully repeatable it is difficult to give unambiguous results. However, the maximum recorded porosity in literature is 0.4 [23]. In this thesis, a regular FCC packing is used, due to its low porosity, which requires less required mesh elements. Furthermore, there are reports of crystallization (disorder-order transition) of spheres into an FCC lattice after being subjected to 3D vibration [24].

2.1.2 Modelling of a packed bed geometry

Modelling a packed bed can be a cumbersome task. Small voids and narrow passages require a fine grid that is able to capture the complex curvatures. In packed beds that consist of spherical particles, the main issue arises from the contact points between adjacent spheres. Theoretically, the contact area between two touching spheres is singular and zero-dimensional; the area equals zero as it consists of a single point. This can cause extremely skewed cells (which in turn causes convergence problems) when such a geometry is meshed. Because the quality of the mesh is of great influence on the accuracy of the results, this issue has to be addressed. This can be done with several methods, as listed by Dixon et al. [5] and shown in figure 2.3:

(a) By **shrinking** the particles by a certain percentage, while retaining their relative positions, gaps are created. These gaps allow for a number of cells between the particles. This eliminates degraded mesh due to skewed cells completely. The porosity of the geometry is increased by the shrinking. Thermal conduction can only be included “virtually” by generating a list of particle neighbours, assuming a contact area and calculating and applying the theoretical heat transfer through conduction. Shrinking the particles is a popular practice [25–28]. Among the four methods, it can yield the highest mesh quality. However, the degree of shrinking must be determined carefully. With insufficient shrinking, elements near the contact points are still too skewed; shrinking too much causes the flow patterns to change dramatically. Several sources claim shrinking the particle by 1% gives a good compromise between mesh quality and accuracy [26, 27] , while others are satisfied with 2% [28].

(b) By **increasing** the particle in size, adjacent particles will overlap and a circular contact area will form. The mesh cells will be less skewed, but quality may still be insufficient due to the crazes at the contact area. The porosity of the geometry decreases due to this operation. For thermal conduction the contact area between two particles may need to be adjusted.

(c) When creating **inter-particle bridges** the particle radius will not change. A cylindrical bridge is created, with its axis through the sphere centres. Mesh quality will increase depending on the bridge radius. The porosity of the geometry decreases. For thermal conduction the contact area between two particles may need to be adjusted.

(d) **Capping** the particles is the opposite of creating bridges. At the contact site, a slice of both particles is taken away. This will create a gap between two circular areas. The porosity of the geometry increases when using this method. Similarly to shrinking the particles, this method will eliminate the contact area between two particles. Thermal conduction therefore has to be calculated and applied separately.

In Chapter 3, the gaps method is employed to model an REV of spherical particles. Due to its ease of implementation and relatively high resulting mesh quality, it is the ideal candidate for the hydration study. In Chapter 4, the four methods mentioned above are evaluated on their effect on pressure drop and heat transfer.

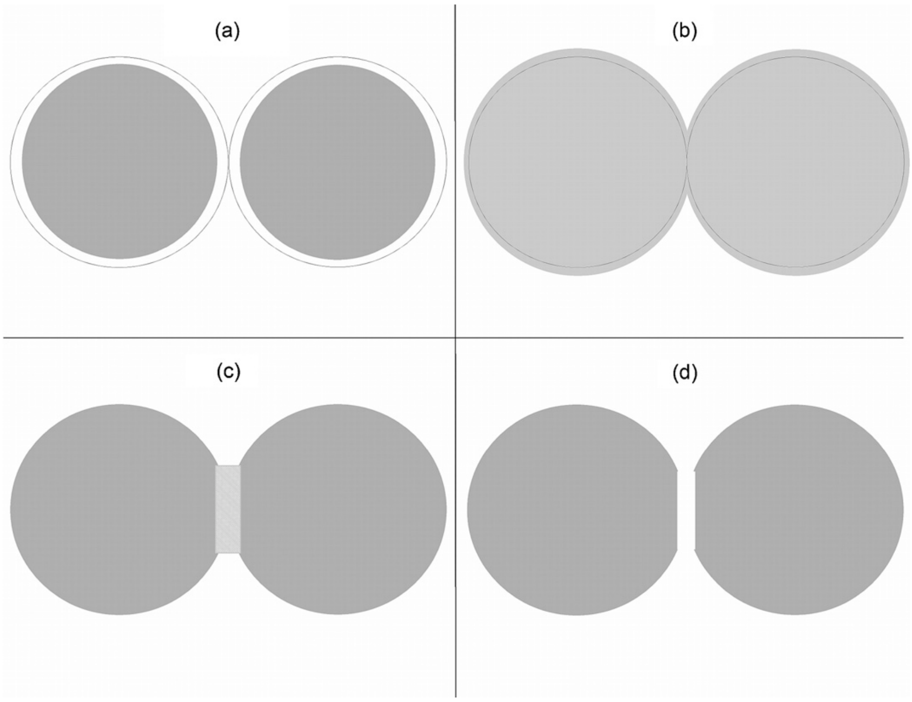

Figure 2.3: Four methods of tackling the particle contact problem: (a) particle shrinking; (b) particle overlap; (c) inter-particle bridging; (d) particle capping [5].

2.2 Physical processes in packed beds

Heat and mass transfer take place simultaneously in the packed bed reactor. When discharging for example, heat is transferred from the particles to the working fluid and transported throughout the bed. Within the particles, heat is generated by the hydration reaction. Simultaneously, water is transported to the particles by the working fluid. It must be noted that in this thesis, the transport of these scalar quantities (temperature and water concentration) is considered to be decoupled: it does not affect the flow field. In this section the most important mechanisms of flow, heat transfer and mass transfer are discussed.

2.2.1 Heat transfer at the particle-fluid interface

The particle surfaces are perhaps the most interesting regions in the packed bed reactor. At these solid-fluid interfaces the transfer of heat and mass takes place by convection. Convection is quantified by the convective heat transfer coefficient h [W/m^{2}K]. Within the particles, heat is generated by the hydration reaction. This heat diffuses throughout the particle by conduction. The ease with which the heat is conducted in solids is characterized by the thermal conductivity k_s [W/mK]. When conduction is the dominant heat transfer mechanism, the temperature distribution in the solid body can be regarded as constant as heat diffuses through the solid medium rapidly. A steep temperature gradient will exist at the boundary. When convection is dominant, the temperature distribution cannot be considered as uniform; temperature near the interface will be significantly closer to the ambient when compared to the center.

To characterize certain physical aspects of the reactor, use is made of dimensionless numbers. The ratio of conduction in solids and convection to the environment is defined by the Biot number

$$Bi = \frac{hL}{k_s}, \tag{2.3}$$

where L [m] is the characteristic length scale and k_s [W/mK] is the thermal conductivity of the solid. In the case of a sphere L is equal to the particle diameter d_p [m]. In case that $Bi < 1$, conduction is dominant and for $Bi > 1$ convection is the dominant mechanism. While k is a material property, h is dependent on ambient conditions and fluid properties. The Nusselt number is the ratio of heat transfer through convection to conduction:

$$Nu = \frac{hL}{k_f}, \tag{2.4}$$

where k_f [W/mK] is the thermal conductivity of the fluid. The Nusselt number can generally be expressed as a function of the Reynolds and Prandtl numbers:

$$Re = \frac{u_s d_p}{\nu} \tag{2.5}$$

$$Pr = \frac{c_{p,f}\mu}{k_f} = \frac{\nu}{D_T} \tag{2.6}$$

In these dimensionless numbers, u_s [m/s] is the superficial flow velocity, d_p [m] is the particle diameter, ν [m^2/s] is the kinematic viscosity, $c_{p,f}$ [J/kgK] is the heat capacity of the fluid, μ [Pa$\cdot$m] is the dynamic viscosity and D_T [m^2/s] is the coefficient of thermal diffusion. The Reynolds number is the ratio of inertial forces to viscous forces and can be used to determine if a flow is laminar or turbulent (flow with $Re > 3500$ is generally considered turbulent). The Prandtl number is not a characteristic of the flow, but a material property: it is the ratio of momentum diffusivity to thermal diffusivity. For materials in which $Pr > 1$ momentum diffuses away through shear forces between fluid layers more rapidly than heat.

Within the working fluid, scalar quantities like temperature and concentration are transported by advection (= transport by the bulk motion) and diffusion (= transport due to temperature/-concentration gradient). One of these may play a greater role than the other, and therefore use is made of the Péclet number, the final dimensionless numbers that is addressed here. As it is the ratio of advection to diffusion, it is defined as:

$$Pe = \frac{u_i d_p}{D} = \frac{Re}{\epsilon} Pr \tag{2.7}$$

D [m^2/s] is the diffusion coefficient of the scalar in the working fluid and can be used for an arbitrary scalar quantity. It must be noted that the interstitial velocity is used here. In a flow with $Pe > 1$, diffusion is insignificant compared to advection. The Péclet number can be used to determine if downstream developments in the flow need to be taken into account. For flows with high Péclet numbers, which is the majority in engineering applications, downstream dependency is not relevant.

Over the years, numerous Nusselt relations have been proposed. Unfortunately, none of them are universally applicable. For a single sphere in a laminar open stream for example, Ranz and Marshall [29] proposed the following relation which they derived from experimental values:

$$Nu = 2 + 0.6Re^{1/2}Pr^{1/3} \tag{2.8}$$

This relation is sometimes (wrongfully) generalized and used in problems where it is far from applicable. For packed beds, there are more appropriate relations. Wakao and Funazkri [30] experimentally investigated mass transfer in packed beds consisting of spherical particles and came up with an equation to relate the Schmidt number (ratio of momentum diffusivity to mass diffusivity) to the Sherwood number (ratio of convective mass transfer to diffusive mass transfer). Since mass transfer can be regarded analogous to heat transfer, their equation can therefore also be used to relate the Prandtl number to the Nusselt number, which was shown by Wakao and Kaguei [31]:

$$Nu = 2 + 1.1 Re^{1/2} Pr^{0.6}, \tag{2.9}$$

which is valid for $15 < Re < 8500$. While the previous two relations do not account for the porosity of the material, there are several that do. Whitaker's work [32] contrasted from work of other authors mentioned here in the sense that it used dimensional analysis to fit heat transfer functions to previously obtained experimental data. Nusselt correlations were proposed for several cases, including laminar and turbulent flow in pipes, laminar and turbulent flow over flat plates and flow in staggered bundles. For flow through a porous medium, Whitaker proposed

$$Nu = \frac{1-\epsilon}{\epsilon}\left(0.5\left(\frac{Re}{1-\epsilon}\right)^{1/2} + 0.2\left(\frac{Re}{1-\epsilon}\right)^{2/3}\right)Pr^{1/3}, \tag{2.10}$$

under experimental conditions of $Pr = 0.7$, $20 < Re < 80000$ and $0.333 < \epsilon < 0.778$. Meng et al. [33] derived their relation by conducting experiments using a water-cooled pebble bed reactor:

$$Nu = 3.212(Re\frac{1-\epsilon}{\epsilon})^{0.335} Pr^{0.438}, \tag{2.11}$$

valid for $12000 < Re < 13000$ and $\epsilon \approx 0.338$. Another relation derived from experimental data is from the Kerntechnische Ausschuss (KTA) [34]

$$Nu = 1.27 Re^{0.36}\frac{Pr^{1/3}}{\epsilon^{1.18}} + 0.033 Re^{0.86}\frac{Pr^{1/2}}{\epsilon^{1.07}} \tag{2.12}$$

The fact that most of the Nusselt relations are only applicable under very specific circumstances, transpires for example from the required conditions for equation 2.12. It is was established under the following experimental conditions: $0.36 \leq \epsilon \leq 0.42$; $10^2 \leq Re \leq 10^5$; $D/d_p \geq 20$; $H/d_p \geq 4$, in which the last two conditions are the ratio of reactor diameter to particle diameter and ratio of reactor height to particle diameter, respectively. A last relation to be addressed here is one proposed by Gnielinsky [35]. His approach is based on the analogy of heat transfer across a flat plate and that this mechanism can be applied to arbitrary geometries. The characteristic length scale is the length over which heat transfer can occur, which in case of a particle is its diameter. His relation consists of the asymptotic solutions for laminar and turbulent heat transfer:

$$Nu_l = 0.664\left(\frac{Re}{\epsilon}\right)^{1/2} Pr^{1/3} \tag{2.13}$$

$$Nu_t = \frac{0.037\left(\frac{Re}{\epsilon}\right)^{0.8} Pr}{1 + 2.443\left(\frac{Re}{\epsilon}\right)^{-0.1}\left(Pr^{2/3} - 1\right)} \tag{2.14}$$

$$Nu_{sp} = 2 + (Nu_l^2 + Nu_t^2)^{1/2} \tag{2.15}$$

This determines the Nusselt number for a single sphere. To find the Nusselt number for a packed bed, an arrangement factor $f(\epsilon)$ is applied:

$$Nu = f(\epsilon)Nu_{sp} = (1 + 1.5(1 - \epsilon))Nu_{sp} \tag{2.16}$$

It was shown that predictions from this relation were accurate for $500 < Re < 10^6$ [36]. However, in the lower Reynolds region, reported experimental results were lower than what Gnielinski's relation predicts.

Using DNS, the convective heat transfer coefficient can be determined "the other way around". This can be done under the assumption that the velocity near the fluid-solid interface is zero, implicating that heat transfer at this interface occurs solely through diffusion. The heat flux q [W] transferred to or from solid bodies in a control volume is equal to the energy difference between the flow that passes through the inlet and when it leaves through the outlet of the control volume (conservation of energy). Given a known surface A [m^2] through which the heat transfer occurs, the free stream fluid temperature T_f [K] and the solid (wall, particle surface) temperature T_s [K], the heat transfer coefficient is calculated through

$$h = \frac{q}{A(T_f - T_s)} \tag{2.17}$$

In packed beds there is no unambiguous definition of a free stream temperature T_f and therefore the bulk temperature of the fluid T_b can be used [37]. To calculate a representative average T_{in}, T_{out} or T_f, often a weighted-by-flux cup-mixing temperature is used [38] (the superficial flow is along the x-axis):

$$T_{mix} = \frac{\int u_x(x,y,z)T(x,y,z)dV}{\int u_x(x,y,z)dV}, \tag{2.18}$$

where u_x is the x-component of the velocity and V is the infinitesimal volume over which the temperature T is evaluated. This is done under the assumption that temperature in low-velocity locations contributes less to the average temperature. The advantage of the cup-mixing temperature over the regular volume-averaged temperature was shown in the work of Singhal et al. [39]. In numerical studies this temperature can be easily calculated by averaging over the domain volume, but this is often not the case in experimental studies. Therefore, an approximated bulk mean temperature $T_{bm} = (T_{in} - T_{out})/2$ can be used [40]. In the case of a fluidized packed bed reactor [41–43] where particles are moving in counterflow with the working fluid, the logarithmic mean temperature difference is used instead

$$\Delta T_{lm} = \frac{(T_{s,out} - T_{f,in}) - (T_{s,in} - T_{f,out})}{\ln\left(\frac{T_{s,out} - T_{f,in}}{T_{s,in} - T_{f,out}}\right)}, \tag{2.19}$$

with $T_{s,in}, T_{s,out}$ the inlet and outlet temperatures of the solid phase and $T_{f,in}, T_{f,out}$ the inlet and outlet temperatures of the fluid phase.

In the work of Dave et al. [44] numerical Nusselt values were compared to several of the mentioned relations. Similar to this thesis, an FCC unit cell was used to obtain the heat transfer coefficients and derive the corresponding Nusselt numbers, which was then compared to the Nusselt numbers from the correlations from literature. Using Large Eddy Simulation and $k - \varepsilon$ turbulence modelling, it was concluded that these numerical results did not match with the relations derived from experiments, with the exception of equation 2.11 from Meng. Also in the work of Ahmadi Motlagh and Hashemabadi [45] a CFD study was conducted to investigate similarities in heat transfer between numerical values and correlations from literature. For cylindrical particles in cross flow and using a $k - \varepsilon$ turbulence model, it was found that the model was able to predict the

Nusselt number with an average error of 3.7% to the Zhuhauskas [46] and Whitaker relation [47]. However, this was done for $Re > 6300$. More relevant to this thesis, Das et al. [48] developed a numerical model using the Immersed Boundary Method to model heat transfer in a randomly packed slender column, with Reynolds numbers up to 500. Focusing on the wall-to-bed heat transfer, they compared their model to the relation by Yagi and Wakao [49] and found that Nusselt values as close as within 10% could be obtained over the entire Reynolds number range.

2.2.2 Temperature transport in porous media

In the reactor, transport of heat takes place in different forms. **Convection-diffusion** is the foremost form of heat transport and is characterized by the convection-diffusion equation

$$\frac{\partial T}{\partial t} + \boldsymbol{u} \cdot \nabla T = D_T \nabla^2 T, \tag{2.20}$$

where $\boldsymbol{u}$ [m/s] is the velocity vector and the thermal diffusivity D_T is defined as the thermal conductivity k_f [W/mK] divided by the density ρ_f [kg/m^3] and heat capacity $c_{p,f}$ [J/kgK] of the fluid:

$$D_T = \frac{k}{\rho_f c_{p,f}} \tag{2.21}$$

Equation 2.20 describes the transport of temperature through the flow domain. The first term on the left hand side (LHS) is included when considering time-dependent problems. The second term on the LHS describes convection/advection: temperature is transported through motion of the working fluid. The term in the right hand side (RHS) describes diffusion: temperature is transported due to a temperature gradient being present throughout the domain.

In the packed bed that is used in this thesis, the solid domain is composed of spherical particles. Due to the Biot number being smaller than 0.1 (see Appendix C), the particle temperature is considered to be independent of the radial coordinate. Therefore, the temperature T_p of a particle with radius r can be evaluated using the following equation:

$$V \rho_s c_{p,s} \frac{\partial T_p}{\partial t} = qA + S, \tag{2.22}$$

with:
V the particle volume ($= \frac{4}{3}\pi r^3$) [m^3]
ρ_s the particle density [kg/m^3]
$c_{p,s}$ the particle material heat capacity [J/kgK]
q the convective heat flux per surface area [W/m^2]
A the particle surface ($= 4\pi r^2$) [m^2]
S the energy source term

The first term on the RHS of equation 2.22 is derived from Newton's law of cooling/heating combined with Fourier's law of conduction. Starting with Newton's law of cooling for heat flux q [W/m^2]:

$$q = h(T_\infty - T_p), \tag{2.23}$$

where h [W/m^{2}K] is the convective heat transfer coefficient and T_∞ is the free stream temperature. Realizing that $\boldsymbol{u} = 0$ at the particle surface, it is assumed that heat transfer occurs only through conduction. Fourier's law $q = -k\nabla T$ can be rewritten for a unidirectional heat flux using Fourier's equation with the normal vector on the solid surface pointing outwards:

$$q = -k_f \overline{\frac{\partial T}{\partial n}}, \tag{2.24}$$

where the average normal gradient on the solid surface is used in the calculation. The second term on the RHS of equation 2.22 is the reaction term S, which represents the heat production from chemical reaction 1.4. This term can be expressed as:

$$S = \Delta H \frac{\rho_s V}{M_s} \frac{\partial \alpha}{\partial t}, \tag{2.25}$$

where ΔH [J/mol] is the specific enthalpy difference between reactants and products, M_s [kg/mol] is the molar weight of the solid reactant and $\frac{\partial \alpha}{\partial t}$ [1/s] is the reaction rate. Substituting equations 2.24 and 2.25 into equation 2.22, the energy balance of a particle now is

$$\frac{\partial T_p}{\partial t} = -\frac{k_f A}{\rho_s c_{p,s} V} \overline{\frac{\partial T}{\partial n}} + \frac{\Delta H}{M_s c_{p,s}} \frac{\partial \alpha}{\partial t} \tag{2.26}$$

In most cases, heat transfer through **conduction** is less significant in packed beds. Conduction between solid bodies takes place through touching surfaces. However, the contact area between two touching spherical particles does not have a straightforward definition. The singular contact point mentioned in section 2.1.2 does not allow for conduction as the area equals zero. However, in packed beds, the gravitational loading may compress the particles slightly, such that a circular contact area is created. According to [50], the radius of this contact area can be expressed by

$$r_c = \left[\frac{3(1-\nu_p^2)}{4E_s} f r \right]^{1/3}, \tag{2.27}$$

where ν_p [-] is the Poisson ratio of the solid material, E_s [N/m^2] is the Young modulus, f [N] is the colinear force and r [m] is the particle radius. Through this contact area, heat conduction is described by Fourier's law

$$Q = -kA\nabla T, \tag{2.28}$$

where Q is the heat flux in [W], $A = 2\pi r_c^2$ the surface area of the contact area circle and k is the thermal conductivity [W/mK]. The last form of heat transfer, **radiation**, does not play a significant role in packed beds, as temperature differences between two adjacent particles are relatively small [50].

2.2.3 Mass transport in porous media

In the packed bed reactor, mass is transferred between the particles and the working fluid. Transport of mass, or concentration c [mol/m^3], is assumed to be decoupled and takes place in a fashion similar to the transport of temperature (equation 2.20)

$$\frac{\partial c}{\partial t} + \boldsymbol{u} \cdot \nabla c = D_c \nabla^2 c, \tag{2.29}$$

with D_c [$\mathrm{m^2/s}$] the diffusion coefficient of water vapour in air. This equation describes convection and diffusion in the flow domain. At the particle surface, mass is transferred between the flow and solid domain. Again bearing in mind that the flow velocity equals zero at the boundary, it is assumed that mass transfer only takes place through diffusion. Therefore, the particle mass balance takes on a form similar to the energy balance equation 2.26:

$$\frac{\partial c}{\partial t} = AD_c\overline{\frac{\partial c}{\partial n}} + \frac{\rho_s V}{M_s}\frac{\partial \alpha}{\partial t} \tag{2.30}$$

In this equation the first term on the RHS comprises the water uptake through diffusion at the surface and the second term describes the water uptake related to the reaction rate. However, now it is assumed that there is no accumulation of water in the particle ($\frac{\partial c}{\partial t} = 0$). This reduces equation 2.30 to

$$AD_c\overline{\frac{\partial c}{\partial n}} = -\frac{\rho_s V}{M_s}\frac{\partial \alpha}{\partial t} \tag{2.31}$$

2.3 Flow modelling

Characterization of the flow in a reactor bed can be done in several different ways. In most cases a balance between detail in results and computational effort has to be found. In this section the two most used methods are discussed.

2.3.1 Direct Numerical Simulation

The method that provides the highest spatial resolution is Direct Numerical Simulation (DNS). It is a type of CFD simulation that solves the Navier-Stokes equations in all three Cartesian coordinates. In this thesis flow is assumed to be incompressible, which reduces the equations of conservation of mass and momentum to the following differential form:

$$\nabla \cdot \boldsymbol{u} = 0 \tag{2.32}$$

$$\boldsymbol{u} \cdot \nabla \boldsymbol{u} = \nu \nabla^2 \boldsymbol{u} - \frac{1}{\rho_f}\nabla p, \tag{2.33}$$

with the fluid density ρ_f [$\mathrm{kg/m^3}$], the kinematic viscosity ν [$\mathrm{m^2}$] and the pressure p [Pa]. To include passive transport of a scalar such as the concentration of a species c [$\mathrm{mol/m^3}$] the convection-diffusion equation can be used:

$$\boldsymbol{u} \cdot \nabla c = D_c \nabla^2 c \tag{2.34}$$

In the incompressible case also temperature is regarded as a decoupled scalar, and therefore the energy conservation can be described by an equation similar to equation 2.34.

Because no assumptions are made regarding the resolving of the flow field, the flow can be characterized at any arbitrary point within the domain. Modelling in such great detail obviously requires significant computational effort, and as a result this method is only employed in relatively small grids. Therefore, modelling a complete packed bed reactor is not realistic given the average computational resources available. To still conduct some sort of numerical research, use can be made of a Representative Elementary Volume (REV). This geometry comprises a part of the reactor that is small enough to keep the number of mesh cells within a realistic limit, but large enough to capture the spatial detail of the physical quantities of interest.

2.3.2 Continuum method

For large and complex geometries, solving the conservation equations at the smallest length scales will require extremely long computational times. Therefore, using a continuum approach can be advantageous in these scenarios. By using this approach all physical properties of the domain are averaged and spatial details on micro-scale are ignored.

When a fluid flows along an object, a viscous boundary layer is formed. Kinetic energy is dissipated in heat due to the viscosity of the fluid. This results in a decrease in pressure in the streamwise direction. For flow through porous media, Henry Darcy derived an equation to relate the pressure drop over the medium to the Darcy velocity (the reactor axis and flow direction lies along the x-axis):

$$\frac{\Delta p}{L} = \frac{\mu}{K} u_s, \tag{2.35}$$

where $\frac{\Delta p}{L}$ [Pa/m] is the difference in pressure over length L, μ [Pa·s] is the fluid dynamic viscosity, K [m^2] is the permeability and u_s [m/s] is the superficial or Darcy velocity. The permeability quantifies the easiness a fluid can pass through a porous material. It can be determined by empirical correlations which are a function of the porosity and particle diameter. An example of this is the Blake-Kozeny equation [51]

$$K = \frac{d_s^2}{B_K} \left(\frac{\epsilon^3}{(1-\epsilon)^2} \right), \tag{2.36}$$

in which B_K is the Blake-Kozeny constant. For spherical particles and porous media with $0.26 < \epsilon < 0.48$, the constant has a value of 172.8, as proposed by Carman [52]. For low flow velocities, predictions made using equation 2.35 are a sufficient approximation. However, as flow velocities increase, inertial effects play a more and more dominant role. This can be accounted for by adding the Forchheimer term to form the Forchheimer equation. This term takes into account the inertia by the quadratic dependence on the flow velocity:

$$\frac{\Delta p}{L} = \frac{\mu}{K} u_s + C \rho_f u_s^2, \tag{2.37}$$

where the constant C is calculated by

$$C = \beta \frac{1-\epsilon}{\epsilon^3 d_p} \tag{2.38}$$

Ergun [53] proposed a value of 1.75 for constant β. In his influential work he rewrote the Forchheimer equation to the Ergun equation, now widely used:

$$\frac{\Delta p}{L} = \alpha \frac{(1-\epsilon)^2}{\epsilon^3} \frac{\mu}{d_p^2} u_s + \beta \frac{1-\epsilon}{\epsilon^3} \frac{\rho_f}{d_p} u_s^2, \tag{2.39}$$

where ϵ [-] is the packed bed porosity, μ [Pa·s] is the dynamic viscosity, d_p [m] is the diameter of the particles, ρ_f [kg/m^3] is the fluid density and u_s [m/s] is the superficial flow velocity. From experiments Ergun established that the value of α is 150 and this holds up to a certain extent, although some sources propose different definitions, both through experimental [54] and numerical [48] research. Although extensively used, the Ergun equation was established for higher Reynolds numbers as well and for that reason does not always provide satisfactory results that concord with values obtained from experiments for lower Reynolds numbers. Therefore, several other relations have been proposed. Josef Kozeny [55] and Philip Carman [56] for example derived an equation to calculate the permeability of materials. It can also be used to calculate the pressure drop over a porous medium:

$$\frac{\Delta p}{L} = \frac{u_s \mu}{K}, \tag{2.40}$$

in which u_s [m/s] is the superficial velocity, μ is the [m^2/s] is the dynamic viscosity and K [m^2] is the permeability of the material. It is only valid for laminar flows. The KTA presented a method (known as the KTA method) to model pressure losses over packed beds at high Reynolds numbers [57]

$$\frac{\Delta p}{L} = \frac{3}{Re^{0.1}} \frac{(1-\epsilon)^{1.1}}{\epsilon^3} \frac{\rho_f}{d_p} u_s^2 + \frac{160}{Re} \frac{(1-\epsilon)^2}{\epsilon^3} \frac{\rho_f}{d_p} u_s^2 \tag{2.41}$$

Over the years, the research in pressure drop has been abundant. Das [48] conducted numerical research, using DNS to simulate flow through a column of randomly packed spheres. To this end they used the Immersed Boundary Method (IBM) to model the particle configuration, which allowed them to avoid using complex mesh structures and particle-particle contact methods. Applying velocities in the lower laminar regime ($Re < 1000$), it was concluded that pressure drop values could be obtained within the 25% error margin to the modified Ergun equation from [54]. In the work of Ahmadi and Sefidvash [58] the Ergun and KTA equations were evaluated against a CFD model of a packed bed. In their SolidWorks model, they found that both the Ergun and KTA approaches overestimated the pressure drop over the packed bed. Consequently, they proposed to fit a function of the form

$$\frac{\Delta p}{L} = \frac{a}{Re_p^b} \frac{(1-\epsilon)^n}{\epsilon^3} \frac{\rho}{d_p} u_s^2, \tag{2.42}$$

in which a, b and c are constants that are to be determined by fitting over results. Also, a porosity-dependent particle Reynolds number is used: $Re_p = Re/(1-\epsilon)$. It must however be noted that their range of Reynolds numbers was extensive (0-150000) and therefore it was justified to neglect the viscous effects on the pressure drop.

The porosity can be held constant over the reactor volume, but in practice this is not the case. Wall effects cause it to be higher than at the reactor center. Giese [59] provided an approximation for the reactor porosity as a function of the radial coordinate r:

$$\epsilon(r) = \epsilon_c \left(1 + 1.36 \exp\left[-5\frac{R-r}{d_p}\right]\right), \tag{2.43}$$

where ϵ_c [-] is the porosity at the center of the reactor and R [m] is the reactor radius. With the continuum approach, the water mass balance can be expressed as being only spatially dependent on the axial coordinate x (the direction of the flow) [60]

$$\frac{\partial c}{\partial t} + u\frac{\partial c}{\partial x} - D_x \frac{\partial^2 c}{\partial x^2} + \frac{1-\epsilon}{\epsilon} \rho_p \frac{d\bar{q}}{dt} = 0, \tag{2.44}$$

with ρ_p [kg/m^3] the particle density and D_x the axial dispersion coefficient. q is a variable similar to α, as it is a ratio of water taken up to the maximal water uptake. The energy equation is defined as [60]

$$\overline{\rho_s C_{p,s}} \frac{\partial T}{\partial t} + \epsilon \rho_f C_{p,f} u \frac{\partial T}{\partial x} - k_{eff} \frac{\partial^2 T}{\partial x^2} - (1-\epsilon)\rho_s \frac{dq}{dt} \Delta H + \frac{4h_i}{d_i}(T - T_w) = 0 \tag{2.45}$$

where $\overline{\rho_s C_{p,s}}$ [J/K] is the overall volumetric heat capacity of the particle bed, ρ_f [kg/m^3] and $C_{p,f}$ [J/K] are respectively the density and volumetric heat capacity of the fluid, k_{eff} [W/mK] is the effective thermal conductivity, h_i [W/m^{2}K] is the convective heat transfer coefficient and T_w [K] is the reactor wall temperature.

In this thesis DNS is used, so that the flow around the particles can be modelled. In doing so, a comparison can be drawn with continuum predictions. Additionally, the model is expected to be able to show effects on micro-scale.

2.4 Reaction models

Several different models are available that describe the course of the hydration/dehydration reactions. Often, the fractional conversion $\alpha = \frac{m_0 - m_t}{m_0 - m_\infty}$ is used to describe the extend of conversion. In this definition m_0 is the initial weight, m_t is the weight at the time t and m_∞ is the final weight of the sample [6]. It is defined as the mass that is already reacted over of the total mass. Its time derivative $\frac{d\alpha}{dt}$ is the parameter of interest in chemical reactions. There are several ways in modelling the conversion rate and this section will provide the three most prevalent ones.

2.4.1 Arrhenius method

The most frequently used and most simplified approach is using a composite equation consisting of three terms relating to the ambient conditions and state of the material. The temperature dependence is captured in the Arrhenius term:

$$k(T) = A_f \exp\left(\frac{-E_a}{RT}\right), \tag{2.46}$$

where R [J/molK] is the gas constant, A_f is the pre-exponential term A_f [1/min] and E_a is the activation energy E_a [J/mol]. The shape function $f(\alpha)$ can take several forms, which are listed in table 2.1. When modelling a specific reaction, the appropriate function has to be selected. For spherical particles with a shrinking core reaction interface (the outer layer of the particle reacts instantaneously and the interface then moves towards the center), R_3 from table 2.1 can be used for example.

While pressure dependency has been a topic of debate [21], it is included in this work. The reaction kinetics are affected by the ratio of the equilibrium pressure p_{eq} [Pa] to the water vapour pressure p_{wv} [Pa]:

$$h(p) = 1 - \frac{p_{eq}}{p_{wv}} \tag{2.47}$$

When p_{wv} equals p_{eq} this term will be zero and no reaction will take place. The equilibrium pressure is dependent on the reaction enthalpy and the temperature and can be determined by deriving from the Clausius-Clapeyron relation:

$$\frac{dln(p_{eq})}{d\frac{1}{T}} = \frac{\Delta H}{R} \tag{2.48}$$

$$p_{eq} = 4.228 \cdot 10^{10} \exp\left(-\frac{7337}{T}\right), \tag{2.49}$$

with the reaction enthalpy ΔH [J/mol] and the universal gas constant R [J/molK]. Equation 2.49 was obtained by fitting over equilibrium lines for K_2CO_3 [61]. It must be noted that T is in [K]

Table 2.1: Different reaction models in differential and integral form

Model	Differential form $f(\alpha)$	Integral form $g(\alpha)$
Nucleation models		
Power law (P_2)	$2\alpha^{1/2}$	$\alpha^{1/2}$
Power law (P_3)	$3\alpha^{1/2}$	$\alpha^{1/3}$
Power law (P_4)	$4\alpha^{1/2}$	$\alpha^{1/4}$
Avrami-Erofeyev (A_2)	$2(1-\alpha)[-ln(1-\alpha)]^{1/2}$	$[-ln(1-\alpha)]^{1/2}$
Avrami-Erofeyev (A_3)	$3(1-\alpha)[-ln(1-\alpha)]^{2/3}$	$[-ln(1-\alpha)]^{1/3}$
Avrami-Erofeyev (A_4)	$4(1-\alpha)[-ln(1-\alpha)]^{3/4}$	$[-ln(1-\alpha)]^{1/4}$
Prout-Tomkins	$\alpha(1-\alpha)$	$ln[\alpha/(1-\alpha)]+c^a$
Geometrical contraction models		
Contracting area (R_2)	$2(1-\alpha)^{1/2}$	$1-(1-\alpha)^{1/2}$
Contracting volume (R_3)	$3(1-\alpha)^{2/3}$	$1-(1-\alpha)^{1/3}$
Diffusion models		
1-D diffusion (D_1)	$1/(2\alpha)$	α^2
2-D diffusion (D_2)	$-[1/ln(1-\alpha)]$	$((1-\alpha)ln(1-\alpha)+\alpha)$
3-D diffusion (D_3)	$[3(1-\alpha)^{2/3}]/[2(1-(1-\alpha)^{1/3})]$	$(1-(1-\alpha)^{1/3})^2$
Ginstling-Brounshtein (D_4)	$3/[2((1-\alpha)^{-1/3}-1)]$	$1-(2/3)\alpha-(1-\alpha)^{2/3}$
Reaction-order models		
Zero-order (F_0/R_1)	1	α
First-order (F_1)	$(1-\alpha)$	$\ln(1-\alpha)$
Second-order (F_2)	$(1-\alpha)^2$	$[1/(1-\alpha)]-1$
Third-order (F_3)	$(1-\alpha)^3$	$(1/2)[(1-\alpha)^{-2}-1]$

and this will yield the vapour pressure in [mbar]. The water vapour or partial pressure is derived from the ideal gas law:

$$c = \frac{n}{V} \qquad\qquad pV = nRT \tag{2.50}$$

$$p_{wv} = cRT, \tag{2.51}$$

in which c is the molar concentration [mol/m^3], n is the number of moles, V is the volume [m^3]. Composing terms 2.46, 2.47 and the chosen shape function R_3 results in the following equation:

$$\frac{d\alpha}{dt} = k(T)f(\alpha)h(p) = A_f \exp\left(\frac{-E_a}{RT}\right)3(1-\alpha)^{2/3}\left(1-\frac{p_{eq}}{p_{wv}}\right) \tag{2.52}$$

This equation describes the rate with which the sample reacts as a function of particle temperature, water vapour pressure and fractional conversion. Because both the Arrhenius term and the pressure term are a function of temperature, it may be interesting to visualize their temperature dependence in figure 2.4.

Arrhenius' law in general dictates that reaction rates increase at higher temperatures, while the pressure term causes a decrease due to the higher equilibrium pressure. Because of its simplicity and stability, the Arrhenius model type has been extensively used in hydration and dehydration studies.

2.4.2 Nucleation and growth model

An alternative approach in determining the conversion rate is using the nucleation and growth model. This model does not depend solely on experimental data, but utilizes the combined effects

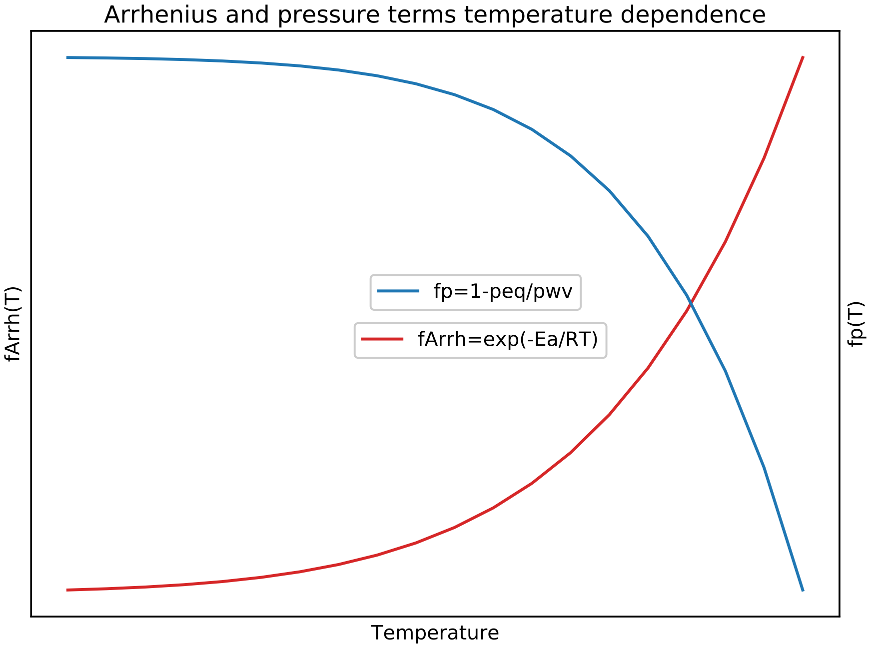

Figure 2.4: According to Arrhenius' law, based on the work of van 't Hoff, reaction rates increase under higher temperatures. Simultaneously, as the equilibrium pressure increases, the pressure term has a negative effect on the reaction rate.

of nucleation and growth. It was first proposed by Mampel, as early as 1940 [62]. Nucleation and growth can easily be observed in crystalline salt hydration experiments, as for example in figure 2.5.

Nucleation occurs when a new nucleus of reacted material is formed and takes place at the particle surface at locations of high reactivity. The nucleation rate is governed by the areic frequency γ. After a nucleus is formed, **growth** determines how quickly the radius of the nucleus grows in the salt particle over time and is quantified by the areic reactivity ϕ. The parameters that have influence on the reaction rate can be grouped in thermodynamic conditions and conditions that refer to the current state of the particle. The reaction rate can then be characterized with [13]

$$\frac{\partial \alpha}{\partial t} = \phi(T, p_{wvp}, ...)S_m(t, \phi, \gamma, r_0) \tag{2.53}$$

The first term is a function of the temperature and partial pressure, while the second term is a function of time, areic reactivity, areic frequency and the reaction interface in the particle. In most circumstances, either nucleation or growth occurs at a much faster rate than the other. As a result, it may for instance be the case that the grain surface is nucleated in a few early timesteps. This causes the reaction to be governed (rate limited) by growth. In a spherical particle, reaction kinetics are displayed similar to the shrinking core model (R_3 in Table 2.1). The ratio between nucleation and growth can be expressed by the number K, which is defined as

$$K = \frac{S_0 r_0 \gamma}{\phi}, \tag{2.54}$$

where S_0 is the grain surface area and r_0 is the radius of the grain sphere. An algorithm covers the bulk of the calculation. However, nucleation rates and growth rates are still dependent on data obtained from experiments. Instead of through numerical iteration, nucleation and growth can also be solved analytically in some circumstances, as was shown in [6, 13].

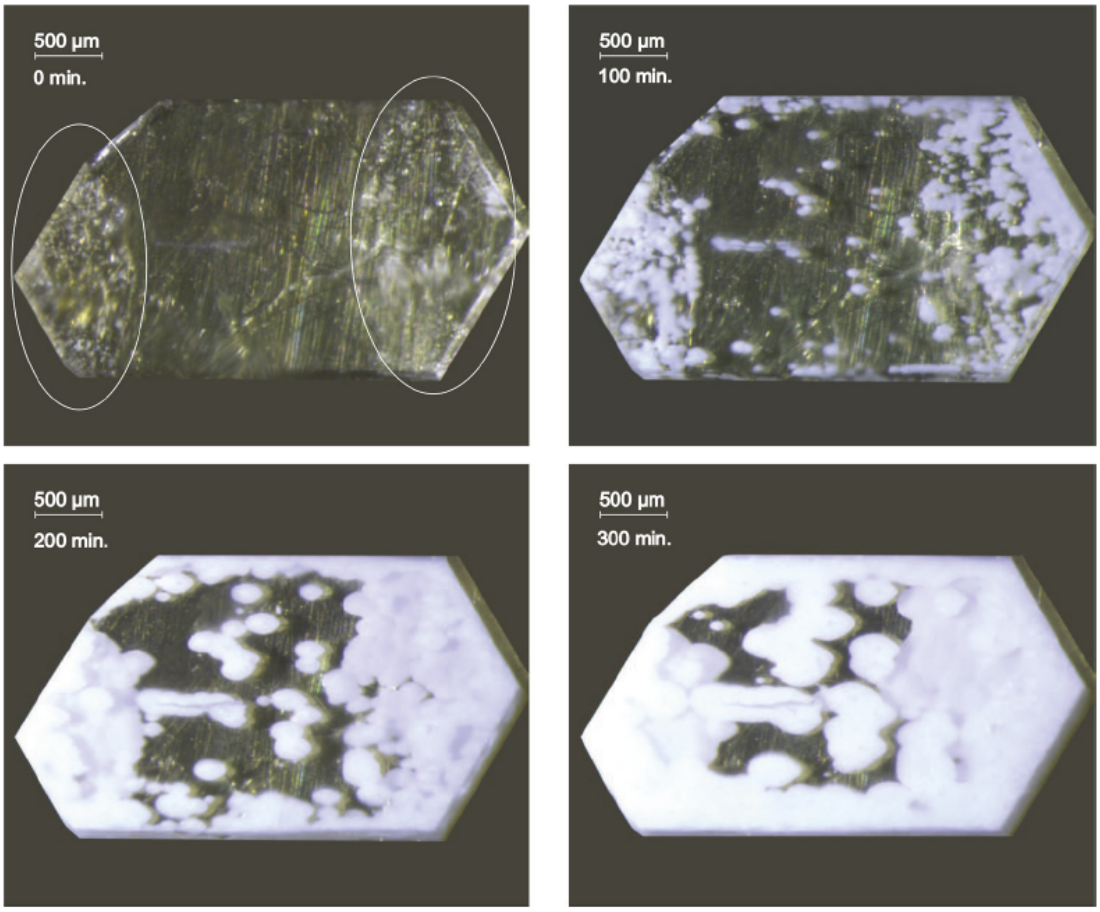

Figure 2.5: Images of dehydration of a single $Li_2SO_4 \cdot H_2O$ crystal. The nuclei can be seen as the white dots that are very small in the top left image, grow in the top right and bottom left image and at last cover almost the entire surface of the salt grain. The nucleation rate can be determined by counting the number of newly formed nuclei in one time interval, while the growth rate is determined by measuring the increase in nucleus radii over time [6].

The nucleation and growth model has in several cases proven to yield results comparable to experiments. In [6] and [19] the fractional conversion curves showed similarities in shape. The main issue was the slight time delay, which was probably caused by an underestimation of the nucleation rate. A disadvantage of nucleation and growth is that the nucleation rate and growth rate are difficult to determine.

2.4.3 Linear Driving Force model

The Linear Driving Force (LDF) model is a third alternative to the modelling of (de)hydration, but can be used for all chemical reactions in general. It was introduced by Gleuckauf and Coates in 1947 [63]. The reaction kinetics are governed by

$$\frac{dq}{dt} = k_{LDF}(q_{eq} - q) \tag{2.55}$$

This equation basically determines the rate of water uptake by the solid from the difference in current mass q and equilibrium mass q_{eq}, multiplied by a factor k_{LDF} [1/s]. k_{LDF} is a lumped parameter related to the particle diameter d_p [m], the mass transfer coefficient k_f [kg/s], the porosity ϵ and the macropore Knudsen diffusivity δ_p [m^2/s] [64]:

$$k_{LDF} = \left(\frac{d_p}{6k_f} + \frac{d_p^2}{60\epsilon\delta_p} \right)^{-1} \tag{2.56}$$

Advantageous to the model is that it is robust, analytic and physically consistent. Research by Gaeini [12] proved that the LDF model provides results similar to experimental data (in this research, the hydration of zeolite 13X was investigated).

Comparing the three methods mentioned in this section, nucleation and growth stands out due to the computational effort it requires. Although it can be utilized for particles of any shape and may yield results of higher accuracy, time limitations force the use of either the Arrhenius method or the LDF method. Additionally, crucial parameters like the nucleation rate and the growth rate, which are temperature and pressure dependent, are difficult to determine. Relatively little research has been carried out on the LDF method, and because the first method is a very well-known approach, it is chosen to use Arrhenius method to model the hydration reaction in this thesis.

Chapter 3

Numerical study: hydration of an REV

The hydration/dehydration reaction progress is one of the most important characteristics of a heat battery. A faster reaction will generate a higher thermal output, but these higher temperatures in general also cause higher thermal losses. Varying inlet conditions will also affect the reactor performance: hydrating at a lower inlet temperature for example increases the reaction rate, which can also be accomplished by using a higher inlet concentration. In this thesis the aim is to develop a model to simulate the hydration of a Representative Elementary Volume (REV) of a K_2CO_3 packed bed, so that these effects can be closely investigated. This model is developed using the software OpenFOAM. In this chapter the numerical model is described. First, a description of the geometry is given. Then, the different possible meshing approaches are discussed. Subsequently, the solution strategy including the equations that are solved are explained. Finally, after the model parameters and the boundary conditions are given, the results are presented and discussed.

3.1 Geometry

Modelling a complete packed bed reactor is a virtually impossible task when using DNS. The fine structures arising from the relatively small salt particles combined with the relatively large overall size of a reactor will result in a model which is computationally very expensive to solve for conventional computers. To accommodate for the computational limitations, use is made of an REV. An REV is generally composed of one or more unit cells. A unit cell is the smallest volume that can be used in the model without changing the geometric properties. Figure 3.1 illustrates the relative size scales of the reactor and the unit cell. In the unit cell, a number of packed particles is regarded as representative for the complete reactor. In this thesis, a unit cell with face-centered cubic (FCC) configuration is chosen as the base geometry as was also proposed by Lan [15]. This unit cell is then repeated three times to form the REV. By repeating the unit cell twice in the streamwise direction, the model will be able to provide more insight in the development of the flow, temperature and concentration. For the FCC unit cell, 14 particles with a 1mm diameter are positioned as shown in figure 3.2. To improve mesh quality, the particle-particle contact points have to be treated, as was discussed in section 2.1.2. It is chosen to shrink the particles to create gaps. As was mentioned before, sources use a shrinkage of 1 or 2%, which increases the mesh quality sufficiently while leaving the local flow patterns more or less intact. However, since the number of particles is moderately large and calculations are computationally very expensive, it is chosen to shrink the particles by 3%. This increases mesh quality drastically, reducing computational efforts. However, it must be noted that the velocities near the contact points are significantly larger, as was shown in [26]. A more detailed overview of the effects of the other possibilities to model the particles (increasing the particles in size, creating inter-particle bridges and capping the particles) is given in sections 4.4.1 and 4.4.2.

The volumes of the particles are subtracted from the unit cell cube so that the negative volume is left which comprises the flow domain. The REV has a porosity of 0.324. The final geometry is shown in figure 3.3.

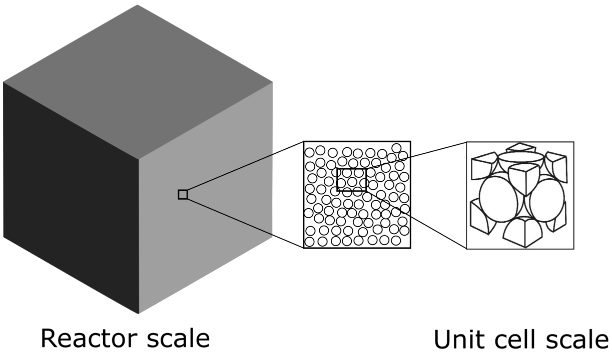

Figure 3.1: Scale size comparison of the reactor and the unit cell. The unit cell is the smallest volume that can still capture sufficient spatial detail.

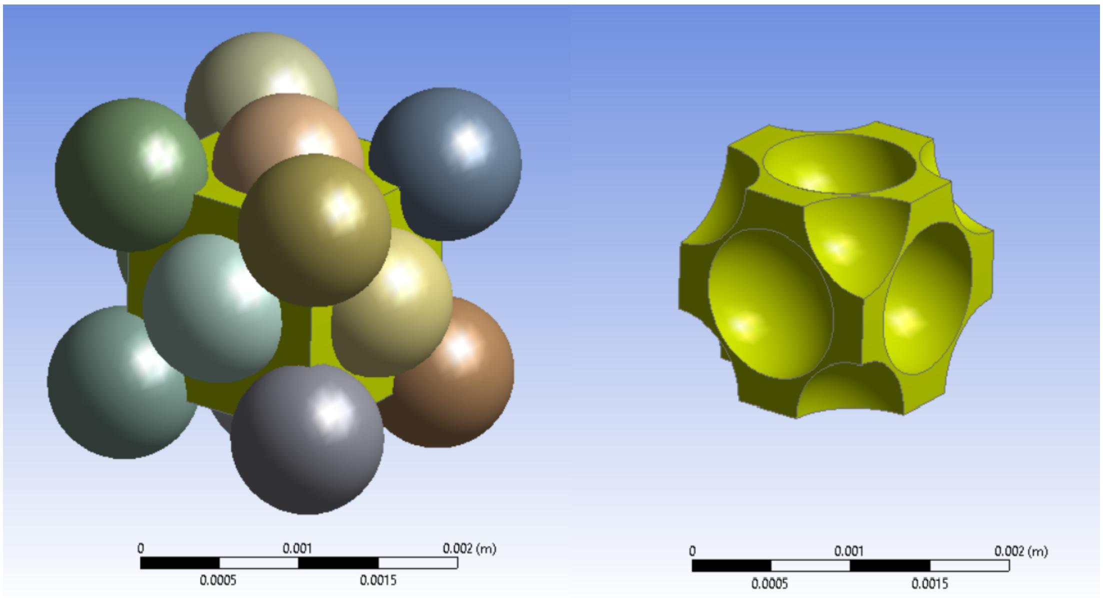

Figure 3.2: The FCC unit cell that is used as base geometry. On the left the 14 particles are shown and the unit cell cube in yellow. On the right the particle volumes are subtracted from the unit cell cube, with the base geometry remaining.

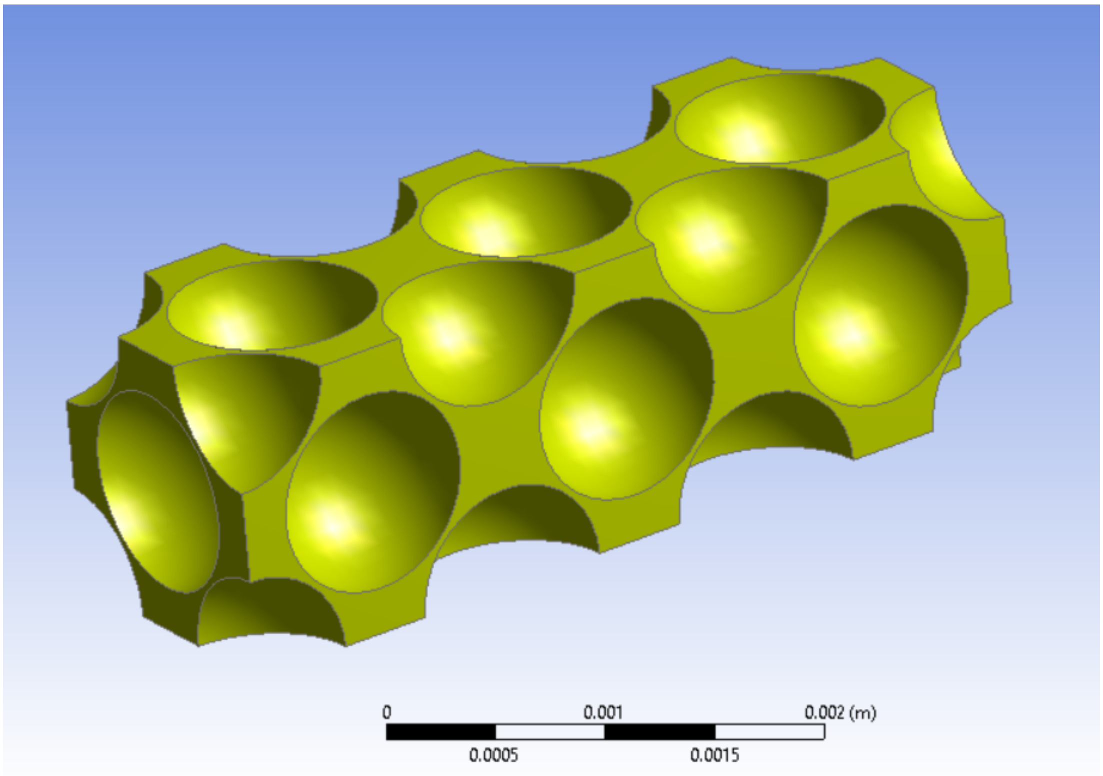

Figure 3.3: Copying the unit cell twice results in a geometry with 32 particles: 2 complete (not visible), 14 half, 8 quarter and 8 1/8 particles.

3.2 Meshing

Geometries in CFD problems are discretized by meshing. The geometry is divided into smaller volumes. In the 3D case, often tetra- and hexahedrals are used for this. Meshing is a necessary operation because the interpolation methods of the element shapes are known, while this is not the case for the complex shapes of the complete geometry. The computational volume is subdivided into elements, while the elements are connected through nodes at their vertices. Mesh grids can be differentiated on 1) being structured or unstructured and 2) being body-fitted or not. The four most common types are illustrated in figure 3.4.

(a) Structured body-fitted mesh. The elements consist of regular shapes and sizes, and nodes spacing is governed by simple algorithms. This type is recommended for simple geometries, due to better convergence and higher resolution.

(b) Unstructured body-fitted mesh. In practice, most geometries are too complex to be discretized with structured grids. If that is the case, unstructured meshes are used. Nodes are placed throughout the domain as is deemed most suitable by the chosen algorithm (e.g. Netgen, GHS3D). This is not as space-efficient as a structured grid, but it allows for the meshing of virtually any geometry.

(c) Hybrid body-fitted mesh. This method employs a combination of structured and unstructured grids. Unstructured meshes are used near complex geometry features such as small edges and curves, while the mesh can be structured in larger sub-volumes with regular boundaries.

(d) Structured mesh with embedded boundary, or Immersed Boundary Method (IBM). This advanced type does not use a body-fitted mesh. Instead, the structured grid cells may be protruding into the solid body, or may even cover the body domain entirely. The body boundary is embedded in the structured grid. This requires additional computations to account for the interaction of the elements with the embedded boundary. However, a simple structured grid is sufficient, which may reduce computational effort. The OpenFOAM extension Foam-extend 4.0 includes this feature.

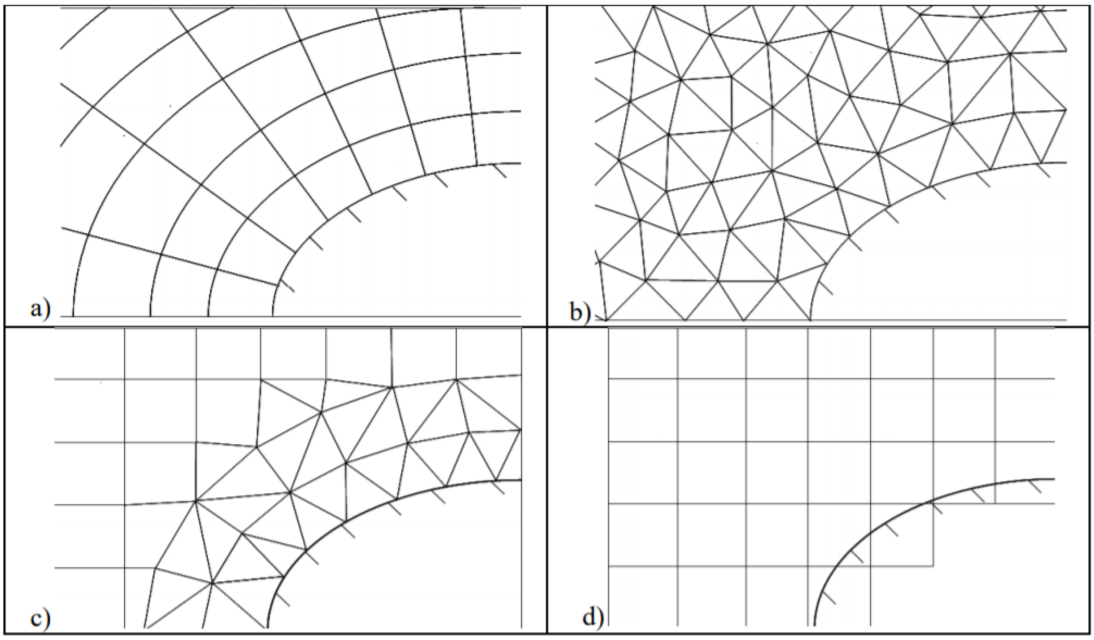

Figure 3.4: Four types of meshes. a) structured; b) unstructured; c) hybrid structured/unstructured; d) immersed boundary [7].

In this thesis, the unstructured mesh is used, due to its ease of implementation and flexibility. In order to capture boundary effects, a mesh inflation of two layers is used at the particle surfaces, which is shown in figure 3.5 below. The inflation layer thickness has to be large enough to capture the boundary layer effects, but too thick inflation layers will not allow for intermediate cells with proper quality (especially the skewness will be high, as shown in figures 3.6a and 3.6b).

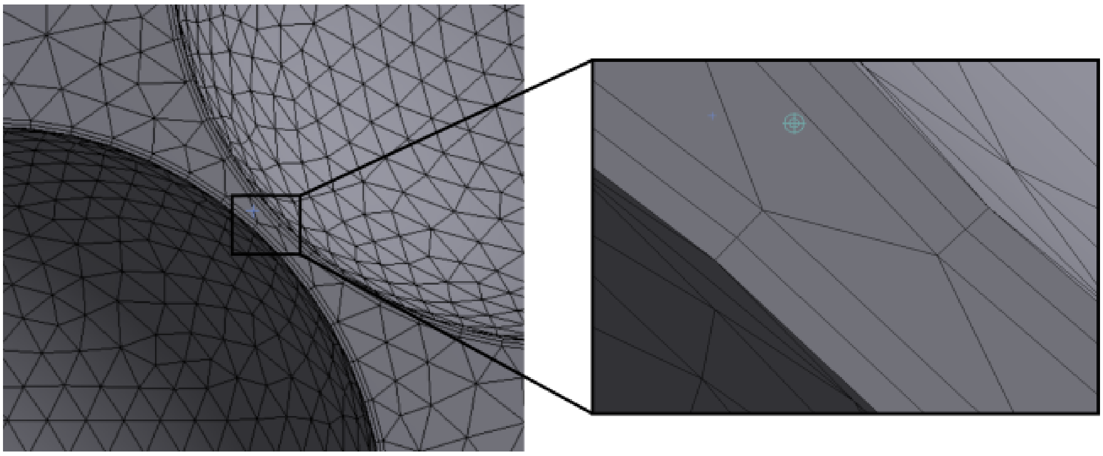

Figure 3.5: The would-be contact points between particles. Due to the 3% shrinkage a gap is created, leaving space for the inflation layers and regular cells.

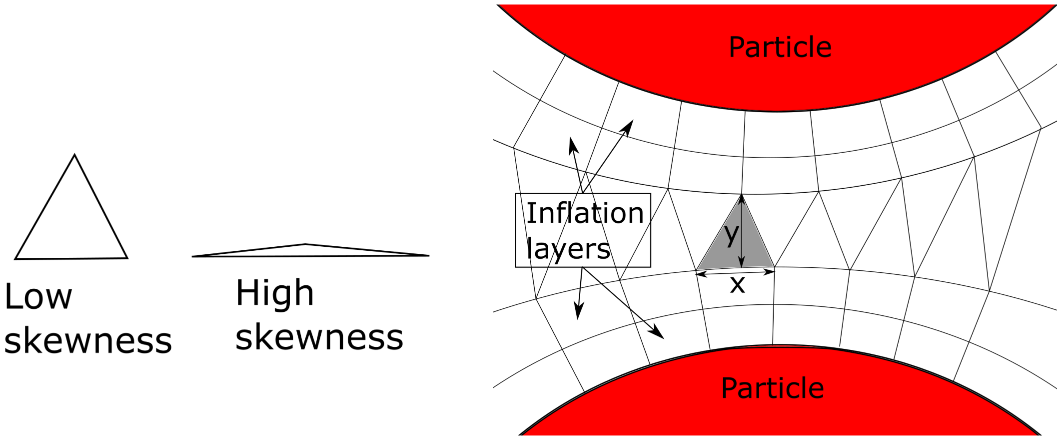

(a) A low skewed cell vs a highly skewed cell.

(b) Inflation layers between particles take up extra space that may result in skewed cells.

Figure 3.6: Possibly skewed cells between inflation layers. Reducing skewness can be done by either decreasing the element size of the body-fitted mesh on the particles (decreasing x) or using smaller inflation layers (effectively increasing y).

The accuracy of the model solution is depends heavily on the quality of the mesh. In general, refining the mesh yields a solution with higher accuracy. However, bearing in mind that time and computational resources are limited, the modeller has to establish a solution that is regarded as sufficiently accurate. This is further explained in Appendix B.1, where the spatial convergence study is described. A larger REV is used here (41 particles instead of 32), although this should not be of influence.

3.3 Solvers

OpenFOAM offers a wide range of numerical solvers. For modelling the hydration of salt particles, there are several options.

- **icoFoam**: Although the pre-built OpenFOAM solvers are numerous, many CFD problems require the CFD engineer to write their own, specific solver. The easiest approach in doing this is copying a simple solver and adapting it as is required. Because icoFoam is the simplest of the OpenFOAM solvers, it is a popular choice. In its unadapted form, icoFoam can be used for modelling incompressible, laminar, isothermal flow. It only requires initial conditions and boundary conditions. The flow field is solved using the Pressure-Implicit with Splitting of Operators or PISO algorithm. Due to its simplicity, computations are very fast. However, it is a time-dependent solver, requiring extra computations.

- **simpleFoam**: In many aspects simpleFoam is comparable to icoFoam. The key differences are that simpleFoam is a steady-state solver using the Semi-Implicit Method for Pressure Linked Equations, or SIMPLE algorithm, and that it is also applicable for turbulent cases. In OpenFOAM, the number of pressure correction iterations of the SIMPLE loop can be set by the user. In figure 3.7, a schematic of the algorithm is shown.

- **chtMultiRegionFoam**: chtMultiRegionFoam is the one of the solvers that can be used for multiregion problems. It uses the concept of Conjugate Heat Transfer: all domains are solved separately and on the interfaces the temperature solutions of one region are used for the other. For fluid regions, the SIMPLE algorithm is used, while the solid regions are solved with Fourier's law (equation 2.28). Due to the fact that chtMultiRegionFoam is a compressible solver, a relatively large amount of computational effort is required.

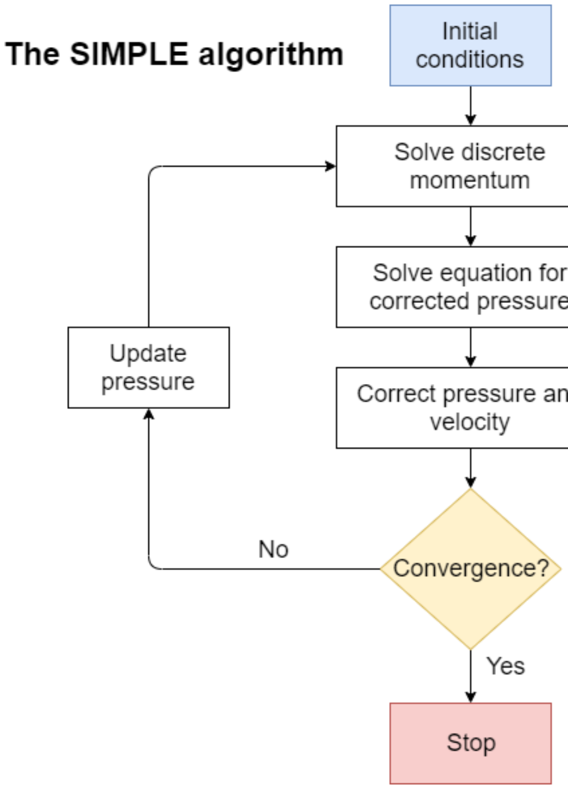

Figure 3.7: The SIMPLE algorithm. In OpenFOAM, the number of iterations of the pressure corrector loop can be set by the user.

3.4 Solution strategy

Simulating every physical process in the salt reactor requires a tremendous amount of time and computational effort, while it may not improve the model accuracy significantly. Therefore for this thesis, a number of assumptions are made:

1. Grains are spherical and do not increase in size due to water absorption.
2. As the Biot number is in the order of 0.1, the grain temperature is assumed to be uniform. See Appendix C for the verification of this assumption.
3. Both transport of temperature and water concentration are decoupled i.e. do not affect the fluid flow.

Under the last assumption the final solution can be obtained in two separate steps. The flow field is solved first and this solution is then exported to the second study, where the temperature and concentration fields are solved. This reduces computational effort, because the flow field is not solved for each time step, but only once.

3.4.1 Solving the flow field

In this work, the simulation domain is carved up and solved with different solvers. Under assumptions stated earlier in this chapter, the flow is regarded as quasi-steady. This allows for the flow field to be solved separately. The geometry and boundary conditions are schematically shown in figure 3.8. Because of the steady-state and incompressible nature of the flow, the choice is made to use the simpleFoam solver, mentioned in section 3.3. It solves for equations 2.32 and 2.33:

$$\nabla \cdot \boldsymbol{u} = 0 \tag{2.32}$$

$$\boldsymbol{u} \cdot \nabla \boldsymbol{u} = \nu \nabla^2 \boldsymbol{u} - \frac{1}{\rho_f} \nabla p \tag{2.33}$$

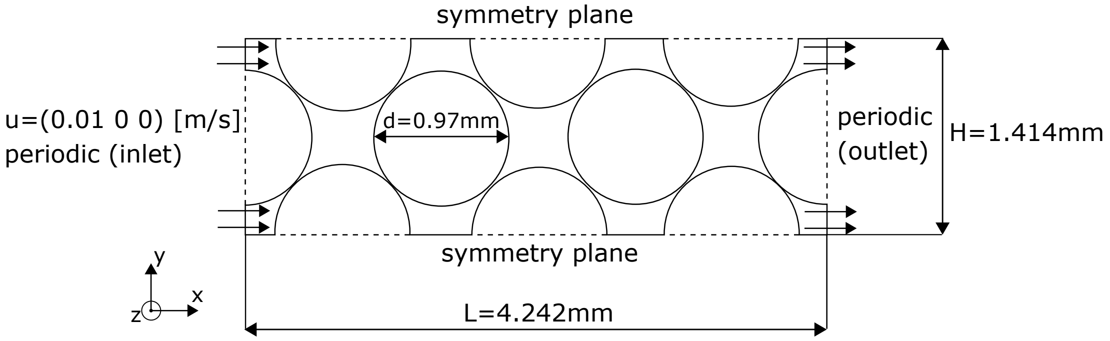

Figure 3.8: Calculation domain for the flow field, consisting of 32 particles in an FCC lattice. A periodic boundary condition of 0.01 [m/s] is prescribed at the inlet and outlet, so that a fully developed flow field is obtained. Symmetry conditions are applied to the side boundaries, and no-slip boundary conditions are applied to the particle surfaces.

For the velocity, a cyclic boundary condition is applied to the inlet and outlet. On the side boundaries (in the y- and z-plane) of the REV, symmetry conditions are prescribed. Dirichlet boundary conditions are used on the particle surfaces that enforce the no-slip conditions (velocity at the interface is zero). Input parameters for this study can be found below in table 3.1.

Table 3.1: Parameters used in the study to solve the flow field.

Symbol	Description	Value
u_i	Interstitial velocity vector	(0.01 0 0) [m/s]
ν	Kinematic viscosity dry air	1.74e-5 [m^2/s]
d_p	Particle diameter	0.97 [mm]
L	REV length	4.242 [mm]
H	REV height (and width)	1.414 [mm]

3.4.2 Solving temperature and concentration

After the velocity solution is obtained it is exported to be used in the next study, where the temperature and concentration fields are solved. The geometry and boundary conditions are schematically shown in figure 3.9. In this part of the study, a modified version of the icoFoam solver (see section 3.3) is employed (simpleFoam cannot be used due to the transient nature of this computation). The PISO algorithm is removed and scalar transport equations for temperature T (2.20) and concentration c (2.29) are added:

$$\frac{\partial T}{\partial t} + \boldsymbol{u} \cdot \nabla T = D_T \nabla^2 T \tag{2.20}$$

$$\frac{\partial c}{\partial t} + \boldsymbol{u} \cdot \nabla c = D_c \nabla^2 c \tag{2.29}$$

To determine the fractional conversion rate, equation 2.52 is used:

$$\frac{d\alpha}{dt} = A_f \exp\left(\frac{-E_a}{RT_p}\right)(1-\alpha)^{2/3}\left(1 - \frac{p_{eq}}{p_{wv}}\right) \tag{2.52}$$

The factor 3 in front of the shape term is now included in the pre-exponential factor A_f. It must also be noted that A_f is given in [1/min], this must be scaled to [1/s] in the calculations. In equation 2.52, the equilibrium pressure (in [mbar]) and water vapour pressure are calculated using equations 2.49 and 2.51:

$$p_{eq} = 4.228 \cdot 10^{10} \exp\left(-\frac{7337}{T}\right) \tag{2.49}$$

$$p_{wv} = cRT \tag{2.51}$$

Using the fractional conversion rate, the energy balance (equation 2.26) and water mass balance (equation 2.31) of the particles can be calculated:

$$\frac{\partial T_p}{\partial t} = -\frac{k_f A}{\rho_s c_{p,s} V}\overline{\frac{\partial T}{\partial n}} + \frac{\Delta H}{M_s c_{p,s}}\frac{d\alpha}{dt} \tag{2.26}$$

$$\overline{\frac{\partial c}{\partial n}} = -\frac{\rho_s V}{M_s D_c A}\frac{d\alpha}{dt} \tag{2.31}$$

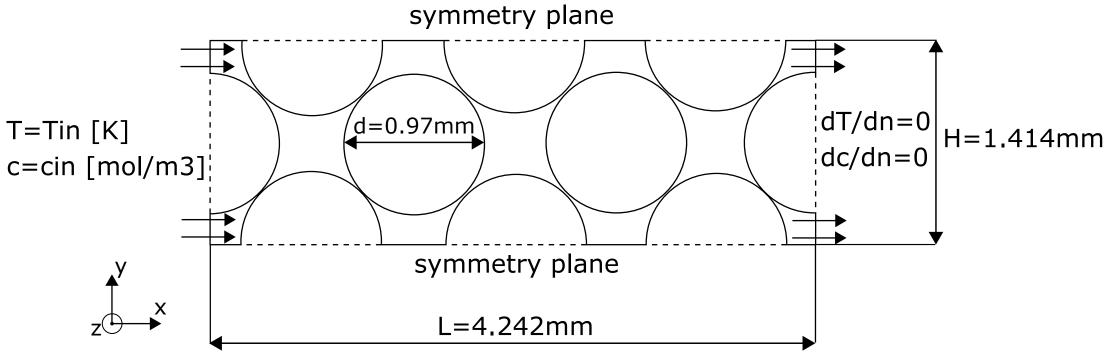

Figure 3.9: Calculation domain for the temperature and concentration fields. An inlet temperature and concentration are prescribed at the inlet. Symmetry conditions are again set at the REV side boundaries. At the outlet, zero-gradient conditions are applied for both scalar fields. At the particle surfaces, a dynamic Dirichlet boundary conditions for the temperature is set. A dynamic Neumann boundary condition is applied for the concentration.

An inlet temperature and concentration are prescribed at the inlet. Again, symmetry conditions are set at the REV side boundaries. At the outlet, zero-gradient Neumann conditions are applied for both scalar fields, because their values are not known a priori and are assumed to not change significantly at the outlet in the direction of the flow. At the particle surfaces, a dynamic (changing each time step) Dirichlet boundary condition is applied for the temperature. A dynamic Neumann boundary condition is applied for the concentration.

Per time-step i the model takes the following steps:

1. Using $\frac{d\alpha}{dt}^{i-1}$ and $\overline{\frac{\partial T}{\partial n}}^{i-1}$ equation 2.26 is solved to determine particle temperature T_p^i. The temperature field is solved using equation 2.20 and the new temperatures of the particles as Dirichlet boundary conditions.

2. Using $\frac{d\alpha}{dt}^{i-1}$ equation 2.31 is solved to obtain $\overline{\frac{\partial c}{\partial n}}^{i}$. The concentration field is solved using equation 2.29 and the normal gradients as Neumann boundary conditions.

3. Requesting particle temperature T_p^i and concentration c^i at the particle boundary, $\frac{d\alpha}{dt}^{i}$ is calculated using equation 2.52. Additionally, the new value of α is determined. $\overline{\frac{\partial T}{\partial n}}^{i}$, $\frac{d\alpha}{dt}^{i}$ and α^i are exported to the next time step (return to step 1).

The solution strategy is illustrated schematically below in figure 3.10.

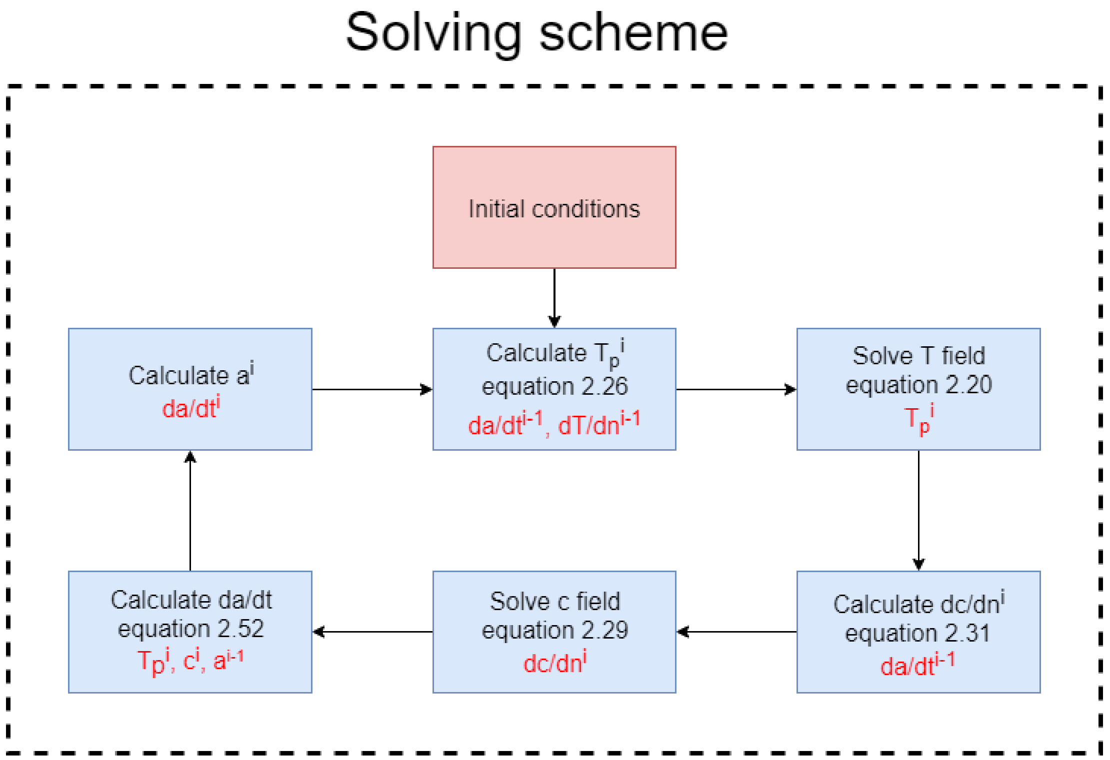

Figure 3.10: Solver scheme for the hydration model. The cycle is repeated each time step. Values required in the equations are written in red text.

3.4.3 Inlet conditions and parameters

The inlet conditions and parameters that are used in this study are listed in table 3.3. The inlet temperature and concentration are set at 26°C and 0.603 [mol/m^3] (= 14.99 [mbar] partial pressure) of water vapour. The inlet concentration is slightly over the deliquescence line at this temperature. Using equation 2.49, the maximum hydration temperature is found to be 64°C, which is shown in figure 3.11. Several parameters are temperature dependent and to make an acceptable approximation of their values, they are evaluated at the mean of inlet temperature and the expected maximum hydration temperature, which is 45°C.

To monitor the development of the scalar quantities within the flow domain, three probes are positioned along the central axis of the REV at locations x=0.707mm, x=2.121mm and x=3.535mm. Their positions are shown in figure 3.12. The probes log the temperature and water vapour concentration every 1 second of simulated time (= 100 time steps). To investigate the effect of the inlet conditions, a parametric study is carried out with lower inlet concentrations, shown in table 3.2. These lower inlet concentrations should result in a noticeable decrease in overall reaction rate. It is chosen to lower the inlet concentrations with 5 and 10%, respectively.

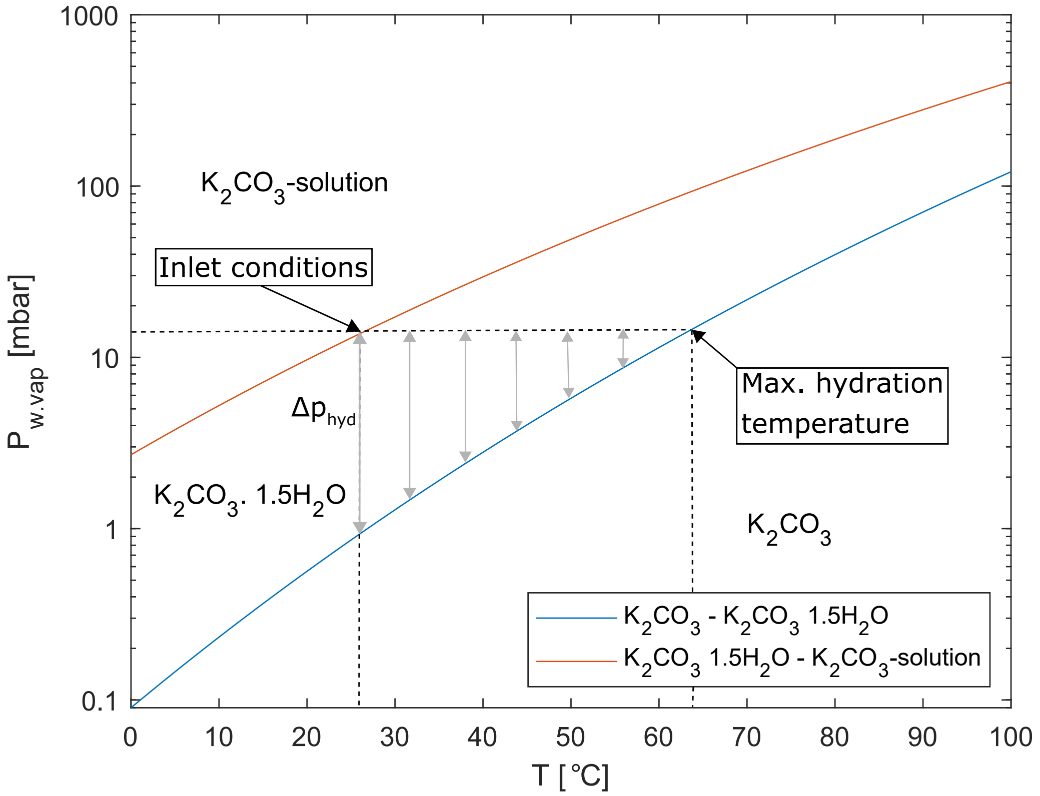

Figure 3.11: K_2CO_3 phase diagram. An inlet temperature of 26°C and an inlet vapour pressure of 14.99 [mbar] are used. At these conditions, a maximum hydration temperature of 64°C is expected.

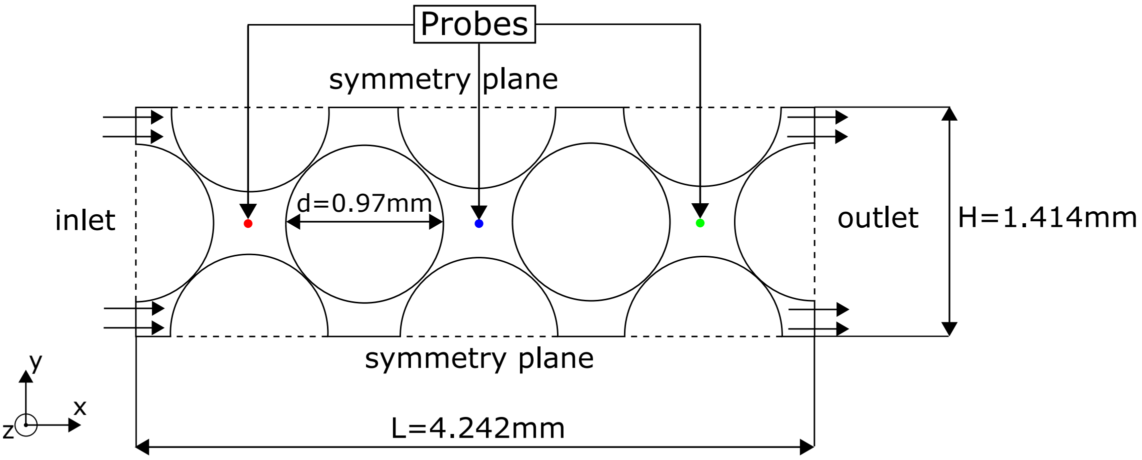

Figure 3.12: Locations of the probes for logging the temperature and concentration, which is done every 100 time steps (= 1 second).

Table 3.2: Inlet conditions used in the parametric study.

Case	Inlet temperature [°C]	Inlet concentration [mol/m^3]	Partial pressure [mbar]
Base	26	0.603	14.99
1	26	0.542	13.48
2	26	0.483	12.00

Time stepping is done with steps of 0.01s. Larger time steps result in an unstable model due to negative water vapour concentrations. A temporal independence study can be found in Appendix B.2. For a validation of the solver, it is referred to Appendix A. Here the velocity profile, heat transfer and conservation of mass and energy are evaluated. All residual controls are set to 1e-6. This is a regular choice for CFD studies.

Table 3.3: Inlet conditions and parameters used in the numerical study. Conditions are 26°C and 14.99 [mbar] partial water vapour pressure.

Symbol	Description	Value	Source
T_{in}	Inlet temperature	26 [°C]	[-]
$T_{p,i}$	Particle initial temperature	26 [°C]	[-]
c_{in}	Inlet concentration	0.603 [mol/m^3]	[-]
ν	Kinematic viscosity	1.74e-5 [m^2/s]	[65]
D_c	Diffusivity of water vapour in air	3.3e-5 [m^2/s]	[65]
ρ_f	Density of air	1.11 [kg/m^3]	[19]
$c_{p,f}$	Specific heat capacity moist air	1006.0 [J/kgK]	[19]
ρ_s	Density of K_2CO_3	2255.0 [kg/m^3]	[2]
$c_{p,s}$	Specific heat capacity K_2CO_3	830.0 [J/kgK]	[66]
E_a	Activation energy	46.22 [kJ/mol]	[67]
A_f	Pre-exponential factor	1.0838e6 [1/min]	[67]
R	Universal gas constant	8.314 [J/Kmol]	[-]
k_f	Thermal conductivity of moist air	0.026 [W/mK]	[68]
M_s	Molar mass K_2CO_3	0.136 [kg/mol]	[-]
ΔH	Enthalpy of hydration	61.54 [kJ/mol]	[67]

3.5 Results and discussion

This section contains the results of the hydration of the REV (see figure 3.3 for the geometry). The particle and REV conversion, conversion rates, temperature and concentration are presented and discussed. The terms "hydration" and "fractional conversion" are used synonymous. Unfortunately, due to time limitations the model was stopped after 25100 seconds ($\approx$ 7 hours) of simulated time.

In figure 3.13, the fractional conversion over time is shown for the particle rows. The first two rows (see figure 3.12) of particles are almost completely hydrated. Note that the purple line of row 1 is covered by the green line of row 2. The row closest to the outlet is just over 50% hydrated. The reaction progress differs per particle row. The first four rows start with a period of relatively fast reaction. The conversion curve obeys a typical R_3 shrinking core characteristic. This is also illustrated in figure 3.14, where the fractional conversion rate is plotted as a function of time (left) and fractional conversion (right). After the period of relatively fast reaction in rows 1-4, the reaction rates gradually decrease and become very low as α approaches 1. For rows 6 and 7, the initial hydration period is slower and starts more gradual, i.e. the reaction is ramped up. The ramping up of row 7 continues for approximately 1.5 hours and up to $\alpha \approx 0.1$, after which it enters the faster reaction phase where the largest part of the particle is hydrated.

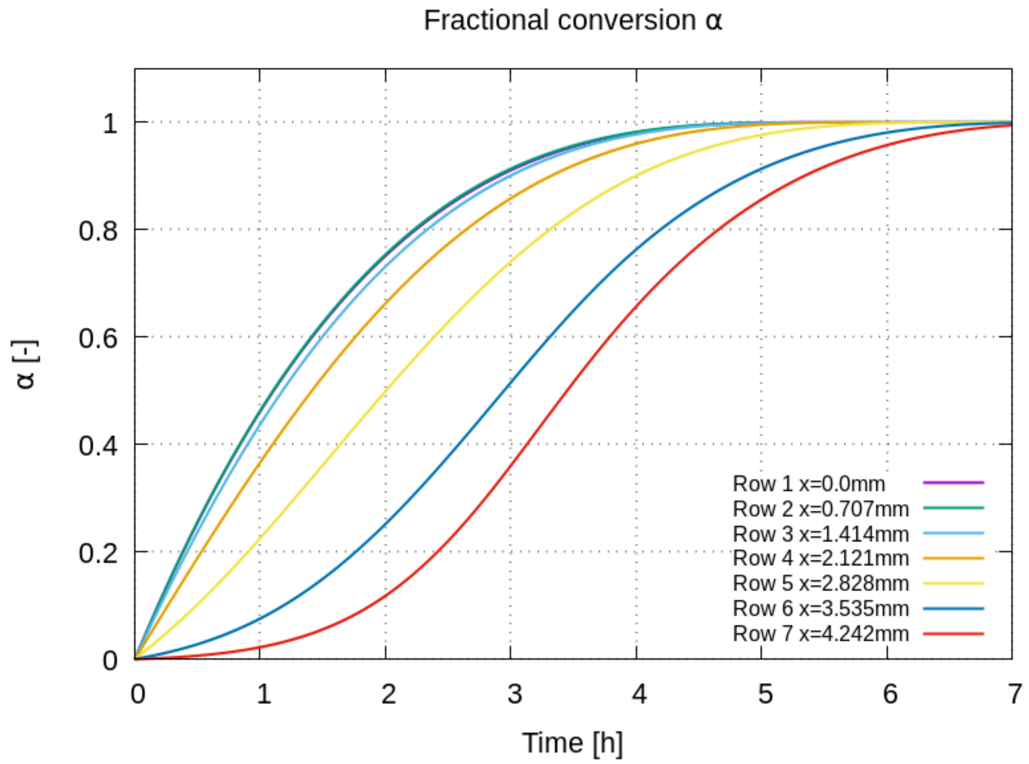

Figure 3.13: The fractional conversion over time for the particle rows in the REV. An inlet temperature of 26°C and an inlet concentration of 0.603 [mol/m^3] (=15 [mbar] partial pressure) are used. The simulation was stopped after almost 7 hours of simulated time.

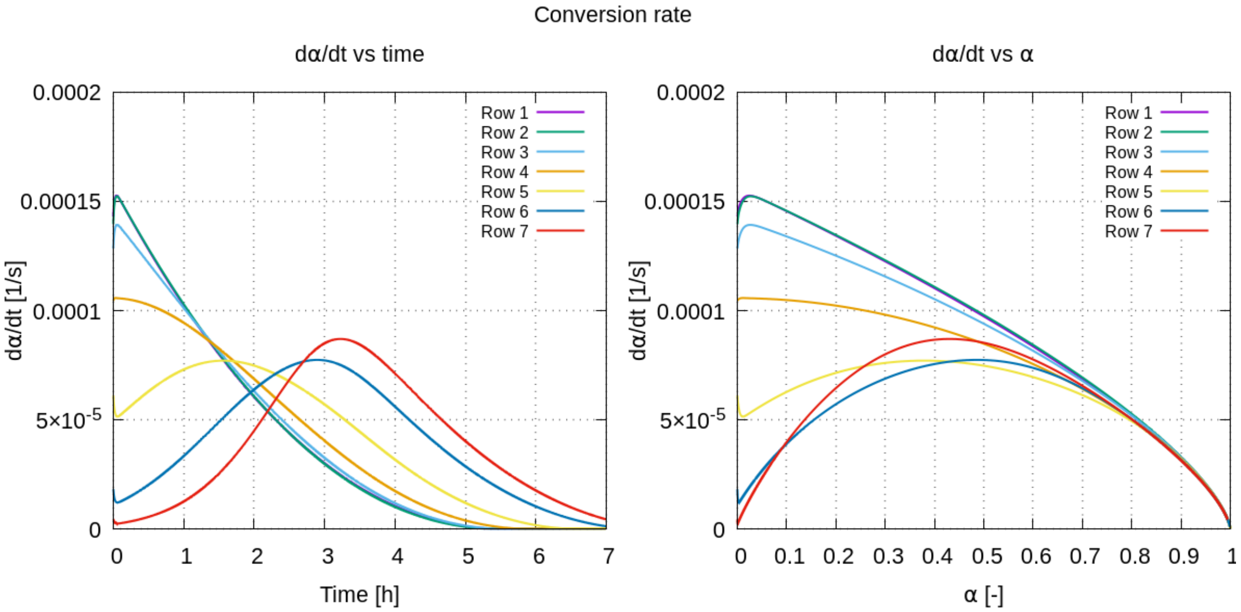

Figure 3.14: Fractional conversion rate of the particle rows. Left: $\frac{d\alpha}{dt}$ vs time; Right: $\frac{d\alpha}{dt}$ vs α. Maxima in conversion rate shift from the start of the reaction for the first rows, to the center of the reaction for rows further downstream. Note that the purple line of row 1 and the green line of row 2 are coinciding.

The streamwise location of the particle influences the reaction progression in the sense that the reaction rate maximum occurs later in time. Over the course of the hydration, the maximum hydration rate is found at the start of the reaction for the first particle rows. This is expected, because rows 1 and 2 are subjected to maximum water vapour concentration and minimum temperature, which results in a maximum driving force. For row 6 and row 7, the peaks appear to occur more in the vicinity of 50% hydration ($\alpha \approx 0.5$). It is remarkable that the maximum reaction rate of row 7 is larger than the maximum of row 6. The peak also occurs during a later stage of the hydration (at $\alpha = 0.4$ for row 7 while at $\alpha = 0.5$ for row 6). This may be caused by diffusion of temperature and water vapour against the direction of the flow. This takes place under particular conditions, characterized by the Péclet number. The thermal and mass Péclet numbers calculated using the conditions of the model are

$$Pe_T = \frac{u_i d_p}{k_f/(\rho_f c_{p,f})} = \frac{0.01 \cdot 0.00097}{0.026/(1.11 \cdot 1006)} = 0.42 \tag{3.1}$$

$$Pe_m = \frac{u_i d_p}{D_c} = \frac{0.01 \cdot 0.00097}{\text{3.3e-5}} = 0.29 \tag{3.2}$$

Since both Péclet numbers are between 0.1 and 1, advection cannot be neglected but diffusion is the dominant transport mechanism. This may indicate the presence of outlet effects, since downstream events can be ‘noticed’. This must be taken into account when designing an REV.

From the right plot of figure 3.14, it is observed that the fractional conversion rates for $\alpha > 0.8$ are independent of the streamwise location and are of equal magnitude. The term $(1-\alpha)^{2/3}$ of equation 2.52 is apparently dominant during this phase and dictates the conversion rate. Each particle row is subjected to different temperatures and concentrations, but this does not seem to affect the fractional conversion rate.

In figures 3.15 and 3.16 the probe temperatures and concentrations are displayed together with the fractional conversion. The early steep conversion curves of the first rows can be explained by the terms of the Arrhenius equation 2.52. At the start, the shape term $(1-\alpha)^{2/3}$ is large, while the temperatures are relatively low. Moreover, the local water vapour concentration is close to the inlet concentration. Further downstream, water vapour is taken up by the particles and the concentration decreases. Combined with the higher equilibrium pressure caused by the increased temperature, this results in a slower reaction. This is also observed in Appendix D, where the probe temperatures and concentrations are displayed along with the REV average of the fractional conversion rate.

From figure 3.15 it is observed that the REV temperature does not come near the maximum hydration temperature of 64°C, but reaches just over 29°C. However, as hydrating particles generate heat, probes 2 and 3 log higher temperatures. In a longer REV the temperatures near the outlet would further approach maximum hydration temperature. The concentration is lower for the probe near the outlet. After approximately 3.5 hours, the majority of the REV is hydrated and the temperatures start to decrease. In figure 3.16 this is observed as well. After the majority of the REV is hydrated, the probe concentrations start to increase and the first probe already reports water vapour concentrations near the inlet level of 0.603 [mol/m^3]. The fact that both the temperature and the concentration are approaching inlet conditions, partially validates the model (in particular the use of an REV), since the inlet conditions are shifting through the domain along with the reaction front.

In all of the figures in this section it can be observed that the fractional conversion of row 1 and row 2 is virtually identical. An explanation for this is found in the inlet conditions that have been used. A uniform temperature and concentration have been applied at the inlet. Using spatial profiles would have been preferred, because the thermal and concentration boundary layers are then formed immediately at the first particle row. As a result, temperature and water vapour concentration are better distributed across the inlet plane. Row 2 would experience a higher temperature (from heat generated by row 1) and lower water vapour concentration (taken up by row 1).

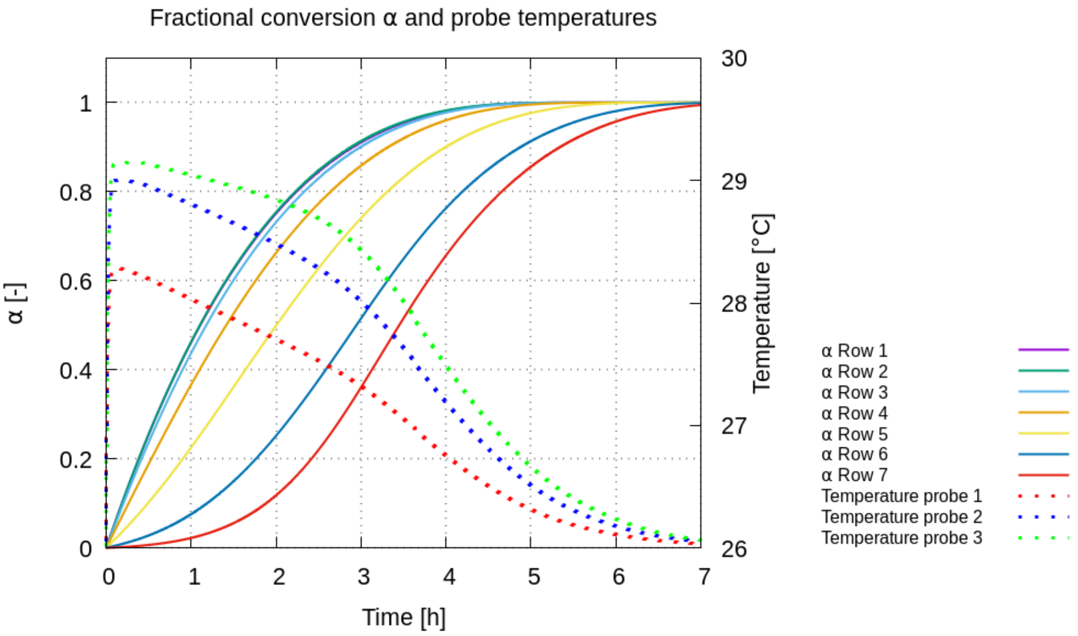

Figure 3.15: Fractional conversion of the particle rows and probe temperatures. The maximum hydration temperature of 64°C from the phase diagram is not reached. Only a 3°C increase in temperature is generated.

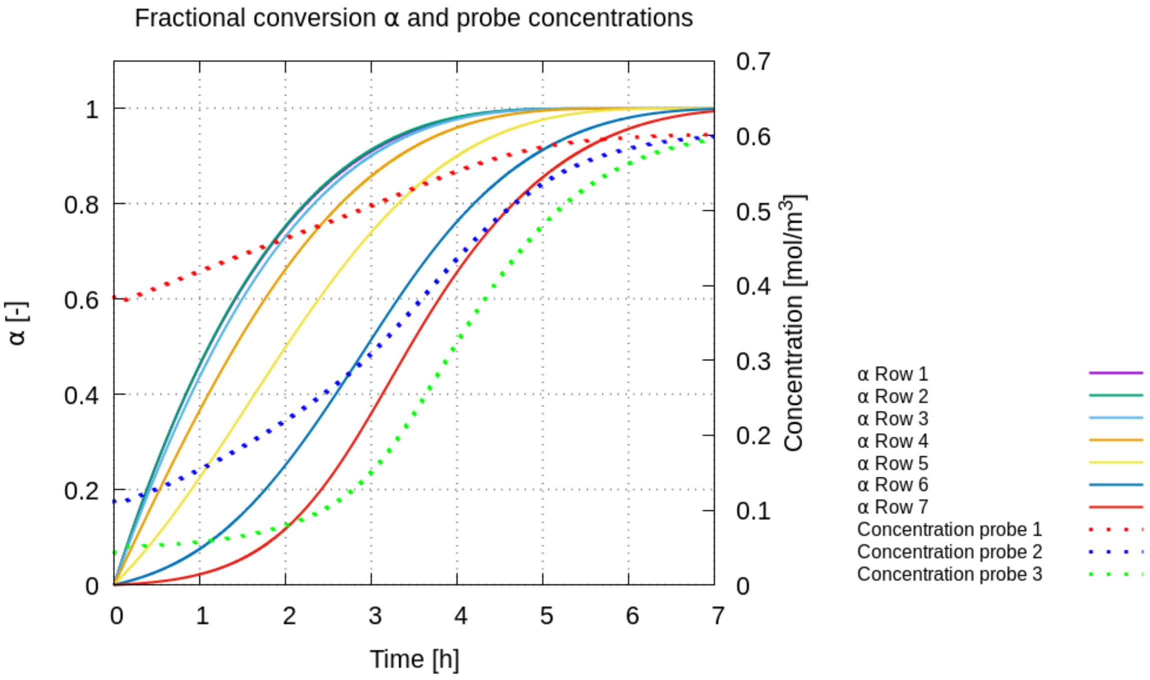

Figure 3.16: Fractional conversion of the particle rows and probe water vapour concentrations. A steeper increase in water vapour concentration is reported by probe 3 as most of the REV is hydrated.

As inlet effects are less prominent further downstream in the REV, the last row most closely represents the bulk of the packed bed reactor. The observation that the hydration progression still changes significantly per particle row, reveals the largest shortcoming of this geometry: it is too short. In a properly designed REV inlet effects cannot be present, because the inlet only comprises a minor portion of the full scale reactor. In an REV of sufficient length the hydration curves from the particle rows are expected to be identical. Estimating from figure 3.13, it is predicted that at least a tripling of the REV length is required to achieve this. If outlet effects are also to be taken into account, an even further extension of the REV is required.

3.5.1 Effect of inlet water vapour pressure

By varying the inlet water vapour concentration, the course of hydration is influenced. Since the base case already used inlet conditions at near-deliquescense, decreasing the inlet concentration while keeping the inlet temperature at 26°C is the only option. The effect of the inlet concentration is shown in figure 3.17, where the REV conversion and conversion rate averages (averages of all 32 particles) are plotted. As expected, the REV hydrates at a slower pace for lower inlet concentrations due to a smaller driving force. In the right figure the reaction rate is plotted against time and it can be observed that the curves have a more or less equal slope. Furthermore, a noticeable drop in reaction rate is visible. This drop occurs at $t \approx 3$ hours for the base case (orange line). For the cases with lower inlet concentrations (blue and red line) the reaction rate starts decreasing at a later moment. This event takes place at approximately the same fractional conversion for all cases. This points to the shape term $(1-\alpha)^{2/3}$ (which has an increasingly steeper negative slope) dictating the reaction rate.

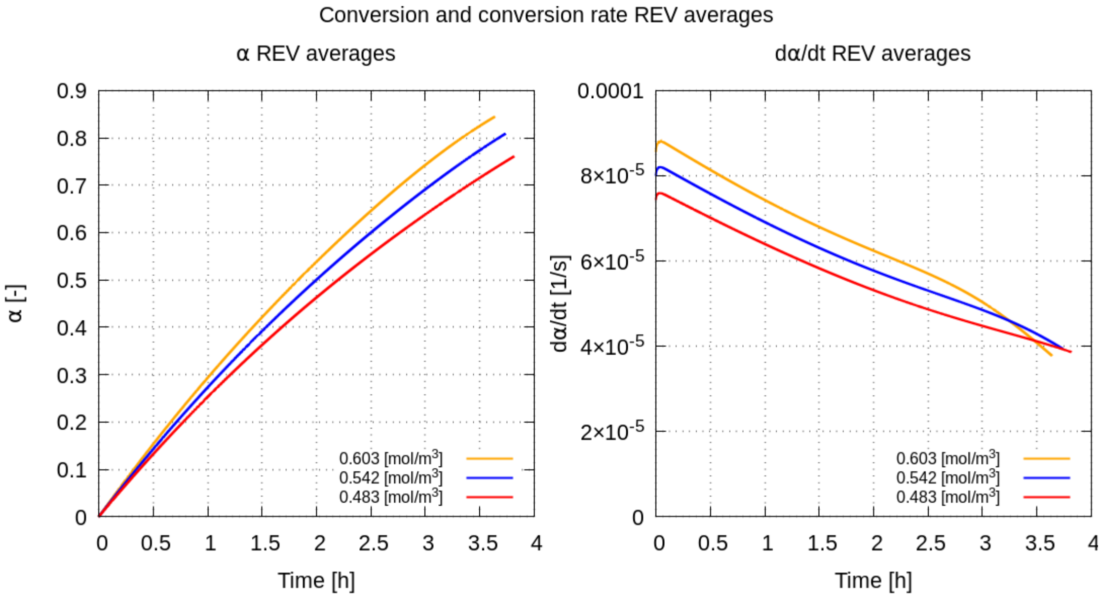

Figure 3.17: α and $\frac{d\alpha}{dt}$ REV averages, for different inlet concentrations. The water vapour concentrations 0.603, 0.542 and 0.483 [mol/m^3] correspond to 14.99, 13.48 and 12.00 [mbar] of partial pressure. Left: fractional conversion REV averages; Right: conversion rate REV averages.

Chapter 4

Numerical study: pressure drop and heat transfer in an REV

Pressure drop is an important characteristic for a particle bed as it is of influence on its energy efficiency. For beds that cause a large pressure drop the energy input has to be increased to overcome the resistance encountered by the air during its trajectory through the bed. In the past, several semi-empirical relations obtained from experiments and numerical models have been proposed to correlate the velocity and porosity to the pressure drop over a packed bed (see section 2.3.2). When modelling packed beds using spatial discretization, choices have to be made on how to model the zero-dimensional particle-particle contacts. This is necessary to obtain a stable model that can provide valid results. There are four methods, which have been discussed in section 2.1.2. The chosen particle contact treatment will have effect on the pressure drop. Therefore, in this chapter a comparison is made between the pressure drop obtained from the numerical model and the Kozeny-Carman, Ergun and KTA equations and what the effect is of the chosen particle contact modelling method.

Heat transfer is another process that is highly influential on the performance of a heat battery. The better facilitated the transfer of heat between fluid and solid is, the faster a reactor can be hydrated and the more thermal power can be generated. The (convective) heat transfer coefficient expresses the ease of energy flux through an interface between a solid body and an adjacent fluid region and is therefore an important parameter when evaluating the performance of a reactor. This chapter evaluates the effect of the particle contact method on heat transfer. This is done by comparing the heat transfer coefficient obtained from the model to the Wakao&Kaguei, Whitaker and Gnielinski equations.

Similar to the previous chapter, an REV of 32 particles in FCC configuration is used. Four different geometries are used in this chapter and they are all derivatives of one base geometry. The base geometry is show in figure 4.1. Considering the case setup, the thesis of Gaeini [12] is used as a work of reference. In his experimental setup, the flow rate could be varied from 0-150 [l/min], corresponding to superficial velocities of 0-0.65 [m/s]. Particles of 1.5mm were used in his experiments, resulting in a maximum Reynolds number of 61 (given that $\nu = 1.59 \cdot 10^{-5}$ [m^2/s]). Therefore, the following Reynolds number series is chosen: [0.25, 0.5, 0.75, 1, 2.5, 5, 7.5, 10, 25, 50, 75]. It must be noted that in this thesis, particles with d_p = 1mm are used, as was in the work of Lan [19] where dehydration was modelled in a fashion similar to Chapter 3. Varying the Reynolds number is done by varying the interstitial velocity according to the following equation which is obtained by substituting equation 2.2 into 2.6 and rearranging:

$$u_i = \frac{Re\nu}{d_p\epsilon},$$

where ν [m^2/s] is the kinematic viscosity of air, d_p [m] is the particle diameter and ϵ [-] is the packed bed porosity.

4.1 Geometry

When modelling a packed bed with spherical particles, extra attention must be paid to the contact points between two adjacent particles. This is necessary to avoid mesh degradation. In section 2.1.2 several method were discussed and in Chapter 3 the gaps method was selected for the modelling of the hydration process of the REV. In this chapter, the effect of the chosen particle contact modelling method on pressure drop and heat transfer is studied. For each of the four methods, a geometry is constructed which is derivative of the base geometry which is shown in figure 4.1.

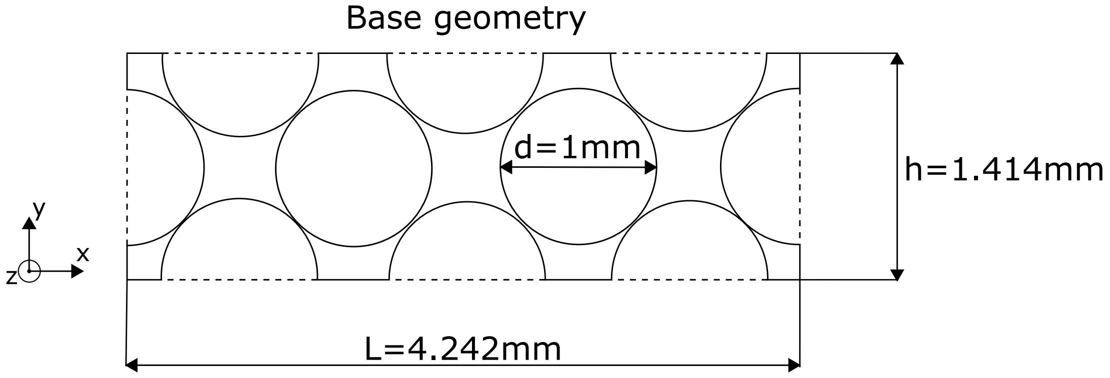

Figure 4.1: Base geometry used in the pressure drop and heat transfer model.

The base REV consists of an FCC lattice of 32 particles with $d_p = 1\text{mm}$: one unit cell in width and height, and three unit cells in length. The four contact modelling methods which were discussed earlier in section 2.1.2 are used here:

1. The **gaps** method has already been discussed in the previous chapter. Particles are shrunk by 3% so that a gap exists at the would-be particle contact. REV porosity = 0.32.
2. The **increase** method causes circular shared patches to be created at the particle contact zones. The particle diameter is increased by 3%. REV porosity = 0.20.
3. In the **bridges** method cylindrical connections with 0.15mm radii are placed at the contact zones. REV porosity = 0.25.
4. The **caps** method is similar to the bridge method, except that now a cylindrical volume is removed. The caps are given a radius of 0.15mm. REV porosity = 0.27.

The four REVs are shown in figure 4.2. As the Reynolds number and pressure drop is calculated through equations using particle diameter d_p, a modified diameter must be determined for the increase, bridges and caps geometries (the particles are no longer spherical). Therefore, use is made of the particle equivalent diameter [69], which is defined as

$$d_p^* = \frac{6V_p}{A_p\phi_p}, \tag{4.1}$$

in which V_p is the particle volume, A_p is the particle surface area and ϕ_p is the sphericity of the particle which can be defined as

$$\phi_p = \frac{(36\pi V_p^2)^{1/3}}{A_p} \tag{4.2}$$

The sphericities and equivalent particle diameters are shown below in table 4.1.

Table 4.1: The sphericities and equivalent particle diameters of the geometries according to equations 4.2 and 4.1, respectively.

Geometry	d_p [mm]	ϕ_p [-]	d_p^* [mm]
Gaps	0.97	1	0.970
Increase	1.03	0.99	1.025
Bridges	1	0.94	1.006
Caps	1	0.994	0.994

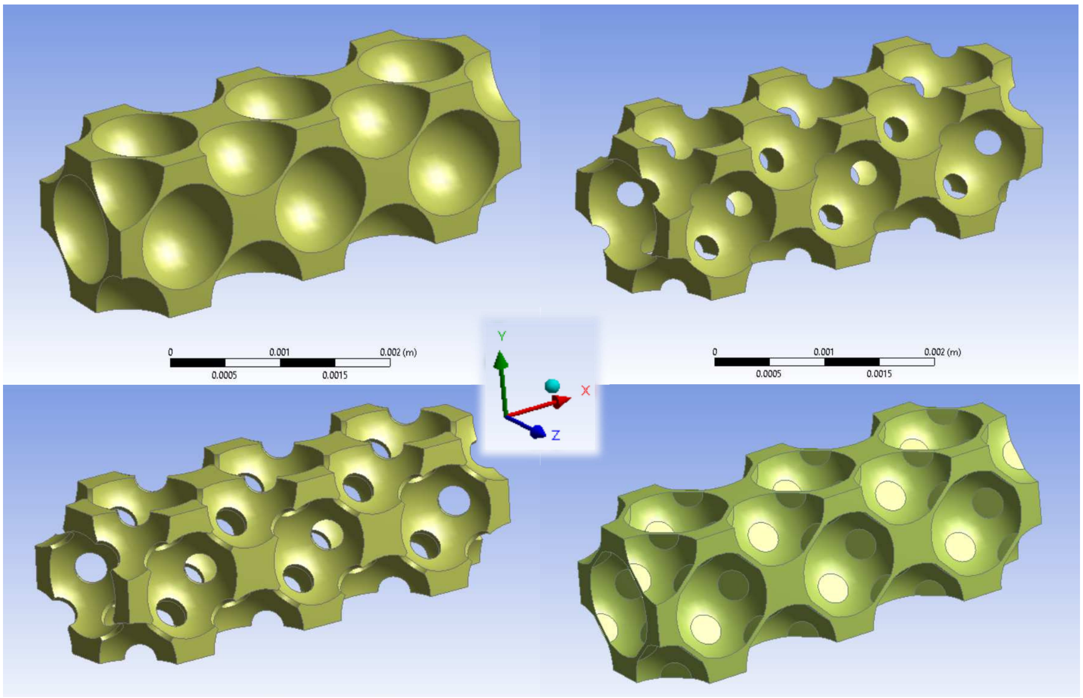

Figure 4.2: The four geometries used in the pressure drop and heat transfer study. Clockwise, from top left: gaps; increase; caps; bridges.

4.2 Mesh

Body-fitted unstructured meshes are used to discretize the geometries. The overall cell size is set to 0.244mm, while a face cell sizing of 0.0487mm is applied to the particle faces. The meshes include two inflation layers on the particle surfaces with a combined thickness of 0.01mm. This is the maximum thickness that allows for the intermediate cells to be of sufficient quality. Skewness targets are set to 0.8. Geometry and mesh information can be found in table 4.2.

Table 4.2: Geometry and mesh information for the pressure drop and heat transfer study.

Method	Porosity	Cells	Bridge/cap radius	Overall cell size	Particle face cell size
Gaps	0.32	229323	-	0.244mm	0.0487mm
Increase	0.2	196459	-	0.244mm	0.0487mm
Bridges	0.25	196930	0.15mm	0.244mm	0.0487mm
Caps	0.27	216002	0.15mm	0.244mm	0.0487mm

4.3 Physics

In this study the emphasis is put on pressure and transport of temperature. Therefore, it is chosen to adapt the simpleFoam solver, which solves for a steady-state, incompressible flow. Additional to the equations for conservation of mass (equation 2.32) and momentum (equation 2.33), the convection-diffusion equation for temperature (equation 2.20) is solved (note that the transient term $\frac{\partial T}{\partial t}$ drops out of the latter due to the steady-state condition):

$$\nabla \cdot \boldsymbol{u} = 0 \tag{2.32}$$

$$\boldsymbol{u} \cdot \nabla \boldsymbol{u} = \nu \nabla^2 \boldsymbol{u} - \frac{1}{\rho_f} \nabla p \tag{2.33}$$

$$\boldsymbol{u} \cdot \nabla T = D_T \nabla^2 T, \tag{2.20}$$

where $\boldsymbol{u}$ [m/s] is the velocity, ν [m^2/s] is the kinematic viscosity, ρ_f [kg/m^3] is the density of the fluid, T [K] is the temperature and D_T [m^2/s] is the thermal diffusivity. Parameters used in this study are listed in table 4.3. The SIMPLE algorithm is used to solve for the velocity and pressure (see figure 3.7). An inlet velocity according to the Reynolds number and temperature are prescribed at the inlet. Symmetry conditions are applied at the side boundaries. Neumann (zero-gradient) conditions are applied at the outlet for the velocity and temperature. This is done because the velocity and temperature here are not known a priori and are also not expected to change significantly at the outlet. The outlet pressure is kept constant at zero. For an illustration of the boundary conditions, see figure 4.3. Convergence limits are set to 1e-6 for the velocity, pressure and temperature.

Table 4.3: Parameters used in the pressure drop and heat transfer study.

Symbol	Description	Value
ν	Kinematic viscosity	1.59e-5 [m^2/s]
D_T	Thermal diffusivity	2.19e-5 [m^2/s]
ρ_f	Density air	1.18 [kg/m^3]
$c_{p,f}$	Heat capacity air	1006 [J/kgK]
k	Thermal conductivity air	0.026 [W/mK]

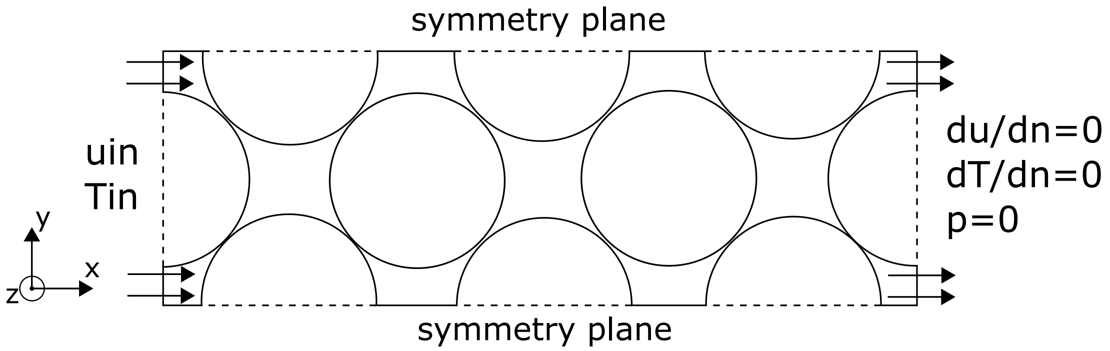

Figure 4.3: Computational domain used in the pressure drop and heat transfer study. Neumann (zero-gradient) conditions are applied at the outlet because the velocity and temperature here are not known a priori and also will not change significantly here. Particle temperatures are shown in figure 4.4.

In order to establish valid heat transfer coefficient and pressure drop values, velocity and temperature inlet profiles have to be developed. Normally this is done using periodic boundary conditions. Unfortunately this is not possible in this case, as the particle surfaces serve as heat sink. Therefore, an alternative approach is adopted. For the temperature, a gradient is generated by gradually reducing the temperature of the particles, according to streamwise position (upstream particles are hotter). When the air has passed through the first two unit cells, the velocity and temperature profiles are expected to be fully developed. The new “inlet” pressure and temperature are then taken as the average over the interface between the second and third unit cells. The particles downstream of this new inlet have a constant temperature. This is illustrated in figure 4.4.

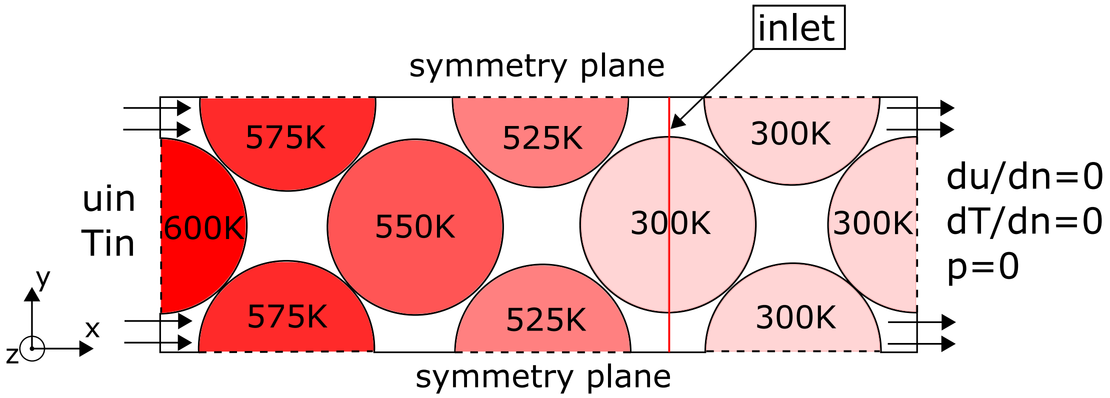

Figure 4.4: Computational domain for the pressure drop and heat transfer model. An inlet temperature is applied at the REV inlet and the air is subsequently cooled by the particles that decrease in temperature according to their streamwise location. At the new “inlet” a velocity and temperature profile will have been developed.

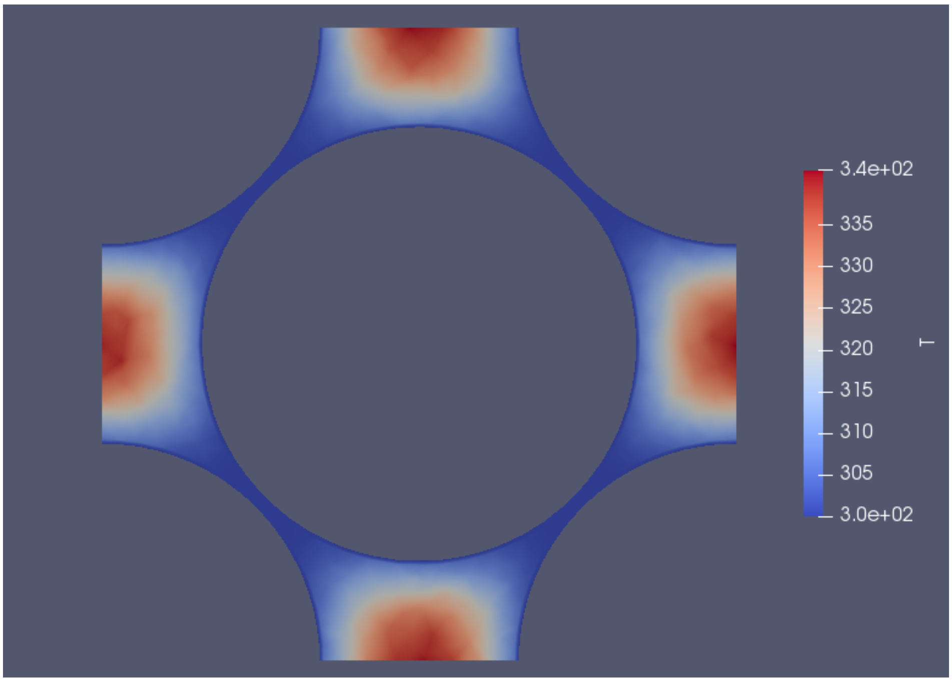

Figure 4.5: Example of a temperature inlet profile, for the gaps geometry and $Re = 1$. Fluid temperatures near the cool particle surfaces are noticeably lower. This particular inlet profile has an average temperature of 314.5K.

The choice is made to apply a large temperature difference so that the rounding errors are relatively small. In figure 4.5, an example of a temperature inlet profile is shown.

4.4 Results and discussion

Pressure drop and heat transfer are important aspects of the heat battery. In this chapter, these two phenomena are studied using an REV. To provide reference and perspective, values obtained from the numerical model are compared with correlations from literature. In this section the results are presented and discussed.

4.4.1 Pressure drop

The results obtained from OpenFOAM is a converged velocity and pressure field, as shown in figure 4.6. It must be noted that because simpleFoam is an incompressible solver, the shown pressure is the pressure divided by the density of the fluid.

A velocity pattern is expected to be established after two unit cells downstream from the inlet. It is therefore assumed that a representative pressure measurement can be taken from this location. The pressure is determined by taking a slice of the domain at this location and calculating the average pressure on this slice. To this end, use is made of an area-weighted pressure according to:

$$p_{slice} = \frac{\sum\limits_{i=0}^{I} p_i A_i}{\sum\limits_{i=0}^{I} A_i}, \tag{4.3}$$

in which (for element slice i) p_i is the pressure and A_i is the in-plane surface area. This operation yields a pressure in the form of p/ρ. To obtain a pressure drop in the form $\frac{\partial p}{\partial x}$, the calculated average pressure is multiplied by the chosen density of the fluid ($\rho_{air} = 1.18$ [kg/m^3]) and subsequently divided by the length of the unit cell (= 1.414mm):

$$\frac{p}{\rho_f} \xrightarrow{\times \rho_f} p \xrightarrow{/l} \frac{\partial p}{\partial x} \tag{4.4}$$

As was discussed in section 2.3.2, past work on pressure drop has resulted in a range of equations that relate the velocity in a porous medium to the pressure drop over the medium. In this work, the pressure drop values calculated using these correlations are compared to what was obtained from the numerical model. The correlations that are used are the Kozeny-Carman (K-C) [55, 56], Ergun [53] and KTA [57] equations:

$$\frac{\partial p}{\partial x} = \frac{u_s \mu}{K} \tag{2.40}$$

$$\frac{\partial p}{\partial x} = 150 \frac{(1-\epsilon)^2}{\epsilon^3} \frac{\mu}{d_p^2} u_s + 1.75 \frac{1-\epsilon}{\epsilon^3} \frac{\rho_f}{d_p} u_s^2 \tag{2.39}$$

$$\frac{\partial p}{\partial x} = \frac{3}{Re^{0.1}} \frac{(1-\epsilon)^{1.1}}{\epsilon^3} \frac{\rho_f}{d_p} u_s^2 + \frac{160}{Re} \frac{(1-\epsilon)^2}{\epsilon^3} \frac{\rho_f}{d_p} u_s^2 \tag{2.41}$$

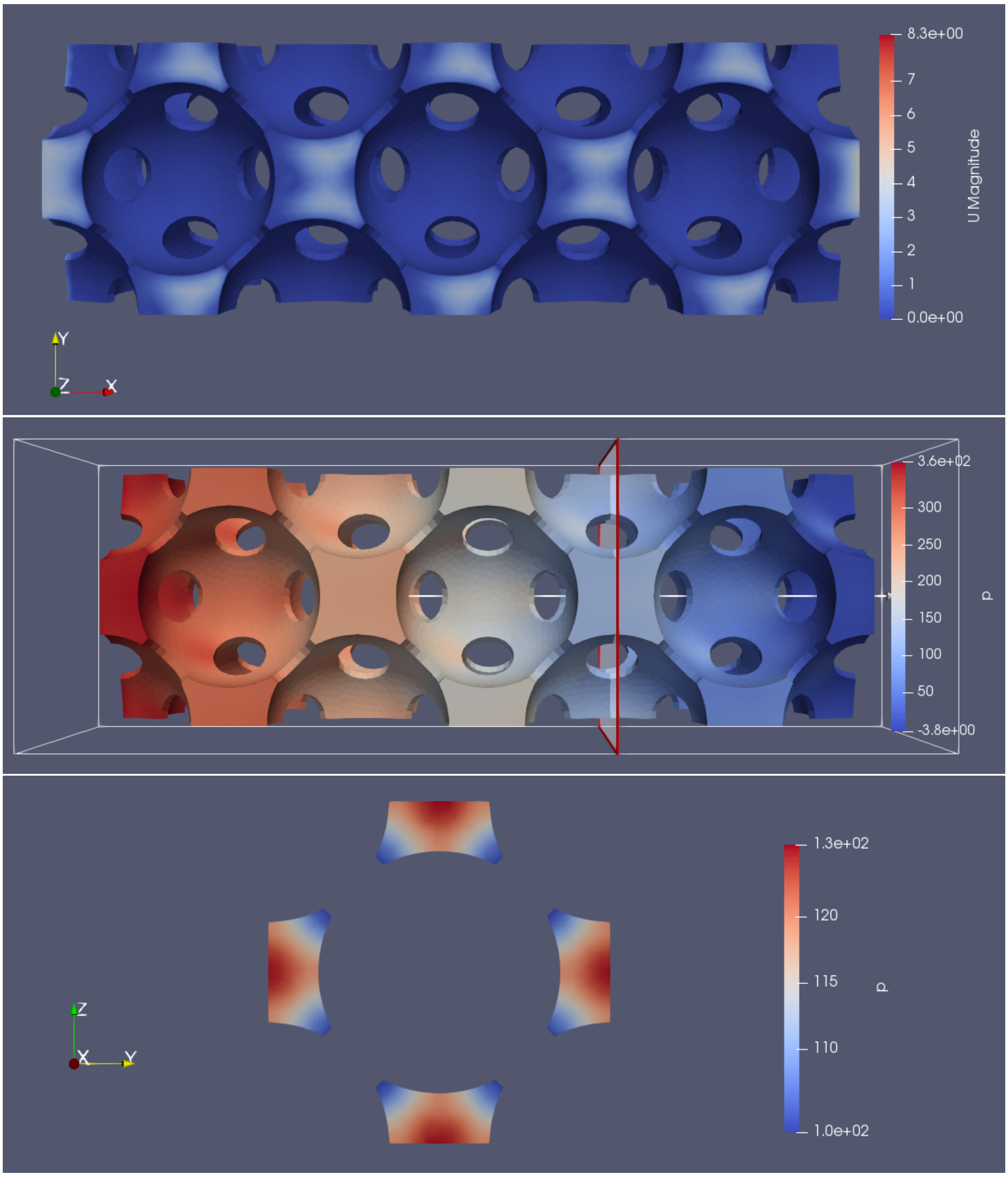

Figure 4.6: The velocity (top) and pressure (center) fields for the bridge geometry. The flow is assumed to be developed after two unit cells. The pressure decreases throughout the volume to reach the prescribed boundary condition of 0 at the outlet. It must be noted that because simpleFoam is an incompressible solver, the shown pressure is the pressure over density. The pressure drop is determined by averaging over the slice surface (bottom).

The permeability K in equation 2.40 is calculated using equation 2.36. The above equations were established under certain experimental conditions:

- Ergun:
  - $1 < Re < 2.4 \cdot 10^3$
  - Particles were randomly packed.

  - Different shapes of particles were used.

- KTA:
  - $1 < Re_p < 10^5$
  - $0.36 < \epsilon < 0.42$
  - Negligible wall effects: with the reactor to particle diameter ratio chosen large enough, wall effects were regarded negligible.
  - Bed length at least four times the particle diameter.
  - Particles were randomly packed.

- K-C:
  - $Re_p < 1$
  - Use of capillary tubes to determine the permeability.
  - Spherical particles were randomly packed.

In figure 4.7 the numerical results are compared with the values from the K-C, Ergun and KTA equations. A differentiation is made between the range $0 < Re \leq 1$ where the K-C equation is valid and the range $Re \geq 1$ where the Ergun and KTA equations are valid. The figure shows that for the upper Reynolds range, there is hardly any difference between the Ergun and KTA equations. At first glance, the caps method appears to be giving the most comparable results for the entire range, followed by the increase and gaps methods. The figure demonstrates that the bridges method is the least close to the K-C and Ergun equations. A shared trait is that for all geometries the deviation from the Ergun correlation becomes visibly larger with increasing Reynolds numbers.

Now that it is clear that none of the contact modelling methods yield values that match completely with the correlations from literature, it may be interesting to quantify their 'closeness' to the K-C and Ergun equations. Therefore their average relative errors are calculated. Since the Reynolds numbers at which the pressure drop is evaluated are not linearly spaced, use is made of a weighting-by-range error. This error is defined as

$$E = \frac{1}{W}\sum_{i=0}^{I} w_i e_i, \tag{4.5}$$

in which w_i is the range of entry i, W is the total range and e_i is the relative error of entry i to Ergun. w_i is defined as

$$w_i = \frac{Re_i + Re_{i+1}}{2} - \frac{Re_{i-1} + Re_i}{2} = \frac{Re_{i-1} + Re_{i-1}}{2} \tag{4.6}$$

and e_i is defined as

$$e_i = \frac{|\frac{\partial p}{\partial x}_{i,model} - \frac{\partial p}{\partial x}_{i,literature}|}{\frac{\partial p}{\partial x}_{i,literature}} \tag{4.7}$$

The errors of the four geometries are shown in table 4.4.

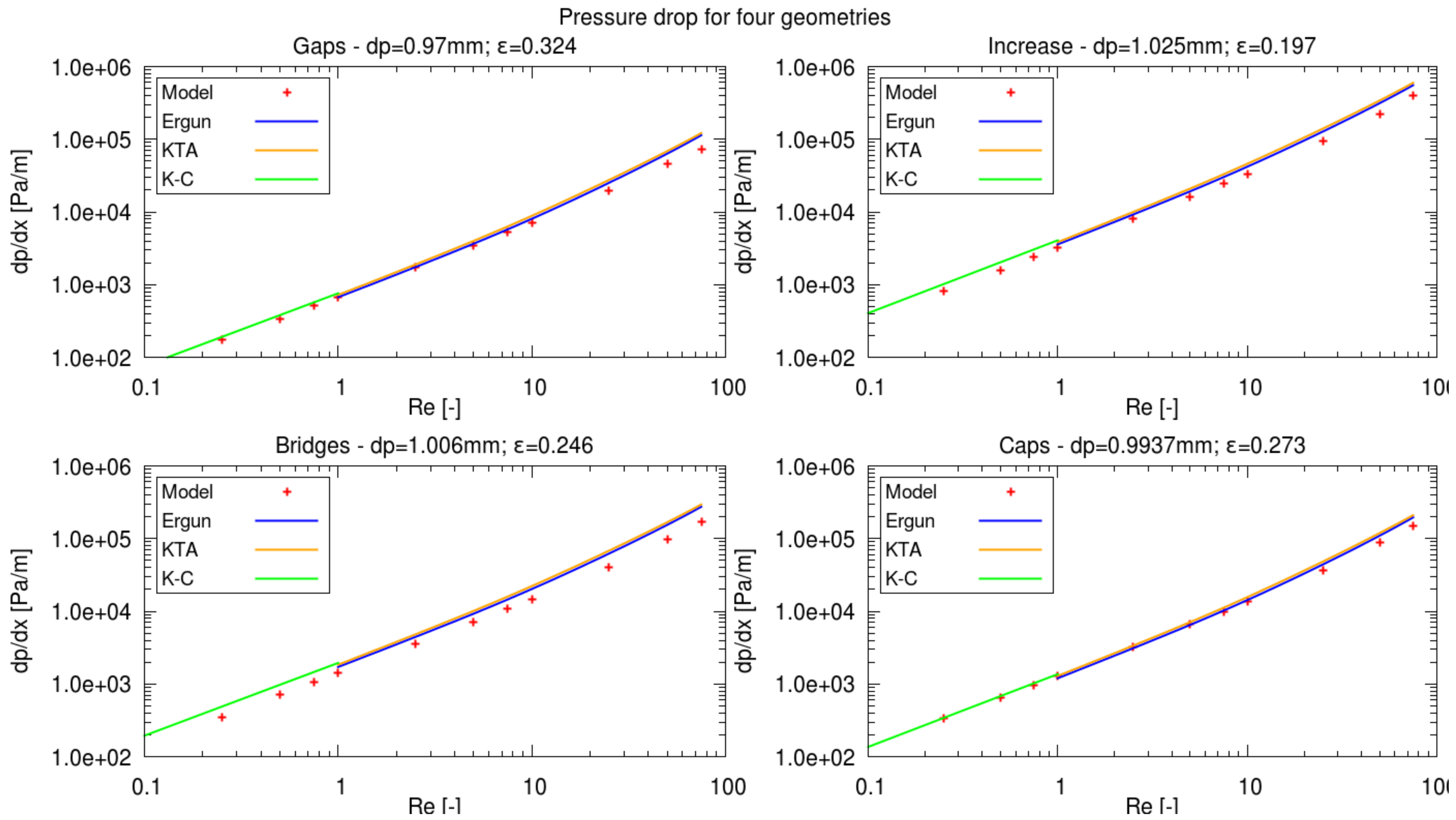

Figure 4.7: Numerical results for the pressure drop compared with results from the K-C, Ergun and KTA equations. The capping method appears to be giving the closest results to the K-C equation for $Re \leq 1$ and the Ergun equation for $Re \geq 1$.

Table 4.4: Average relative errors to the K-C and Ergun equations.

Geometry	Average relative error to K-C	Average relative error to Ergun
Gaps	0.097	0.203
Increase	0.232	0.232
Bridges	0.328	0.318
Caps	0.038	0.132

From the relative errors, it is clear that the caps method is, with distance, the method that gives the closest match to what literature provides. In the lower Reynolds range, the gaps method is not too far off from the K-C equation. In the higher range the relative error is significantly larger, but still the second-best choice between the four geometries. The increase method gives a comparatively high relative error for both Reynolds ranges. The bridges method is an outlier with very high errors.

The overestimation of Ergun (or the underestimation of the CFD model) was already observed by Ahmadi [58], and in their work they proposed to fit function 2.42 to the numerical results:

$$\frac{\partial p}{\partial x} = \frac{a}{Re_p^b}\frac{(1-\epsilon)^n}{\epsilon^3}\frac{\rho_f}{d_p}u_s^2 \tag{2.42}$$

The fit attempts, using the non-linear least squares method, are shown in figure 4.8. The R^2 values are close to 1, but this is because it is an absolute error and not a relative one. The result of this is that the fit at the lower Reynolds numbers appears to be worse in the log-log plot. However, at higher Reynolds numbers the fits have a higher goodness. Due to the high Reynolds number range (up to 1250000) that was investigated in [58], no Darcy term was included in equation 2.42 to account for viscous effects. This may be the reason for the inability of the proposed equation to result in a good fit for the Reynolds range that is evaluated here.

It has now been established that the caps and gaps methods can give results similar to the K-C and Ergun correlations. It would be interesting to adjust these geometries to obtain a geometrical model that approaches the ideal situation (touching spheres). For the caps method this would be implemented by decreasing the capping radius, while for the gaps method this would imply to reduce the shrinkage. However, both of these operations would reduce the space for intermediate cells between the particles and this would render the meshing of the geometry impossible with conventional meshing algorithms. Therefore, the increase method, which was the third best option, is selected: instead of using a 3% increase in particle diameter, a 1% increase could potentially give a closer approximation to experimental results. In order to obtain a mesh that is of acceptable quality, a large number of cells is required. To accommodate for the limitations of the meshing tool that is used (the student version of Ansys Mesh only allows for a maximum 512k cells), the geometry is shortened to two unit cells. Apart from this, an identical routine is carried out to obtain the results. Results are shown in figure 4.9. The relative errors to the K-C and Ergun equation are now 0.149 and 0.199, respectively. This is significantly smaller than the errors of the 3% increase geometry. Additionally, the proposed equation form 2.42 is plotted in the right figure. Also for the 1% increase geometry a proper fit can be found.

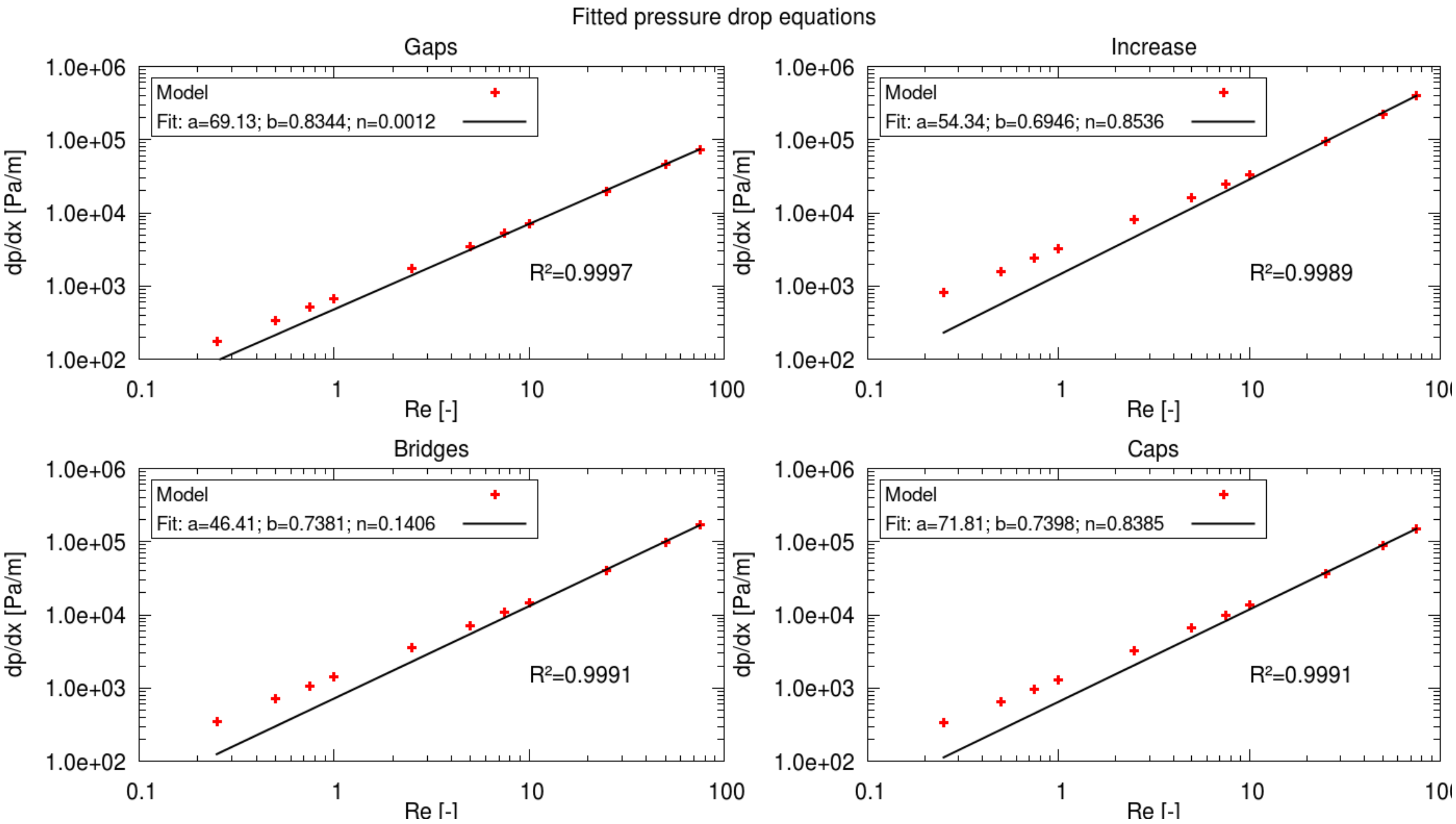

Figure 4.8: The fitted equations in the form of 2.42 to the numerical results. While a good fit is found in the higher range, the proposed equation cannot be used to determine pressure drop at low Reynolds numbers.

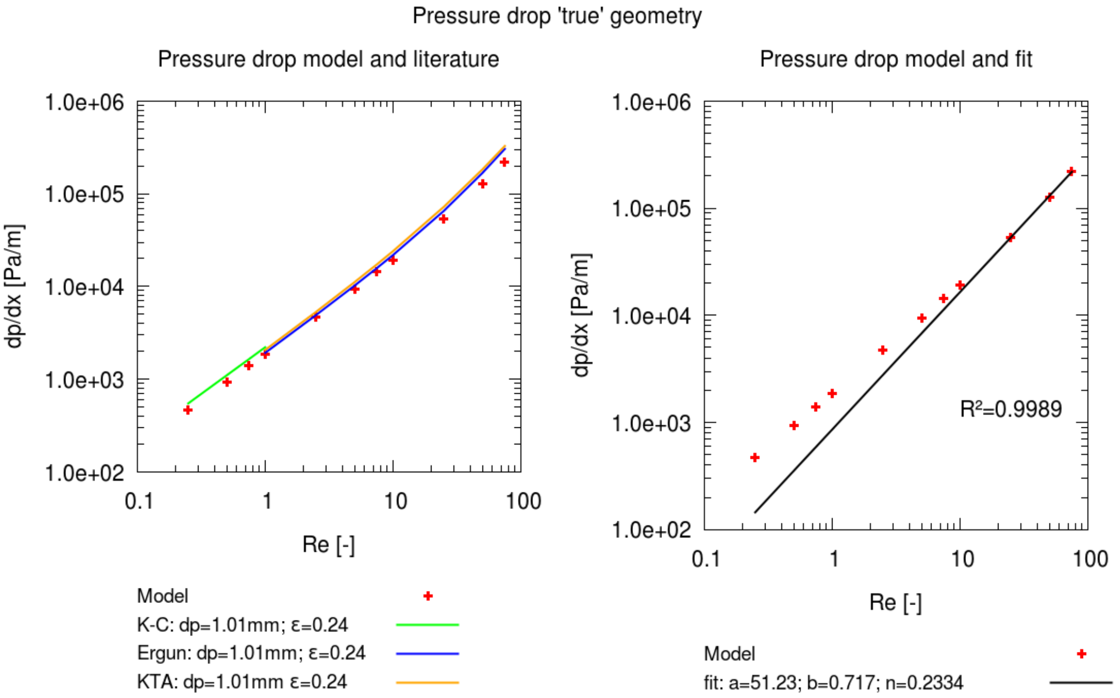

Figure 4.9: Pressure drop results for the geometry with a 1% increase in particle diameter.

4.4.2 Heat transfer

Heat transfer is one of the key aspects in a packed bed reactor. The better it is facilitated, the higher the potential output of thermal power. The heat transfer coefficient is therefore an important parameter to rate the reactor performance. It can be predicted through semi-empirical correlations for the Nusselt number. Numerous of these correlations can be found in literature, as was discussed in section 2.2.1. Relevant for heat batteries, some of them are also valid for low Reynolds numbers. These correlations are listed in table 4.5. Although some of the conditions mentioned may not exactly coincide with the conditions of the heat battery considered in this work, they are still included. This is done due to the work of Dave [44], where it was shown that these correlations may also yield comparable results outside of the circumstances under which they were established.

Other relations have been mentioned as well in Chapter 2, but the conditions (aside from the Reynolds number range) under which they are valid are deemed too dissimilar to the conditions of this thesis. The Ranz and Marshall equation [29] for example, is only valid for a single sphere in a laminar free stream. In this section a comparison is made between the relations from table 4.5 and the results from the model. Similar to the previous section, the four different particle contact modelling methods are evaluated. Note that in the calculations of the Reynolds and Nusselt numbers the equivalent particle diameter d_p^* from equation 4.1 is used. From the model, the heat transfer coefficient is calculated using equation 2.17

$$h = \frac{q}{A(T_f - T_s)}, \tag{2.17}$$

with the heat transfer surface area A [m^2], the fluid temperature T_f [K] and the solid temperature T_s [K]. From here the Nusselt number is calculated using

Table 4.5: Various Nusselt relations and the experimental conditions under which they were established.

Author	Correlation	Experimental conditions	Ref.
Wakao&Kaguei	$2 + 1.1Re^{1/2}Pr^{0.6}$	$Pr \approx 0.7$ $20 < Re < 3000$	[31]
Whitaker	$\frac{1-\epsilon}{\epsilon}\left(0.5\left(\frac{Re}{1-\epsilon}\right)^{1/2} + 0.2\left(\frac{Re}{1-\epsilon}\right)^{2/3}\right)Pr^{1/3}$	$Pr \approx 0.7$ $20 < Re < 80000$ $0.34 < \epsilon < 0.78$	[32]
Gnielinski	$(1 + 1.5(1-\epsilon))Nu_{sp}$	$0.7 < Pr < 10000$ $Re/\epsilon < 1.1 \cdot 10^7$ $0.24 < \epsilon < 0.935$	[35]

$$Nu = \frac{hd_p^*}{k_f}, \tag{2.4}$$

where k_f is the thermal conductivity of air. In equation 2.17 the heat flux q is determined by

$$q = \dot{V}\rho_f c_{p,f}(T_{in} - T_{out}),$$

where $\dot{V}$ [m^3/s] is the volumetric flux, ρ_f [kg/m^3] and $c_{p,f}$ [J/kgK] are respectively the density and heat capacity of air and $T_{in} - T_{out}$ [K] is temperature difference between inlet and outlet. The bulk temperature T_f (T_s is held constant) is determined by using the cup-mixing temperature (see equation 2.18), which in its discrete form is

$$T_f = \frac{\sum_{i=0}^{I} u_{x,i}T_iV_i}{\sum_{i=0}^{I} u_{x,i}V_i}, \tag{4.8}$$

in which $u_{x,i}$ is the magnitude of the velocity, T_i is the temperature and V_i is the volume of element i. T_{in} and T_{out} are the averages of a plane and therefore are weighted by flux, according to

$$T_{in,out} = \frac{\sum_{i=0}^{I} u_{x,i}T_idy_idz_i}{\sum_{i=0}^{I} u_{x,i}dy_idz_i}, \tag{4.9}$$

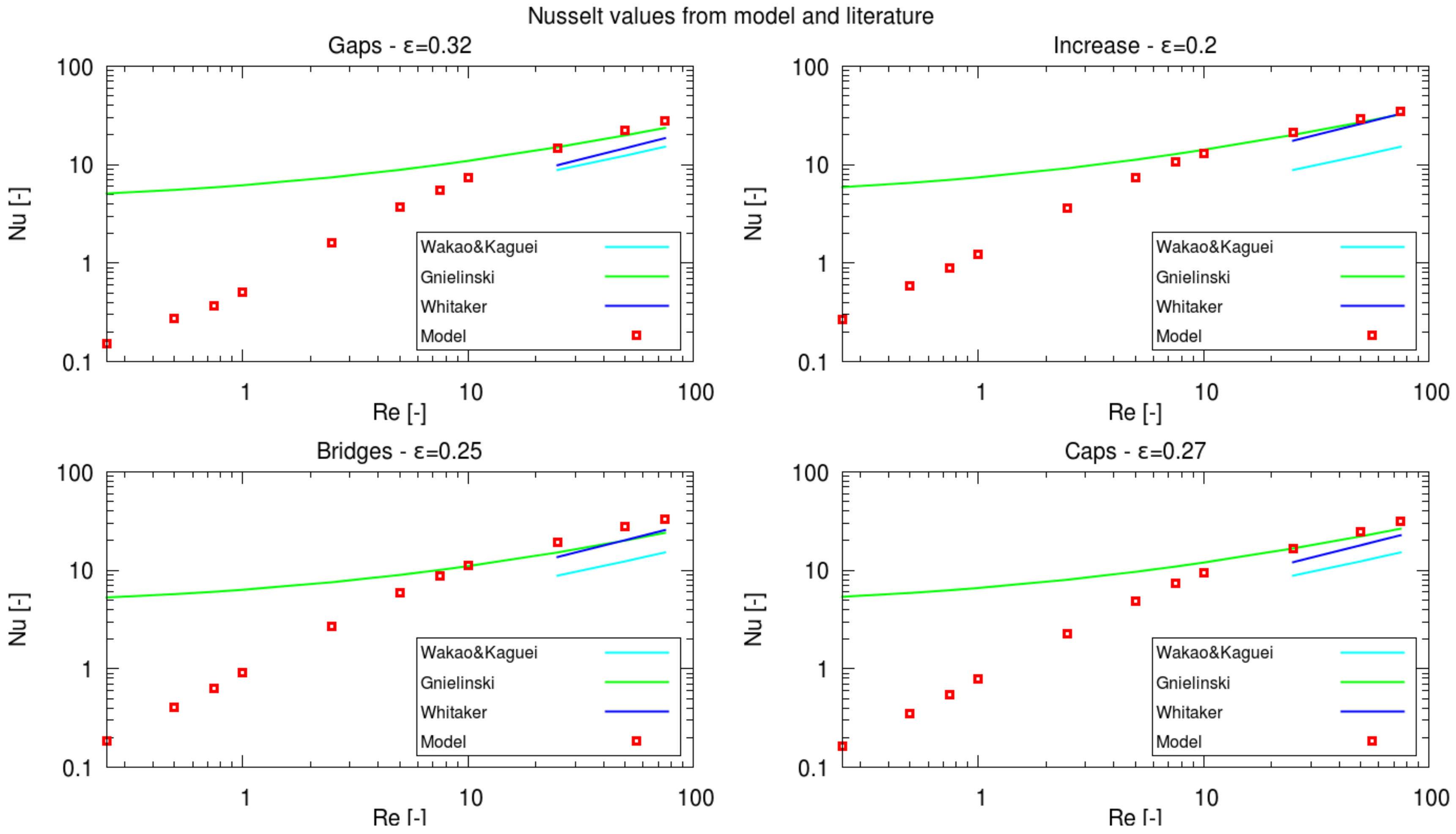

Figure 4.10: Nusselt vs Reynolds for each of the particle contact modelling methods. For $Re > 20$, the rate of heat transfer in the increase and caps geometries is comparable to what was found in the research of the Whitaker and Gnielinski. The gaps method is third best, while the bridges method has the largest deviation.

In figure 4.10 the Nusselt numbers for the four geometries are plotted. All particle contact modelling methods share the trait that the heat transfer is underestimated for low Reynolds numbers compared to the Gnielinski relation. The increase method appears to be producing results that are the closest to the correlations from literature. Also Whitaker's relation comes in close vicinity of this works results. A zoomed-in view of the higher Reynolds region for the increase geometry is shown in figure 4.11. With this closer look it can be seen that the for $Re \geq 10$, Gnielinski's correlation gives a satisfying match with the numerical data. The relative error remains within 9% of Gnielinski's values, which is remarkable, since Gnielinski developed his relation to also be valid for up to $Re/\epsilon \approx 10^7$. There is a slight overestimation of convective heat transfer after $Re \approx 10$, compared to both the Gnielinski and Whitaker relations.

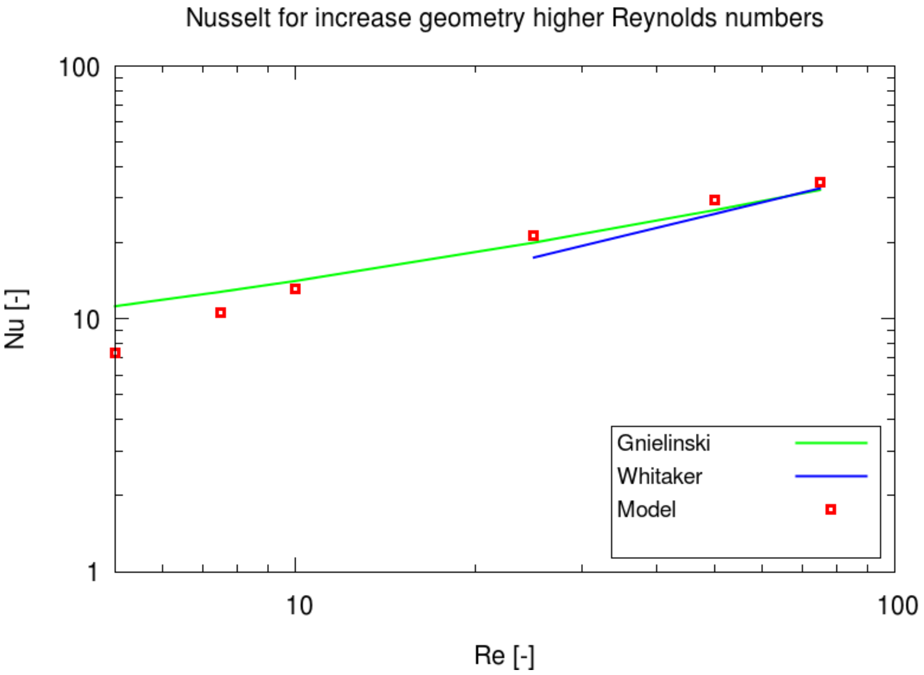

Figure 4.11: Nusselt for the increase geometry in the higher Reynolds region. Gnielinski's equation gives a good match for $10 \leq Re < 75$.

The data from the other geometries are less in concordance with any of the empirical correlations. Among them, the caps method gives the best performance, followed by the gaps geometry. The bridge method is, similar to the pressure drop study, the worst. A general trend can be deduced: up to $Re \approx 20$ the heat transfer is underestimated by the model (when compared to Gnielinski), above this region the heat transfer is slightly overestimated (compared to any of the Nusselt relations).

Combining the evaluations of the four methods on pressure drop and heat transfer, it is concluded that the bridging method produces the least comparable results. It is recommended to not use this method. The pressure drop from the caps method was relatively good, but the heat transfer from the increase method performed better. The gaps method predicts pressure drop and heat transfer relatively well.

When using continuum methods to model a packed bed reactor, it is advised to employ the K-C equation to determine the pressure in the bed as function of streamwise coordinate. It is only valid for $Re < 1$, but this is sufficient for heat batteries. In the case that higher Reynolds numbers are used, the Ergun equation can be employed, but the modeller has to bare in mind that the deviation grows rapidly for larger Reynolds numbers. For heat transfer, it is not recommended to use any of the Nusselt relations mentioned in this work (given that $Re < 1$). More research on laminar heat transfer in packed beds is required.

Chapter 5

Conclusions and recommendations

Heat battery models can provide useful insight in the mechanisms that are at play internally. In this thesis, a DNS model was developed in OpenFOAM to simulate the hydration process of a K_2CO_3 packed bed reactor. To this end, use was made of a Representative Elementary Volume (REV). This collection of 32 particles in FCC configuration was used to represent the complete packed bed. In a second study, pressure drop and heat transfer were investigated.

5.1 Conclusions

First, the hydration process was modelled. Air with 26°C and 15mbar water vapour pressure was flown through the REV to investigate the hydration kinetics. The first rows displayed conversion curves typically seen in R_3 reaction models. For particle rows further downstream, the reaction started more gradual and resembled an S-shape: an initial period of the conversion rate ramping up, followed by a period of faster reaction where the bulk of the particle is hydrated and a final period of decreasing reaction rate. The maximum temperature of 64°C according to the phase diagram was not reached and only an increase of 29°C was reported by the probes. The highest maximum fractional conversion rates were found in the first particle row and decreased for particles further from the inlet. However, the maximum of the particle row 7 was higher than that of row 6, which was probably caused by outlet effects.

To study its effect on the hydration kinetics, the inlet water vapour concentration was varied. Two studies were conducted with inlet concentrations of 13.48 and 12mbar of partial pressure. As expected, the lower concentrations resulted in a slower hydration rate. A drop in REV reaction rate average was observed. This drop, while occurring at different moments in time, took place at REV fractional conversion averages of approximately 0.75.

It was shown that while the model produced explicable results, the REV fell short in length. This was deduced from the fact that the progression of conversion of downstream particle rows was still significantly changing, implicating inlet effects were still at play. An REV is designed properly if it can be used to represent any arbitrary location in the bulk of the packed bed and therefore, inlet effects cannot be present (and for the same matter also outlet effects cannot be present). Employing an REV to model the packed bed reactor is partially justified by the observation that a reaction front was formed and the inlet conditions shifted along through the domain. This was derived from the fact that the temperature and concentration logged by the first probe were approaching inlet conditions.

In order to evaluate the micro-scale flow and heat transfer effects, the REV was subjected to two studies: the pressure drop over the REV and the fluid-to-particle convective heat transfer. The effect of the particle-particle contact modelling methods were also investigated. The four methods were: shrinking the particles to create gaps (gaps methods), increasing the particle diameters (increase method), creating inter-particle bridges (bridges method) and capping the particles (caps method). Results were compared to multiple correlations from literature. For the pressure drop over the REV, the model results were compared the Kozeny-Carman (K-C), Ergun and KTA equations. It was concluded that for $Re \leq 1$, the K-C equation could more or less predict the pressure drop, although a slight underestimation of the model was observed in all geometries. For $Re \geq 1$, the model results were closer to Ergun than to KTA. Between the geometries, it was the caps method that produced the closest results. This was determined by calculating the relative errors to the K-C and Ergun equations. The gaps and increase methods were the second and third best choices, respectively. The bridges method produced the least comparable results by far. This pushed to investigate what would happen if a geometry would be used that resembled the actual situation (touching particles) more closely. The caps and gaps methods, although having the lowest relative errors, could not be used for this: reducing the capping radius or reducing the particle shrinkage would result in a geometry that could not be properly meshed. Therefore, the increase geometry was selected. The increase of particle diameter was reduced from 3% to 1%. Confirming the hypothesis, a significantly smaller average relative error was found: while at 3% increase the relative error to the K-C and Ergun equations were both 0.232, at 1% increase the relative erros were reduced to 0.149 and 0.199. Furthermore, an attempt was made to fit the equation proposed by Ahmadi to the numerical data. Using the non-linear least squares method, a fit with low R^2 could be found for the four geometries. However, the relative error at low Reynolds numbers was high. This was explained by the fact that in their work, Ahmadi fitted over Reynolds numbers up to 1250000 and chose to not include a term to account for the viscous effects. The proposed equation was therefore not deemed useful for Reynolds ranges comparable to what was used in this thesis.

Also for the convective heat transfer the numerical results were compared to relations from literature. Several Nusselt correlations -both porosity dependent and porosity independent- were used to compare the ease of heat transfer in the REV at low Reynolds numbers. For $Re < 10$ none of the correlations gave comparable results and the Nusselt numbers from the model were significantly lower than the Nusselt numbers from the Gnielinski relation. However, a good match was found for $Re \geq 10$ in Gnielinski's relation (also Whitaker's relation was close in this range). Comparing the particle contact modelling methods, it was the increase method that yielded the results closest to the equations from literature, followed by the caps, gaps and finally the bridges method.

In the hydration study a flow with $Re \approx 0.6$ was used in combination with the gaps method. Assuming that the Gnielinski correlation is correct, the rate of convective heat transfer was heavily underestimated by the model. However, since this correlation was proposed for up to $Re/\epsilon = 1.1 \cdot 10^7$, accuracy is probably lost for low Reynolds numbers.

5.2 Recommendations

Regarding the REV design, it is recommended that its length is increased to at least three times the current size. This is required to avoid the presence of inlet effects. For flows with low Péclet numbers where temperature and water vapour can diffuse against the direction of flow, an even longer REV may be required because in that case, outlet effects have to be taken into account as well. To fully develop the thermal and concentration boundary layers at the first particle rows, inlet profiles should be used at the inlet. Additionally, the model can be run with different particle configurations (BCC, SC, random packing). Finally, it is advised that for further REV modelling where a particle-particle contact method is used, the increase method should be used.

To better understand viscous effects and heat and mass transfer in packed beds, it is recommended that experiments are carried out to study local pressure drop and heat transfer. By investigating these mechanisms on millimeter scale instead of averaging over the packed bed reactor, better insight can be obtained on the formation of viscous, thermal and concentration boundary layers. The results of these experiments can then be compared to the results from models similar to those described in this thesis. Regarding the choice of contact modelling method, it is advised to use the increase method in future work. It had the best performance regarding heat transfer. Although it did not capture the pressure drop as good as the caps and gaps methods, pressure drop does not play a role in the hydration kinetics (given a fixed flow velocity). It is therefore not of influence on the hydration process.

However, since it has also become clear that none of the contact modelling method produced unambiguously good results, a different approach may be necessary. It is therefore recommended that for future DNS models of packed beds where spherical particles are involved, the Immersed Boundary Method (IBM) is utilized to discretize the geometry. In doing so, no contact modelling method has to be employed which is expected to yield results that are better comparable to experiments. Simultaneously, the mesh quality will improve, which is expected to drastically reduce the required computational effort and improve accuracy.

If investigation of macro-scale effects are the goal of study, it is not advised to use DNS. Using continuum methods is several times faster while results can be in good agreement with experimental results, as was shown in [12]. Modellers who wish to employ continuum methods in their packed bed reactor models, are advised to use the K-C equation to calculate the pressure as a function of streamwise coordinate. It gives acceptable results for $Re \leq 1$. Unfortunately, no proper Nusselt correlation is known for this region, and thus the convective heat transfer can not yet be approximated. It is recommended to research the rate of convective heat transfer in packed beds for this low Reynolds number region.

Bibliography

[1] Joost Gerdes, Sjoerd Marbus, and Martijn Boelhouwer. Energietrends 2016. Technical report, ECN, 2016. vii, 1

[2] PAJ Donkers, LC Sögütoglu, HP Huinink, HR Fischer, and OCG Adan. A review of salt hydrates for seasonal heat storage in domestic applications. *Applied energy*, 199:45–68, 2017. vii, vii, 3, 4, 5, 35

[3] Herbert Zondag. Reader 4em50 thermal energy storage 2017-2018. vii, 2, 4

[4] Apiano F Morais, Hansjoerg Seybold, Hans J Herrmann, and José S Andrade Jr. Non-newtonian fluid flow through three-dimensional disordered porous media. *Physical review letters*, 103(19):194502, 2009. vii, 8

[5] Anthony G Dixon, Michiel Nijemeisland, and E Hugh Stitt. Systematic mesh development for 3d cfd simulation of fixed beds: Contact points study. *Computers & Chemical Engineering*, 48:135–153, 2013. vii, 9, 10

[6] Shuiquan Lan, Herbert Zondag, Anton van Steenhoven, and Camilo Rindt. Kinetic study of the dehydration reaction of lithium sulfate monohydrate crystals using microscopy and modeling. *Thermochimica acta*, 621:44–55, 2015. vii, 6, 19, 21, 22

[7] Robert Arslanbekov, Vladimir Kolobov, and A Frolova. Analysis of compressible viscous flow solvers with adaptive cartesian mesh. In *20th AIAA Computational Fluid Dynamics Conference*, page 3381, 2011. viii, 28

[8] NL Agentschap. warmte en koude in nederland. retrieved january 7, 2015, 2013. 1

[9] . Study on open and closed chemical thermal energy storage technology with low-regeneration temperature. 2014. 3

[10] Benoit Michel, Pierre Neveu, and Nathalie Mazet. Comparison of closed and open thermochemical processes, for long-term thermal energy storage applications. *Energy*, 72:702–716, 2014. 3

[11] E.W. Washburn. Knovel, 1926 - 1930;2003. 4

[12] M Gaeini. Thermochemical seasonal heat storage for the built environment: a multi-scale investigation. 2017. 5, 23, 41, 59

[13] Loïc Favergeon, Jacques Morandini, Michèle Pijolat, and Michel Soustelle. A general approach for kinetic modeling of solid-gas reactions at reactor scale: application to kaolinite dehydroxylation. *Oil & Gas Science and Technology–Revue dIFP Energies nouvelles*, 68(6):1039–1048, 2013. 5, 21

[14] Armand Fopah-Lele, Frédéric Kuznik, Thomas Osterland, and Wolfgang KL Ruck. Thermal synthesis of a thermochemical heat storage with heat exchanger optimization. *Applied Thermal Engineering*, 101:669–677, 2016. 5

[15] Shuiquan Lan. *Grain-scale analysis of thermochemical heat storage materials.* PhD thesis, Technische Universiteit Eindhoven, 2016. 5, 25

[16] Per EC Burström, Vilnis Frishfelds, Anna-Lena Ljung, T Staffan Lundström, and B Daniel Marjavaara. Modelling heat transfer during flow through a random packed bed of spheres. *Heat and Mass Transfer*, 54(4):1225–1245, 2018. 5

[17] RE Hayes, A Afacan, B Boulanger, and AV Shenoy. Modelling the flow of power law fluids in a packed bed using a volume-averaged equation of motion. *Transport in porous media*, 23(2):175–196, 1996. 6

[18] Loïc Favergeon, Michèle Pijolat, Françoise Valdivieso, and Céline Helbert. Experimental study and monte-carlo simulation of the nucleation and growth processes during the dehydration of li 2 so 4· h 2 o single crystals. *Physical Chemistry Chemical Physics*, 7(21):3723–3727, 2005. 6

[19] Shuiquan Lan, Mohammadreza Gaeini, Herbert Zondag, Anton van Steenhoven, and Camilo Rindt. Direct numerical simulation of the thermal dehydration reaction in a tga experiment. *Applied Thermal Engineering*, 128:1175–1185, 2018. 6, 22, 35, 41

[20] DA Deshpande, KR Ghormare, ND Deshpande, and AV Tankhiwale. Dehydration of crystalline k2co3· 1.5 h2o. *Thermochimica Acta*, 66(1-3):255–265, 1993. 6

[21] Armand Fopah Lele, Frédéric Kuznik, Holger U Rammelberg, Thomas Schmidt, and Wolfgang KL Ruck. Thermal decomposition kinetic of salt hydrates for heat storage systems. *Applied energy*, 154:447–458, 2015. 6, 19

[22] Ganesh Balasubramanian, Mehdi Ghommem, Muhammad R Hajj, William P Wong, Jennifer A Tomlin, and Ishwar K Puri. Modeling of thermochemical energy storage by salt hydrates. *International Journal of Heat and Mass Transfer*, 53(25-26):5700–5706, 2010. 6

[23] G David Scott. Packing of spheres: packing of equal spheres. *Nature*, 188(4754):908, 1960. 9

[24] Xi-zhong An. Densification of the packing structure under vibrations. *International Journal of Minerals, Metallurgy, and Materials*, 20(5):499–503, 2013. 9

[25] HPA Calis, JPBC Nijenhuis, BC Paikert, FM Dautzenberg, and CM Van Den Bleek. Cfd modelling and experimental validation of pressure drop and flow profile in a novel structured catalytic reactor packing. *Chemical Engineering Science*, 56(4):1713–1720, 2001. 9

[26] Michiel Nijemeisland and Anthony G Dixon. Comparison of cfd simulations to experiment for convective heat transfer in a gas–solid fixed bed. *Chemical Engineering Journal*, 82(1-3):231–246, 2001. 9, 25

[27] SJP Romkes, FM Dautzenberg, CM Van den Bleek, and HPA Calis. Cfd modelling and experimental validation of particle-to-fluid mass and heat transfer in a packed bed at very low channel to particle diameter ratio. *Chemical Engineering Journal*, 96(1-3):3–13, 2003. 9

[28] Theodoros Atmakidis and Eugeny Y Kenig. Cfd-based analysis of the wall effect on the pressure drop in packed beds with moderate tube/particle diameter ratios in the laminar flow regime. *Chemical Engineering Journal*, 155(1-2):404–410, 2009. 9

[29] WE Ranz and WR Marshall. Evaporation from droplets. *Chemical Engineering Progress*, 48(3):141–146, 1952. 11, 52, 71, 84

[30] N Wakao and T Funazkri. Effect of fluid dispersion coefficients on particle-to-fluid mass transfer coefficients in packed beds: correlation of sherwood numbers. *Chemical Engineering Science*, 33(10):1375–1384, 1978. 11

[31] N Wakao, S Kaguei, and T Funazkri. Effect of fluid dispersion coefficients on particle-to-fluid heat transfer coefficients in packed beds: correlation of nusselt numbers. *Chemical engineering science*, 34(3):325–336, 1979. 12, 53

[32] Stephen Whitaker. Forced convection heat transfer correlations for flow in pipes, past flat plates, single cylinders, single spheres, and for flow in packed beds and tube bundles. *AIChE Journal*, 18(2):361–371, 1972. 12, 53

[33] Xianke Meng, Zhongning Sun, and Guangzhan Xu. Single-phase convection heat transfer characteristics of pebble-bed channels with internal heat generation. *Nuclear Engineering and Design*, 252:121–127, 2012. 12

[34] Nuclear Safety Standards Commission et al. Reactor core design of high temperature gas-cooled reactors: Heat transfer spherical fuel elements, kta 3102.2 part 2. 1983. 12

[35] V Gnielinski. Gleichungen zur berechnung des wärme-und stoffaustausches in durchströmten ruhenden kugelschüttungen bei mittleren und großen pecletzahlen. *Verfahrenstechnik*, 12(6):363–367, 1978. 12, 53

[36] E Achenbach. Heat and flow characteristics of packed beds. *Experimental thermal and fluid science*, 10(1):17–27, 1995. 13

[37] YASAR Demirel, BA Abu-Al-Saud, HH Al-Ali, and Y Makkawi. Packing size and shape effects on forced convection in large rectangular packed ducts with asymmetric heating. *International journal of heat and mass transfer*, 42(17):3267–3277, 1999. 13

[38] H Tavassoli, EAJF Peters, and JAM Kuipers. Direct numerical simulation of fluid–particle heat transfer in fixed random arrays of non-spherical particles. *Chemical engineering science*, 129:42–48, 2015. 13

[39] Arpit Singhal, Schalk Cloete, Stefan Radl, R Quinta-Ferreira, and S Amini. Multiscale modelling of heat transfer from arrays of spherical particles. In *Proceedings of the 9th International Conference on Multiphase Flow (ICMF), Firenze, Italy*, pages 22–27, 2016. 13

[40] G Srinivasa Rao, KV Sharma, SP Chary, RA Bakar, MM Rahman, K Kadirgama, and MM Noor. Experimental study on heat transfer coefficient and friction factor of al2o3 nanofluid in a packed bed column. *Journal of Mechanical Engineering and Sciences*, 1(1):1–15, 2011. 13

[41] Kevin J Albrecht and Clifford K Ho. High-temperature flow testing and heat transfer for a moving packed-bed particle/sco2 heat exchanger. In *AIP Conference Proceedings*, volume 2033, page 040003. AIP Publishing, 2018. 13

[42] Kevin J Albrecht and Clifford K Ho. Heat transfer models of moving packed-bed particle-to-sco2 heat exchangers. *Journal of Solar Energy Engineering*, 141(3):031006, 2019. 13

[43] Junlin Chen, Xunfeng Li, and Xiulan Huai. Experimental study on the heat transfer of gas with coagulative particles flowing through a packed granular bed filter. *Applied Thermal Engineering*, 141:906–912, 2018. 13

[44] AJ Dave, K Sun, and L Hu. Numerical assessment of packed-bed heat transfer correlations for molten salt. *Annals of Nuclear Energy*, 136:107002, 2020. 13, 52

[45] AH Ahmadi Motlagh and SH Hashemabadi. Cfd based evaluation of heat transfer coefficient from cylindrical particles. *International Communications in Heat and Mass Transfer*, 35(5):674–680, 2008. 13

[46] A Žukauskas. Heat transfer from tubes in crossflow. In *Advances in heat transfer*, volume 8, pages 93–160. Elsevier, 1972. 14

[47] Stephen Whitaker. *Elementary Heat Transfer Analysis.* 01 1976. 14

[48] Saurish Das, Niels G Deen, and JAM Kuipers. A dns study of flow and heat transfer through slender fixed-bed reactors randomly packed with spherical particles. *Chemical Engineering Science*, 160:1–19, 2017. 14, 17, 18

[49] Sakae Yagi and Noriaki Wakao. Heat and mass transfer from wall to fluid in packed beds. *AIChE Journal*, 5(1):79–85, 1959. 14

[50] Maasoud Kaviany. *Principles of heat transfer in porous media.* Springer Science & Business Media, 2012. 15

[51] John Hadlett Harker, John Rayner Backhurst, and JF Richardson. *Chemical Engineering Volume 2: Particle Technology and Separation Processes.* Elsevier Science, 2002. 17

[52] Philip Crosbie Carman. Flow of gases through porous media. 1956. 17

[53] Sabri Ergun. Fluid flow through packed columns. *Chem. Eng. Prog.*, 48:89–94, 1952. 17, 46

[54] IF Macdonald, MS El-Sayed, K Mow, and FAL Dullien. Flow through porous media-the ergun equation revisited. *Industrial & Engineering Chemistry Fundamentals*, 18(3):199–208, 1979. 17, 18

[55] J Kozeny. Ueber kapillare leitung des wassers im boden, wien, akad. *Wiss*, 136:271, 1927. 18, 46

[56] Philip Crosbie Carman. Fluid flow through granular beds. *Trans. Inst. Chem. Eng.*, 15:150–166, 1937. 18, 46

[57] Sicherheitstechnische Regel des Kerntechnischen Ausschusses. Auslegung der reaktorkerne von gasgekuhlten hochtemperaturreaktoren, 1981. 18, 46

[58] Soroush Ahmadi and Farhang Sefidvash. Study of pressure drop in fixed bed reactor using a computational fluid dynamics (cfd) code. *ChemEngineering*, 2(2):14, 2018. 18, 50

[59] Michael Giese. *Strömung in porösen Medien unter Berücksichtigung effektiver Viskositäten.* na, 1998. 18

[60] CCM Rindt and SV Gaastra-Nedea. Modeling thermochemical reactions in thermal energy storage systems. In *Advances in Thermal Energy Storage Systems*, pages 375–415. Elsevier, 2015. 18

[61] Leslie Glasser. Thermodynamics of inorganic hydration and of humidity control, with an extensive database of salt hydrate pairs. *Journal of Chemical & Engineering Data*, 59(2):526–530, 2014. 19

[62] Kurt L Mampel. Zeitumsatzformeln für heterogene reaktionen an phasengrenzen fester körper 2. die zeitumsatzformeln für ein pulver ans kugelförmigen teilchen. *Zeitschrift für Physikalische Chemie*, 187(1):235–249, 1940. 21

[63] E Gleuckauf and JI Coates. The influence of incomplete equilibrium on the front boundary of chromatograms and the effectiveness of separation. *J Chem Soc*, 1315:e21, 1947. 22

[64] Douglas M Ruthven. *Principles of adsorption and adsorption processes.* John Wiley & Sons, 1984. 22

[65] Engineering toolbox, (2018). *Air - Diffusion Coefficients of Gases in Excess of Air.* `https://www.engineeringtoolbox.com/air-diffusion-coefficient-gas-mixture-temperature-d_2010.html`. Accessed: 13-09-2019. 35

[66] Elsa Valencia Martinez. Solabcool : a novel adsorption chiller for the built environment. 2013. 35

[67] SA Shaik. Kinetic investigation of k2co3 using thermal analysis techniques and modelling of energy-padstm. Master's thesis, Eindhoven University of Technology, 2018. 35

[68] Electronics cooling. `https://www.electronics-cooling.com/2003/11/the-thermal-conductivity-of-moist-air/`. Accessed: 13-09-2019. 35

[69] Mahdi Zare and Seyed Hassan Hashemabadi. Cfd simulation and experimental validation of tortuosity effects on pellet-fluid heat transfer of regularly stacked multi-lobe particles. *Chemical Engineering Journal*, 361:1543–1556, 2019. 42

[70] Bernard Atkinson, MP Brocklebank, CCH Card, and JM Smith. Low reynolds number developing flows. *AIChE Journal*, 15(4):548–553, 1969. 68

[71] Ulf Herrmann and David W Kearney. Survey of thermal energy storage for parabolic trough power plants. *Journal of solar energy engineering*, 124(2):145–152, 2002. 84

[72] Souad Messai, Mohammed El Ganaoui, Jalila Sghaier, and Ali Belghith. Experimental study of the convective heat transfer coefficient in a packed bed at low reynolds numbers. *Thermal Science*, 18(2):443–450, 2014. 84

Appendix A

Validation of the solver

The OpenFOAM solver is validated through the comparison of results from two cases of which the analytical solutions are known.

A.1 Flow velocity profile

A relatively simple method to (partially) validate the solving of the flow field is by modelling Poiseuille flow. To this end, OpenFOAM is tasked with finding a steady-state solution for laminar flow through a pipe. The analytical solution of the radial velocity profile (function of radius r) is described by the Hagen-Poiseuille equation:

$$u(r) = -\frac{R^2}{4\mu}\frac{\partial p}{\partial x}\left(1 - \frac{r^2}{R^2}\right), \tag{A.1}$$

where R [m] is the pipe diameter, μ [Pa·s] is the dynamic viscosityand $\frac{\partial p}{\partial x}$ [Pa/m] is the partial derivative of the pressure p to x. As the inlet pressure (the outlet pressure is set to 0) is not prescribed an equation is required that couples the mean velocity (= is the prescribed inlet velocity) to the velocity profile. The average velocity V_{avg} [m/s] is given by the following equation:

$$V_{avg} = \frac{2}{R^2}\int_0^R u(r) r dr \tag{A.2}$$

By substituting equation A.1 into equation A.2 an new equation for the mean velocity is obtained:

$$V_{avg} = -\frac{R^2}{8\mu}\frac{\partial p}{\partial x} \tag{A.3}$$

Rearranging for $\frac{\partial p}{\partial x}$ and substituting back into equation A.1 yields

$$u(r) = 2V_{avg}\left(1 - \frac{r^2}{R^2}\right) \tag{A.4}$$

The model used in this validation is a straight tube with diameter $D = 0.01$ [m]. A flow with $Re = 1$ is prescribed at the inlet. According to the definition of the Reynolds number for a pipe

$$Re = \frac{uD}{\nu}, \tag{A.5}$$

this corresponds to a velocity of 0.00174 [m/s] (using a kinematic viscosity $\nu = 1.74 \cdot 10^{-5}$). Dirichlet conditions are prescribed at the tube wall. A zero-gradient Neumann condition is used at the outlet. For the pressure, zero-gradient conditions are applied to the wall and inlet, while the outlet pressure is set to a constant 0. The simpleFoam solver is employed for this case. According to Atkinson et al. [70] the entrance length ($0.99u_0$) for low-Reynolds pipe flow is

$$L_{entrance} = (0.59 + 0.056Re)D = 6.5 \text{ [mm]} \tag{A.6}$$

At this distance from the inlet, the velocity should be 99% of its developed value. In figure A.1, the velocity on the centreline is plotted. At x=6.5 [mm], u=3.277 [mm/s], which is 99.4% of its developed velocity.

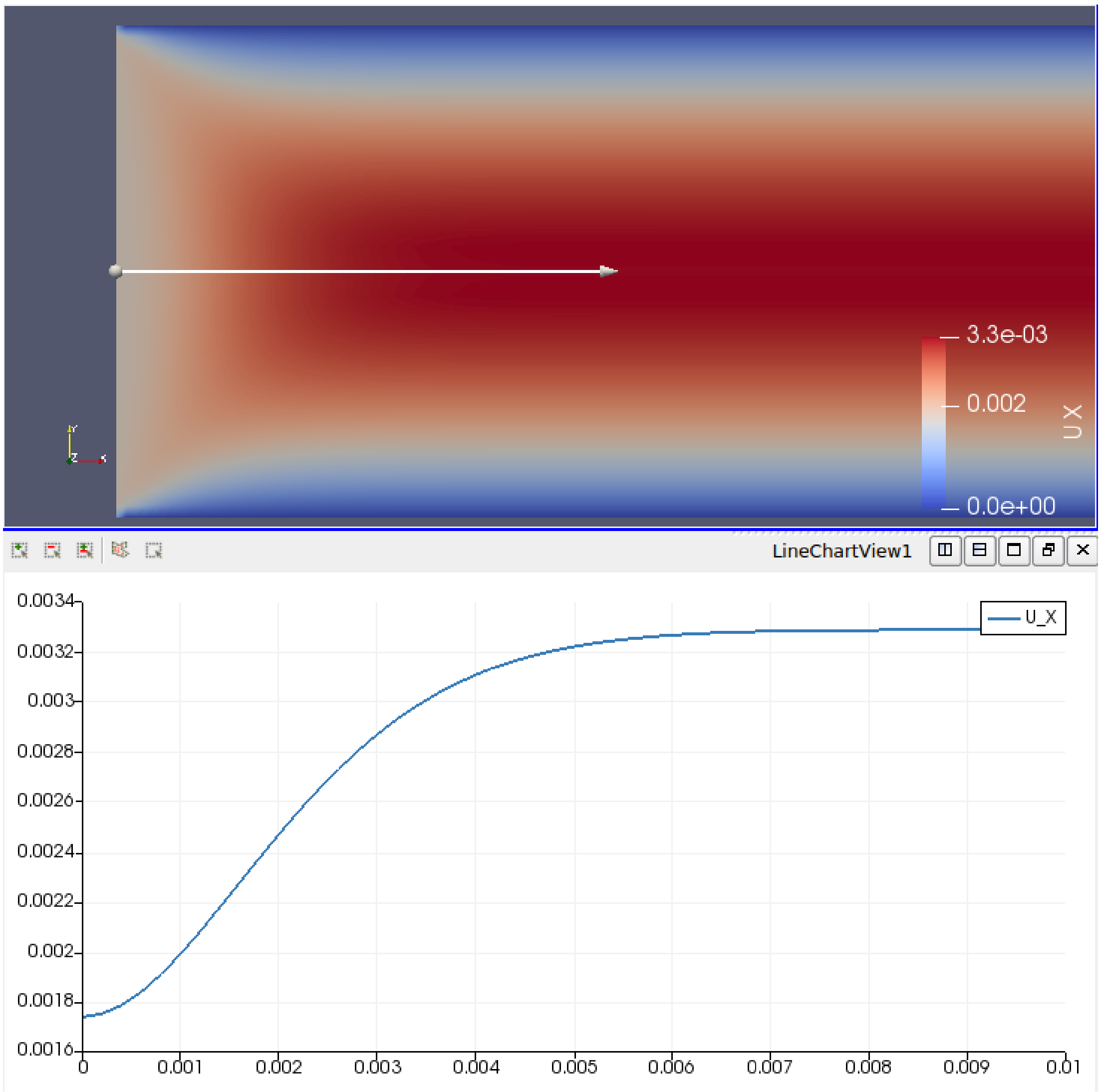

Figure A.1: Top: solution of the velocity field as solved by OpenFOAM. Fluid enters at the left. Bottom: the axial velocity along the white arrow is plotted in the graph. ($u = 0.00174$ [m/s], $D = 0.01$ [m], $\nu = 1.74 \cdot 10^{-5}$ [m^2/s])

Several different mesh methods can be used and their degree of accuracy will vary. Differentiating between structured and unstructured mesh, four meshing approaches are evaluated: structured

(8 radial elements), structured refined x2 (16 radial elements), structured refined x3 (24 radial elements) and unstructured, as shown in figure A.2. Velocity gradient are higher at the boundary and therefore a scale factor of 0.2 is applied, so that the elements are thicker near the pipe center.

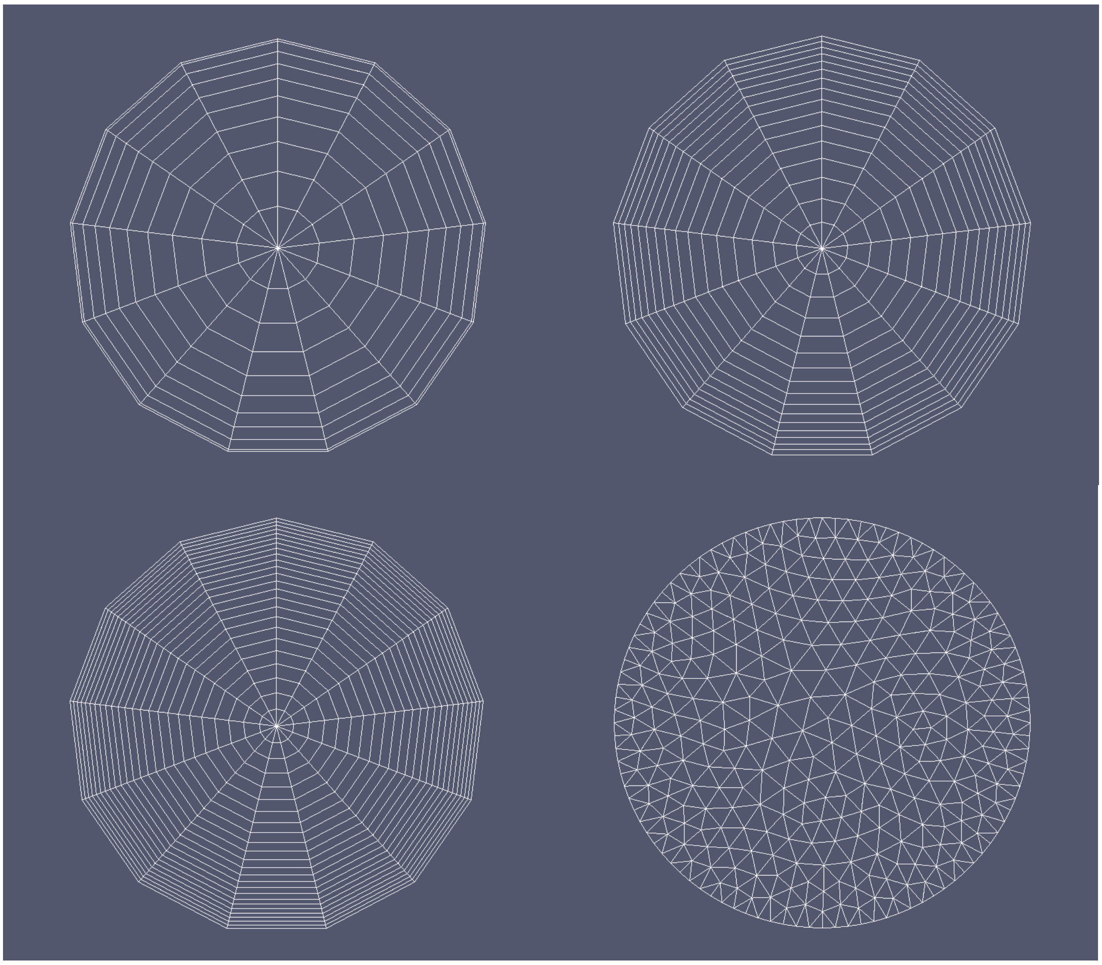

Figure A.2: The four different meshes used. Clockwise, starting from top left: standard, refined x2, unstructured, refined x3.

The resulting velocity profiles in radial direction, evaluated at $L_{entrance}$, are shown in figure A.3. It must be noted that the fully developed analytical solution is plotted. Therefore, the numerical solutions has a slightly lower velocity. The axial velocity near the wall appears to be predicted correctly, compared to the analytical solution. To evaluate the profiles at the center, figure A.4 provides a magnified image. The unstructured mesh gives relatively accurate results. As expected, the finest mesh results in the most accurate solution among the structured meshes. The velocity profile of all meshes diverges from the analytical solution as the radial coordinate approaches zero.

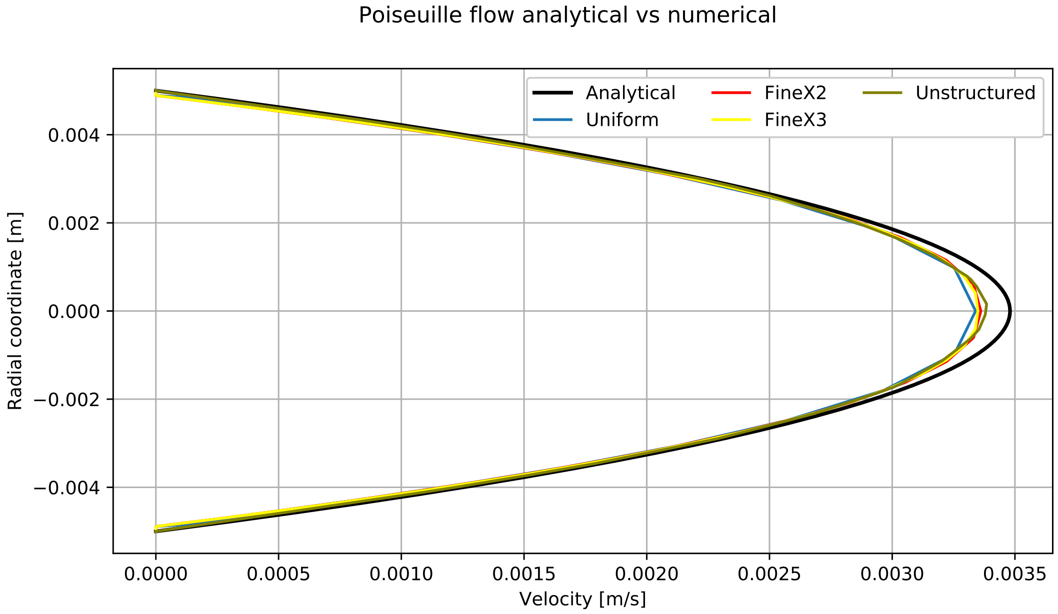

Figure A.3: The flow velocity profiles of the different meshes, compared to the analytical solution.

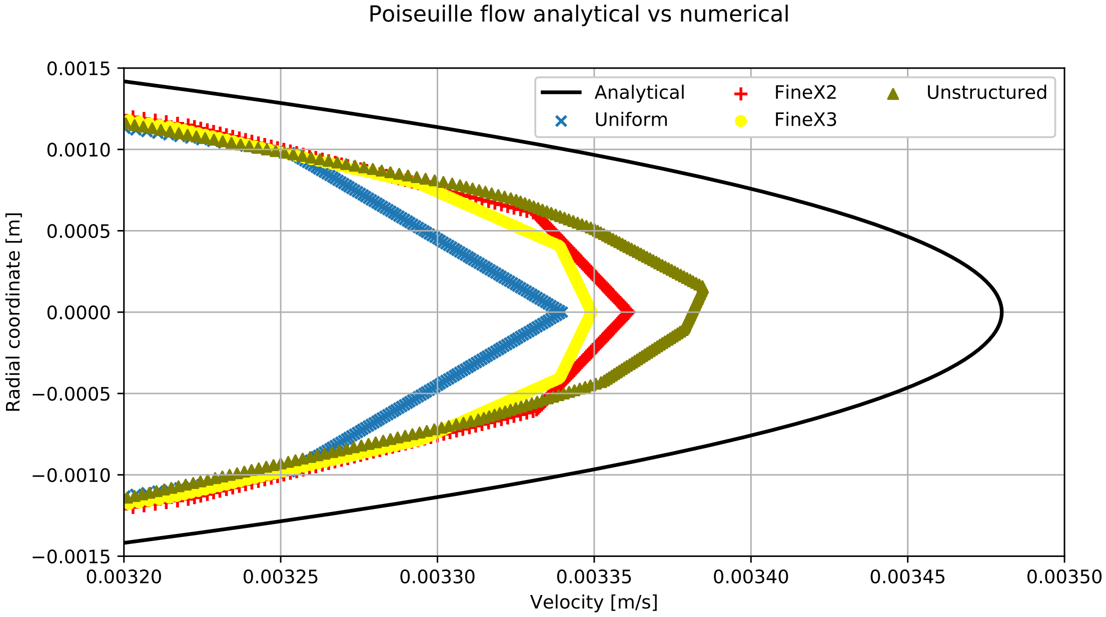

Figure A.4: Velocity profiles magnified at the tube center.

A.2 Heat transfer

A second important mechanism in this work is fluid-solid heat transfer. A temperature difference between the particles and the surrounding gas drives a heat flux through the particle surfaces. To validate this mechanism a single particle is considered, centered in a tube.

Due to the Biot number ($= hL/k \approx 0.1$) being significantly smaller than 1 (see appendix C), the lumped system assumption can be made. A non-dimensional parameter Θ for the temperature is introduced which contains the particle temperature T, the free stream temperature T_∞ and the initial particle temperature T_i:

$$\Theta = \frac{T_i - T_\infty}{T - T_\infty} \tag{A.7}$$

The analytical solution for the temperature evolution over time for a spherical particle is

$$\Theta(t) = \exp\left(-\frac{hA}{\rho_s V c_{p,s}} t\right) \tag{A.8}$$

The particle surface A [m^2], particle volume V [m^3], particle density ρ_s [kg/m^3] and the particle material specific heat $c_{p,s}$ [J/kgK] are known. The convective heat transfer coefficient h [W/m^{2}K]does not have a constant value, but depends on several system parameters:

$$h = \frac{Nu_d k_f}{d_p}, \tag{A.9}$$

with k_f [W/mK] the thermal conductivity of air and d_p [m] the particle diameter. According to Ranz and Marshall [29] the Nusselt number for a sphere in laminar fluid is dependent on the Reynolds and Prandtl numbers:

$$Nu_d = 2 + 0.6 Re_d^{1/2} Pr^{1/3} \tag{A.10}$$

$$Re_d = \frac{\rho_f u d_p}{\mu} \tag{A.11}$$

$$Pr = \frac{\mu c_{p,f}}{k_f}, \tag{A.12}$$

where ρ_f [kg/m^3] is the air density, u [m/s] is the free stream velocity, μ [Pa·s] is the dynamic viscosity of air and $c_{p,f}$ [J/kgK] is the specific heat of air. Values of the constants mentioned above are listed in table A.1.

The first term on the RHS of equation 2.26 is used to calculate the energy transfer between particle and ambient. This would make the energy balance of a particle as follows:

$$\frac{\partial T_p}{\partial t} = \frac{k_f A}{\rho_s c_{p,s} V} \overline{\frac{\partial T}{\partial n}}. \tag{A.13}$$

This approach should yield a particle temperature progression over time similar to equation A.7. To this end, a particle in a tube is modeled, where laminar, hotter air is flown through. Three meshes are generated which can be seen in figure A.5: standard mesh, refined mesh and refined mesh with boundary layer. This boundary layer mesh has a thickness of 5mm.

Table A.1: Constants used in the validation. Several constants are temperature dependent, but are evaluated at the mean temperature of T_i and T_∞.

Symbol	Description	Value
T_i	Initial particle temperature	370 [K]
T_∞	Free stream temperature	400 [K]
u	Free stream velocity	0.5 [m/s]
d	Particle diameter	0.001 [m]
$c_{p,s}$	Specific heat of particle material	1180.8 [J/kgK]
ρ_s	Density of particle material	2060.0 [kg/m^{3}K]
$c_{p,f}$	Specific heat of the fluid (air)	1011.0 [J/kgK]
ρ_f	Density of the fluid (air)	0.8977 [kg/m^{3}K]
k_f	Thermal conductivity of the fluid (air)	0.03235 [W/mK]
μ	Dynamic viscosity of the fluid (air)	2.264e-5 [kg/ms]

The numerical results are plotted together with the analytical solution in figure A.6. The standard mesh already yields a rather accurate result. Adding a boundary layer mesh to the refined mesh does not significantly improve the simulation; the fine mesh has sufficient accuracy.

Since it has been established that the fine mesh provides acceptable accuracy, the model can be validated at higher Reynolds numbers. To this end, the simulation is run with $Re = 100, 200$. Results are plotted in figure A.7.

It becomes clear that the temperature deviation from the analytical solution increases for higher Reynolds numbers. However, since the Reynolds numbers in this work are low, this aspect of the model is regarded as validated.

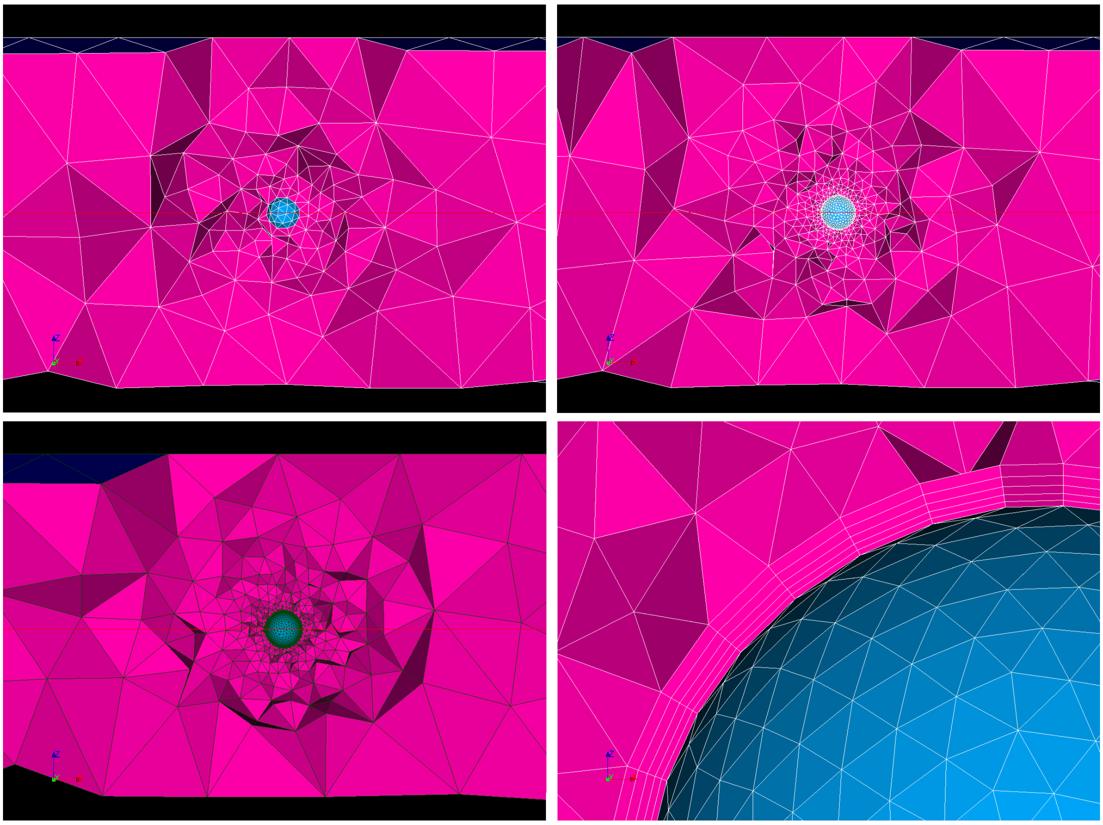

Figure A.5: Different meshes used in the heat transfer validation. Top left: standard mesh (3975 elements). Top right: refined mesh (13514 elements). Bottom left: refined mesh with boundary layer (16836 elements). Bottom right: close-up of the boundary layer mesh.

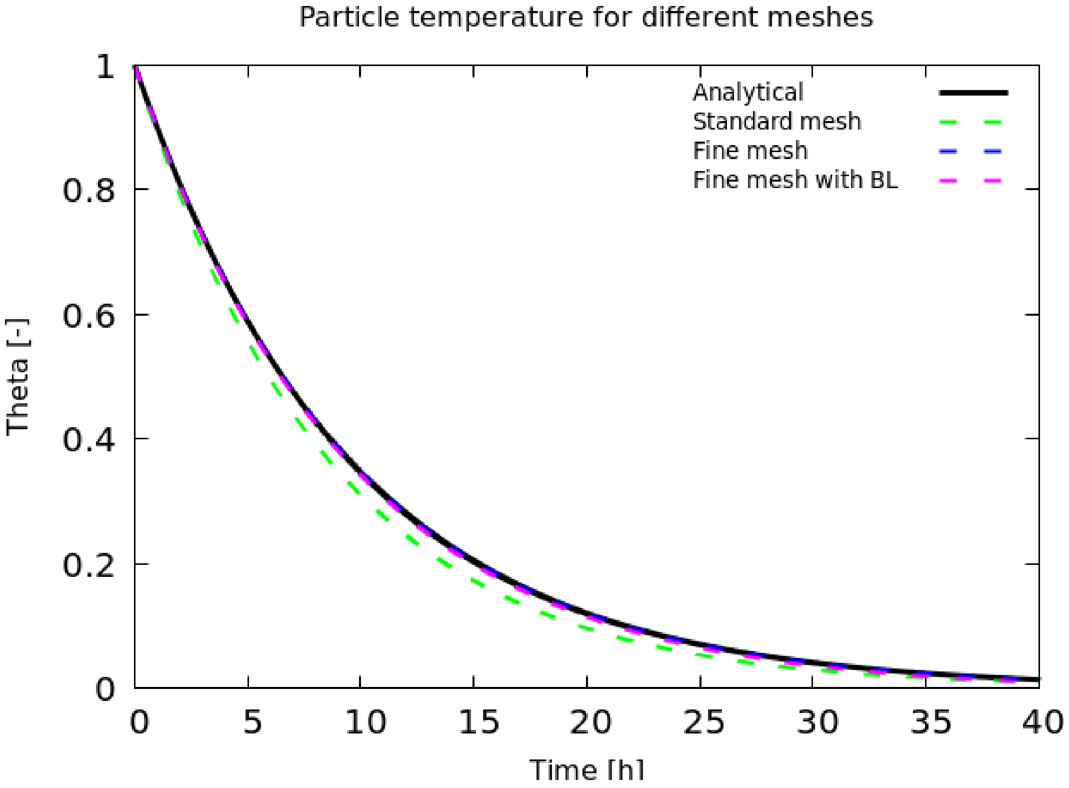

Figure A.6: Particle temperature progression over time for the different meshes.

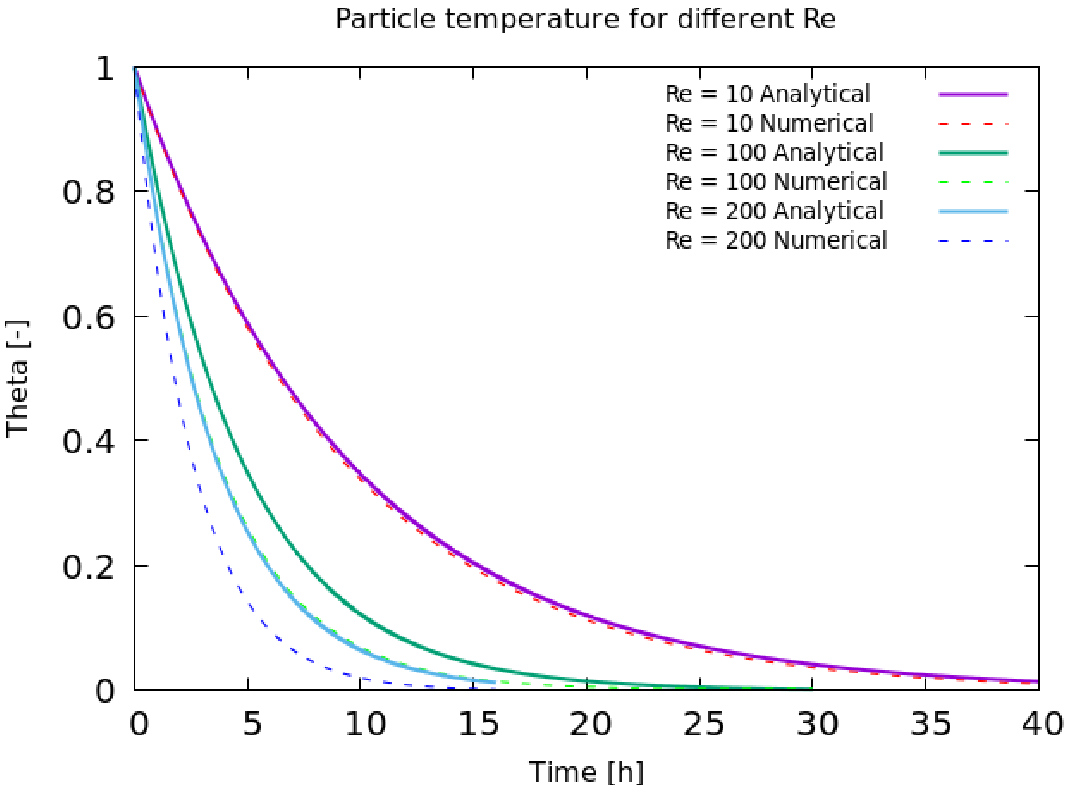

Figure A.7: Particle temperature progression over time for Re=10, 100 and 200, for both the numerical and analytical solutions.

A.3 Conservation of mass and energy

The model must satisfy the laws of conservation. This implies that all mass (or volume due to incompressibility) entering the domain must eventually exit the domain and vice versa. The same condition applies to energy. For this validation the single sphere model of section A.2 is considered again. The mass flux through the outlet is computed by

$$\dot{m}_{water} = c\phi, \tag{A.14}$$

where c [mol/m^3] is the molar concentration of water and ϕ [m^3/s] is the total mass flux. The mass fux through the particle surface is calculated using the normal gradient (transfer at the surface occurs only through diffusion):

$$\dot{m}_{water} = \frac{\partial c}{\partial n} A D_c, \tag{A.15}$$

where A [m^2] is the particle surface area and D_c [m^2/s] is the mass diffusion coefficient of water. Similar equations can be obtained for energy:

$$\dot{q} = (T_{inlet} - T_{outlet})\phi \tag{A.16}$$

$$\dot{q} = \frac{\partial T}{\partial n} A D_T, \tag{A.17}$$

where D_T is the thermal diffusivity. It must be noted that the unit of heat flux in these equations is [Km^3/s] (divide by ρ and $c_{p,f}$ to obtain [J/s])].

As can be seen in figure A.8, the mass flux through the particle surfaces and the mass flux through the outlet appear to be matching. Integrating over time and comparing the total mass fluxes, the water vapour mass flux through the particles surface is 0.02% less than the outlet water vapour mass flux. However, the heat flux through the particle surface is underestimated consistently, which can be clearly seen in figure A.9. A difference of 6% is found. This error perseveres when decreasing the temporal and spatial resolution.

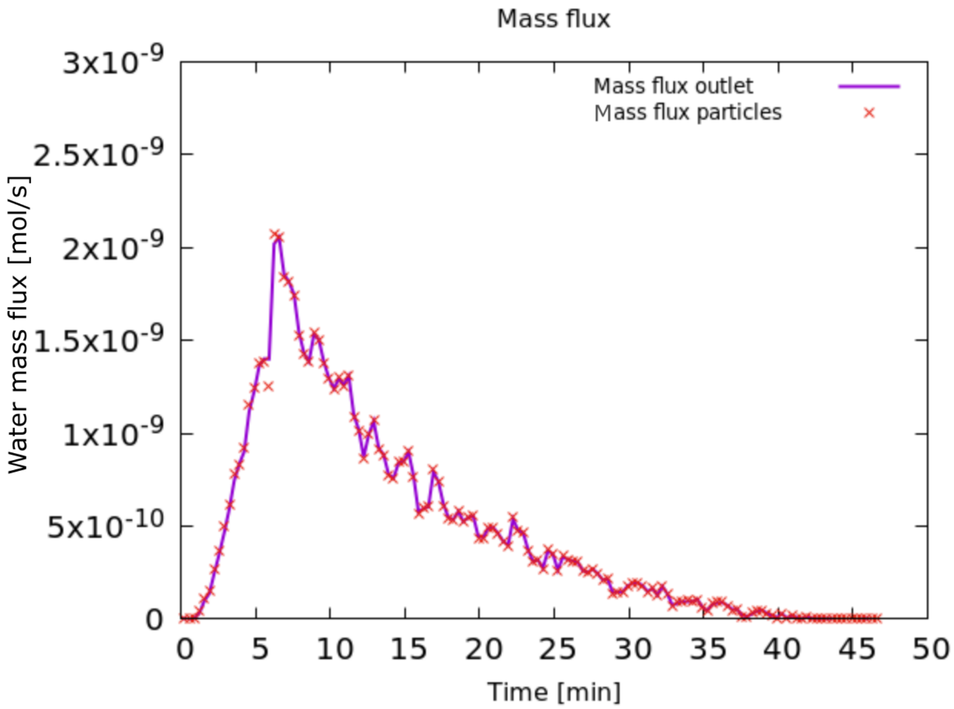

Figure A.8: Mass fluxes through the outlet and the particle surfaces.

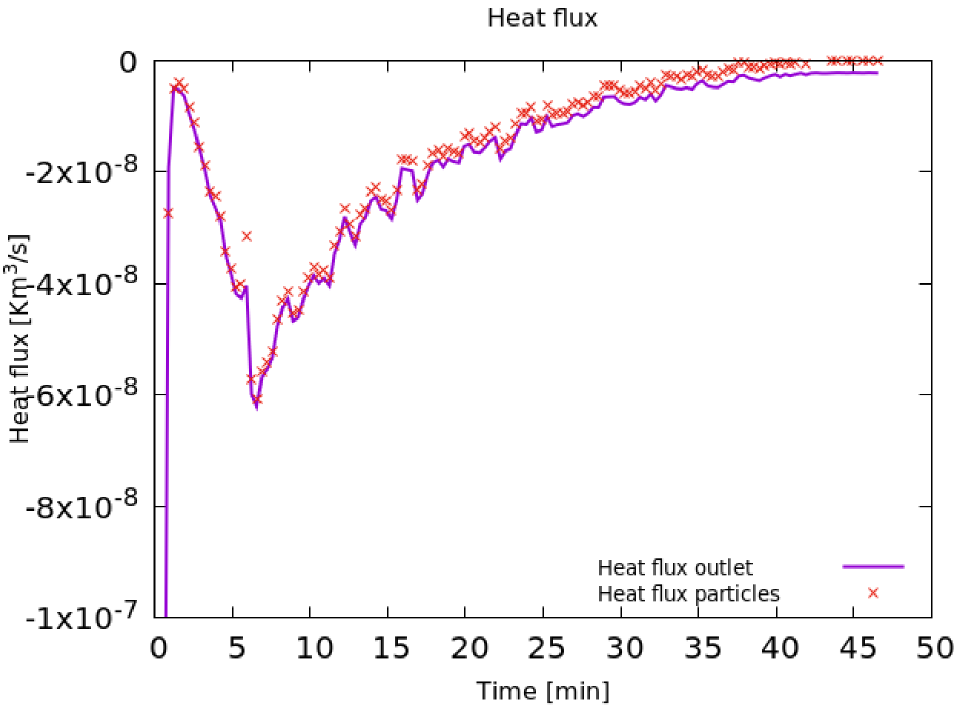

Figure A.9: Heat fluxes through the outlet and the particle surfaces.

Appendix B

Independence studies

B.1 Mesh independence study

Every FEM study requires an evaluation of the spatial convergence. Reducing the cell sizes must not significantly affect the solution. The definition of "significantly" varies per case. Considering the computational cost of the multi-particle hydration model, a 3.5% change between meshes is regarded as acceptable. As test case, an identical setup is used as for the main case of this thesis. Cold, moist air with $T = 299.15$ [K] and $c = 0.603$ [mol/m^3] is flown through the geometry. The solution is found using two separate studies:

1. The first study is to solve the flow field. Cyclic boundary conditions are used on the inlet and outlet, so that a fully developed flow is formed in the REV. On the four sides of the REV, symmetry boundary conditions are applied. No slip boundary conditions are applied at the particle surfaces. The solution of the flow field is exported and used in the second study.
2. In the second study the temperature and concentration fields are solved. The velocity is used in the transport equations, but is not affected by the temperature and concentration, and therefore the model will not solve for velocity (and pressure). A fixed temperature and concentration are prescribed at the inlet. Symmetry boundary conditions are again applied to the sides of the REV. The solid domain is not included in the FEM model, but is simulated through a set of equations that couple it to the flow domain.

Input parameters can be found in table B.2. Output values of interest are:

- The evolution in time of **fractional conversion** α differs per particle. Unfortunately, due to time limitations no completely reacted REV could be simulated. Therefore, one of the particles near the inlet is chosen to monitor as these particles will react first.
- For the **temperature** T, a probe is inserted near the center of the geometry, in the flow domain.
- This probe also logs the **concentration** c.
- The **velocity magnitude** u is measured at the streamwise center of the geometry, although the location should not matter due to the cyclic boundary conditions. The arc over which the velocity is taken starts at the side of the REV and ends at the particle surface.

The monitored locations are shown in figure B.1. To evaluate spatial convergence, four meshes A-D are considered, with mesh A being the coarsest mesh and mesh D being the finest. Two mesh parameters are varied, the overall element size and the face element sizing on the particle surfaces. Using mesh A as the base case, meshes B, C and D are respectively 5%, 10% and 15% refinements, applied to both parameters.

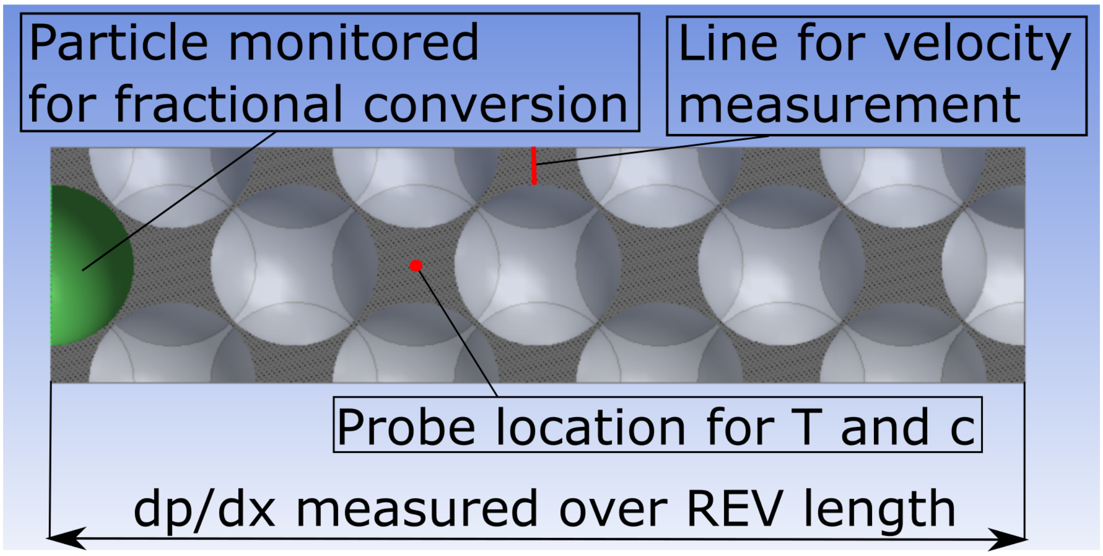

Figure B.1: Locations where the values of interest are monitored.

Table B.1: Mesh parameters used for the spatial convergence study.

Mesh	Overall element size [m]	Face element size [m]	No. elements
A	2.57e-4	5.13e-5	269767
B	2.44e-4	4.87e-5	304035
C	2.31e-4	4.62e-5	353303
D	2.18e-4	4.36e-5	402052

B.1.1 Results

In figure B.2 the fractional conversion of the different meshes are shown. Results are normalized to the values of mesh A. For the simulated time interval, the solutions appear to be converging. The initial difference between meshes A and D is almost 5%, but differences between subsequent meshes (e.g. B-C) are well within the 3.5% limit. Deviations for the temperature (figure B.3) and concentration (figure B.4) are significantly smaller than for α. After approximately 1 hour, the values start to deviate slightly, but then stabilize at around $t \approx 1.8$h. Unfortunately, the velocities show considerable change, especially from mesh A to mesh B. This deviation is particularly strong near the end of the arc, at the particle boundary. This overestimation of the velocity may cause a lower pressure drop over the REV, due to a smaller amount of viscous friction force to be exerted on the fluid.

Table B.2: Constants used in the validation. Several constants are temperature dependent, but are evaluated at the mean temperature of T_i and T_∞.

Symbol	Description	Value
T_i	Initial particle temperature	299.15 [K]
T_∞	Inlet temperature	299.10 [K]
u	Interstitial velocity	0.01 [m/s]
d	Particle diameter	0.97 [mm]
D_m	Diffusion coefficient water vapour in air	3.2e-5 [m^2/s]
ΔH	Enthalpy of reaction	61.54 [kJ/mol]
M_s	Molecular weight K_2CO_3	0.136 [kg/mol]
$c_{p,s}$	Specific heat of particle material	830.8 [J/kgK]
ρ_s	Density of particle material	2255.0 [kg/m^3]
$c_{p,f}$	Specific heat of the fluid (air)	1006.0 [J/kgK]
ρ_f	Density of the fluid (air)	1.18 [kg/m^3K]
k_f	Tthermal conductivity of the fluid (air)	0.026 [W/mK]
μ	Dynamic viscosity	1.876e-5 []kg/ms]

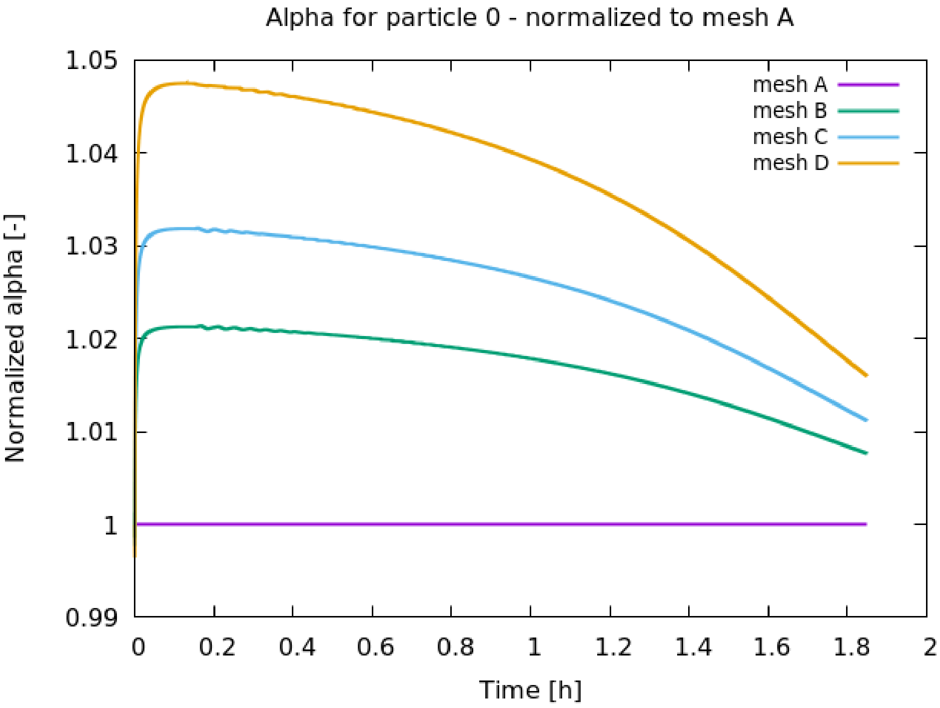

Figure B.2: Fractional conversion α over time. Values are normalized to mesh A.

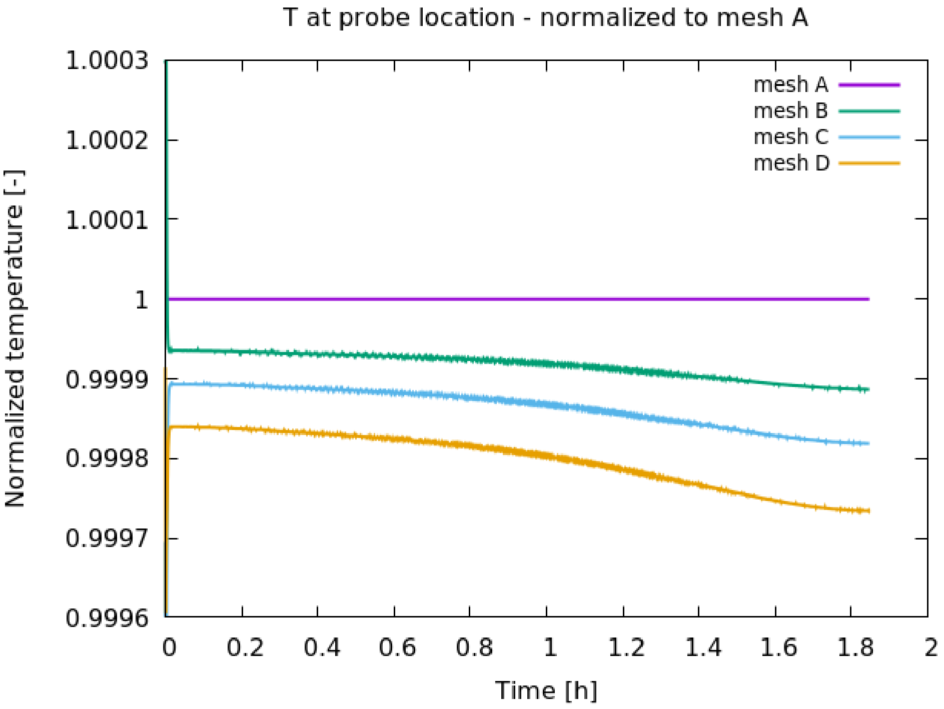

Figure B.3: Temperature at probe location over time. Values are normalized to mesh A.

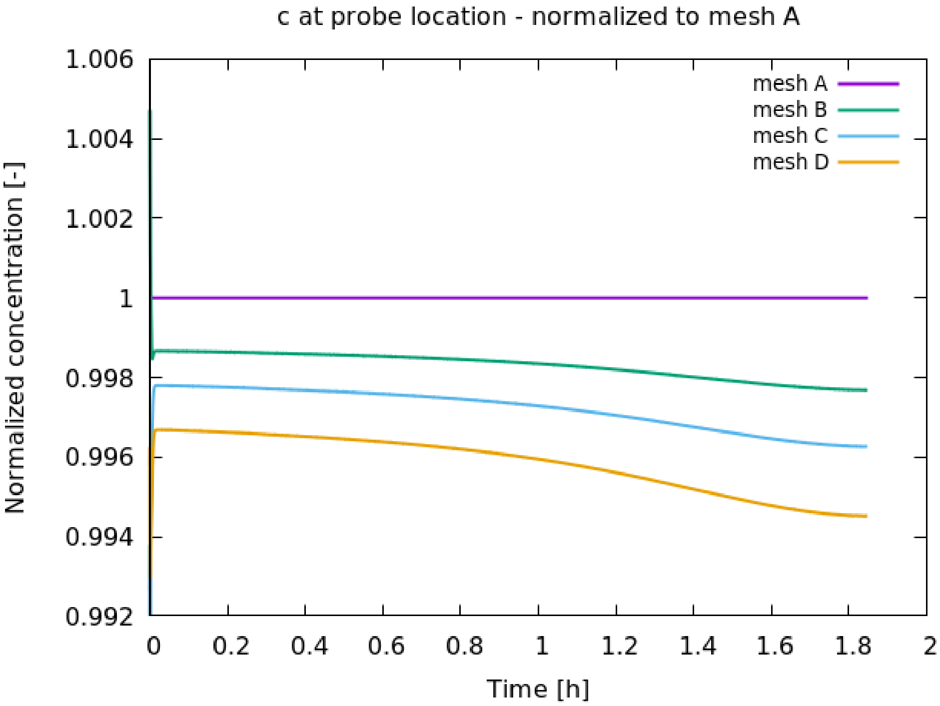

Figure B.4: Concentration at probe location over time. Values are normalized to mesh A.

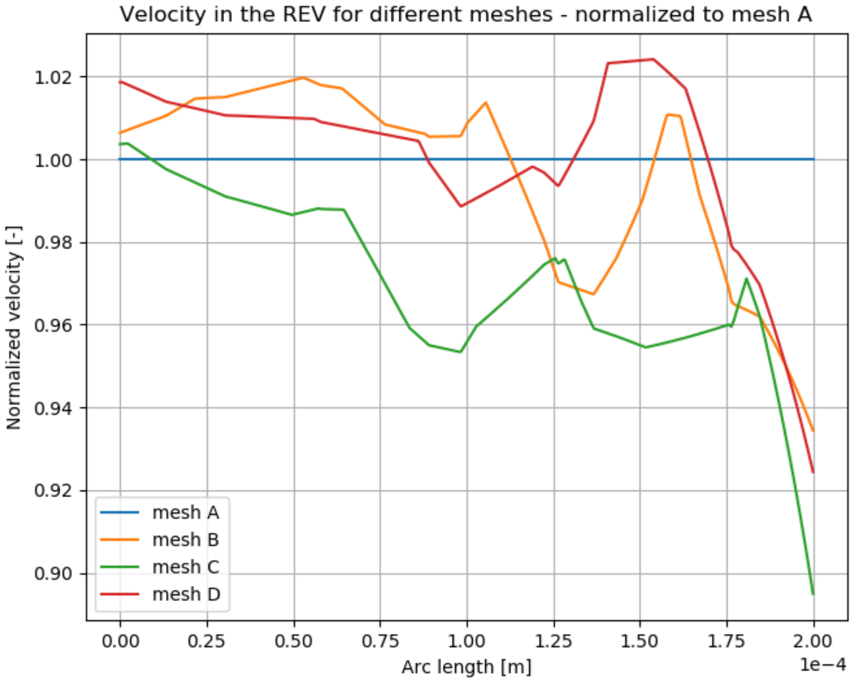

Figure B.5: Velocity plotted over the line shown in figure B.1, normalized to the values of mesh A. A strong deviation between mesh A and mesh B can be seen at the end of the arc, at the particle surface.

B.2 Temporal independence study

Similar to grid independency, the model results must also be independent of the chosen time step. Therefore, three identical studies with different time steps are run, shown in table B.3.

Table B.3: Three cases with different time steps.

Case	Δt [s]
base	0.01
temp1	0.0095
temp2	0.009

B.2.1 Results

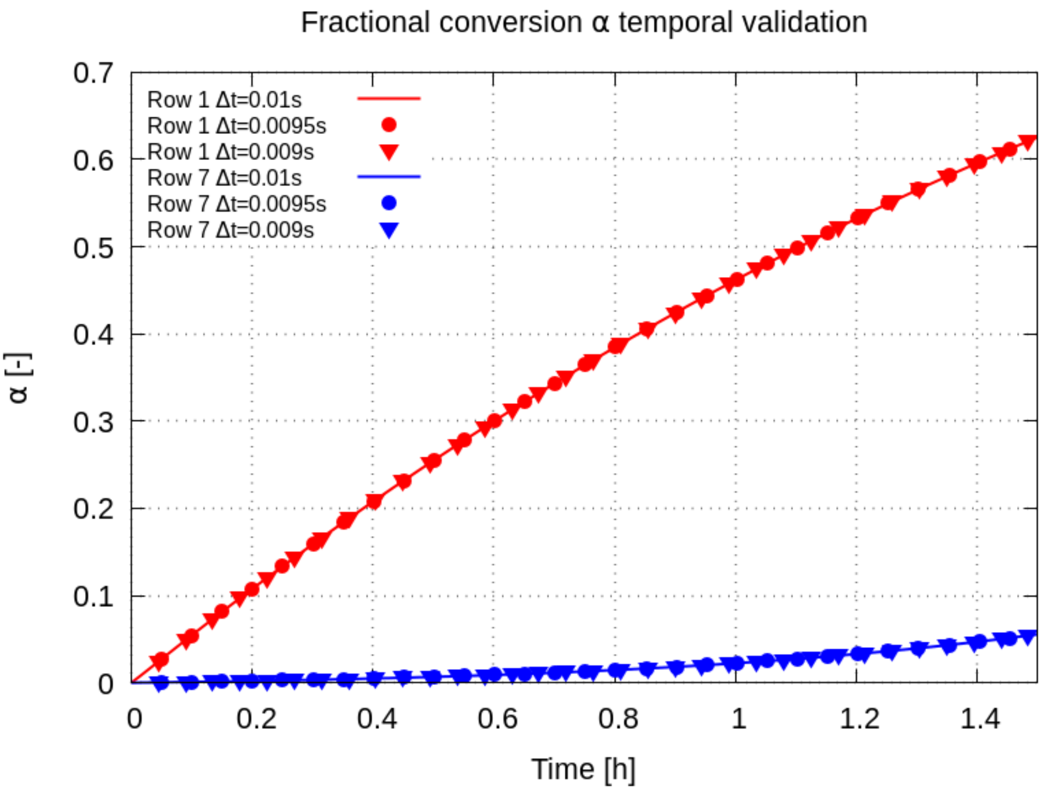

Figure B.6: Fractional conversion over time for different time steps.

In figure B.6 the results are shown. Due to time constraints, only up to 1.5 hours time could be simulated. Row 1 and row 7 are chosen as their conversion progression provides the best contrast.

From the figure, it can be observed that the conversion progression is identical, regardless of the chosen time step. This indicates that the time step of 0.01s used in Chapter 3 is properly chosen.

Appendix C

Verification of the Biot number

A large part of the thermal aspect of the model used in this thesis are based on the assumption that the Biot number is in the order of 0.1, or smaller. With this, the temperature distribution of a solid body can be regarded as constant. The Biot number is defined as

$$Bi = \frac{hL}{k_s}, \tag{C.1}$$

where h [W/m^{2}K] is the convective heat transfer coefficient, L [m] is the characteristic length and k_s [W/mK] is the thermal conductivity of the solid, in this case K_2CO_3. L is generally taken as the particle diameter d_p. In this validation use is made of spheres with radii of 0.485mm. For K_2CO_3, $k_s = 2$ [W/mK] [71]. The definition of h is more complex, as it is a function of the Nusselt number:

$$h = \frac{Nuk_f}{d_p}. \tag{C.2}$$

Substituting equation C.2 in equation C.1, a new rewritten equation for the Biot number is obtained:

$$Bi = \frac{Nuk_f}{k_s}. \tag{C.3}$$

The Nusselt number itself can be determined by using the relation provided by Ranz and Marshall [29]:

$$Nu = 2 + 0.6Re^{1/2}Pr^{1/3} \tag{C.4}$$

This relation was derived from experimental results using a single sphere in a free stream. However, Messai et al. [72] showed that the Nusselt numbers for packed beds (with spherical particles) is comparable to the Ranz and Marshall definition. Therefore this approach is accepted for this verification. The Reynolds number is defined as

$$Re = \frac{u_s d_p}{\nu}, \tag{C.5}$$

and the Prandtl number

$$Pr = \frac{c_{p,f}\mu}{k_f}. \tag{C.6}$$

In the last two equations, μ [Pa·s] is the dynamic viscosity, ν [m^2/s] is the kinematic viscosity equal to the ratio of μ to the density of the fluid ρ_f [kg/m^3], k_f [W/mK] is the thermal conductivity of the fluid, $c_{p,f}$ [J/kgK] is the heat capacity of the fluid. u_s [m/s] in equation C.5 is defined as the product of the interstitial velocity u_i and the packed bed porosity ϵ [-]:

$$u_s = \epsilon u_i \tag{C.7}$$

Table C.1: Parameters used in the Biot number verification. Ambient conditions: 325K, 45% relative humidity.

Symbol	Description	Value
μ	Dynamic viscosity of the fluid (air)	1.93e-5 [m^2/s]
d_p	Particle diameter	0.00097 [m]
ϵ	Packed bed porosity	0.324 [-]
ρ_f	Density of the fluid (air)	1.11 [kg/m^3]
$c_{p,f}$	Specific heat capacity moist air	1006.0 [J/kgK]
ρ_s	Density of K_2CO_3	2255.0 [kg/m^3]
u_i	Interstitial fluid velocity	0.01 [m/s]
k_f	Thermal conductivity of moist air	0.026 [W/mK]
k_s	Thermal conductivity of K_2CO_3	2 [W/mK]

Parameters used in this validation are listed in table C.1. For low Reynolds numbers Nu $\approx$ 2 and Bi $\approx$ 0.026. Because this is significantly lower than 0.1, the temperature distribution in the particles can be regarded constant.

C.1 Results

In Chapter 3, air was flown through a packed bed with an interstitial velocity of 0.01 [m/s], or $Re = 0.56$. In chapter 4, it was shown that for the gap geometry, this resulted in $Nu \approx 0.275$. From equation C.3, $Bi = 0.004$. This shows that, for the conditions used in Chapter 3, the assumption of constant temperature distribution in the particles is valid.

Appendix D

Probe temperatures and concentration & conversion rates

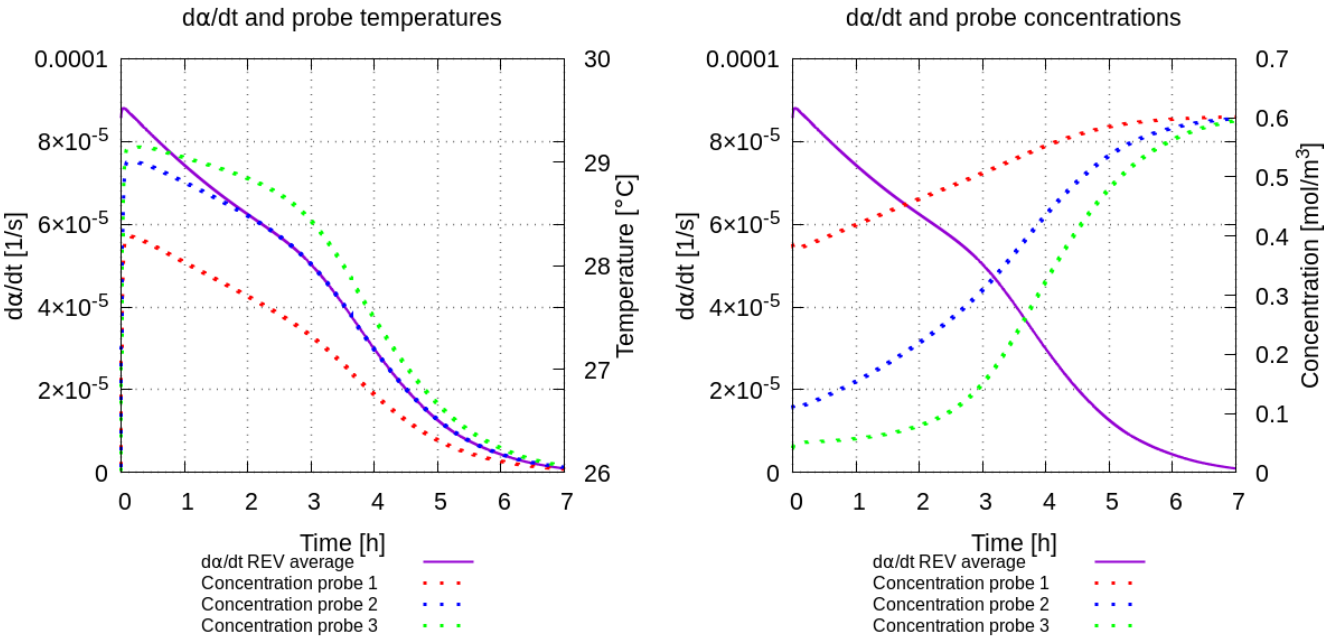

Figure D.1: Fractional conversion rate averaged over the REV and probe temperatures and concentration. The temperatures follow the same trend as the overall conversion rate. Conversely, concentrations start to increase.

TU/e
Technische Universiteit
Eindhoven
University of Technology

Declaration concerning the TU/e Code of Scientific Conduct for the Master's thesis

I have read the TU/e Code of Scientific Conduct[i].

I hereby declare that my Master's thesis has been carried out in accordance with the rules of the TU/e Code of Scientific Conduct

Date

01/11/2019

Name

D'Rose R.D.

ID-number

0930799

Signature

Submit the signed declaration to the student administration of your department.

---

[i] See: http://www.tue.nl/en/university/about-the-university/integrity/scientific-integrity/
The Netherlands Code of Conduct for Academic Practice of the VSNU can be found here also.
More information about scientific integrity is published on the websites of TU/e and VSNU

January 15 2016